Jumps in granular flows down incline

Ségolène Mejean

▶ **To cite this version:**

Ségolène Mejean. Jumps in granular flows down incline. Fluid mechanics [physics.class-ph]. Université Grenoble Alpes; University of Sydney. Nuclear Research Foundation, 2019. English. NNT : 2019GREAI015 . tel-02163536

HAL Id: tel-02163536
https://theses.hal.science/tel-02163536

Submitted on 24 Jun 2019

HAL is a multi-disciplinary open access archive for the deposit and dissemination of scientific research documents, whether they are published or not. The documents may come from teaching and research institutions in France or abroad, or from public or private research centers.

L'archive ouverte pluridisciplinaire **HAL**, est destinée au dépôt et à la diffusion de documents scientifiques de niveau recherche, publiés ou non, émanant des établissements d'enseignement et de recherche français ou étrangers, des laboratoires publics ou privés.

Communauté
UNIVERSITÉ Grenoble Alpes

THE UNIVERSITY OF SYDNEY

THÈSE

Pour obtenir le grade de

DOCTEUR DE LA COMMUNAUTÉ UNIVERSITÉ GRENOBLE ALPES

préparée dans le cadre d'une cotutelle *entre la Communauté Université Grenoble Alpes* et *l'Université de Sydney*

Spécialité : **Mécanique des fluides, procédés, énergétique**

Arrêté ministériel : le 6 janvier 2005 – 25 mai 2016
Présentée par :

Ségolène MEJEAN

Thèse dirigée par **Thierry FAUG** et **Itai EINAV**
préparée au sein des **Laboratoires Irstea Grenoble et the School of Civil Engineering**
dans l' École Doctorale **IMEP2 : Ingénierie – Matériaux, Mécanique, Environnement, Énergétique, Procédés, Production**

Ressauts dans les écoulements granulaires en pente

Jumps in granular flows down inclines

Thèse soutenue publiquement le **11 mars 2019**,
devant le jury composé de :

Monsieur Hamid KELLAY
Professeur, CNRS, Université de Bordeaux, Rapporteur
Monsieur Pierre-Yves LAGREE
Directeur de recherche, CNRS, Université Pierre et Marie Curie, Rapporteur
Monsieur Anthony THORNTON
Professeur associé, University of Twente, the Netherlands, Rapporteur
Monsieur Nicolas RIVIERE
Professeur, INSA, Université de Lyon, Président du jury
Monsieur Thierry FAUG
Chercheur - Ingénieur, Irstea, Université Grenoble-Alpes, Directeur de thèse
Monsieur Itai EINAV
Professeur, University of Sydney, Directeur de thèse

Acknowledgments

This ph.D thesis was a very interesting experience, which involved many people from both sides of the world, that I would like to thank here.

First of all, I would like to thank the people in my jury , the referees Anthony Thornton, Pierre-Yves Lagrée, and Hamid Kellay, and the president of the jury and examiner Nicolas Rivière for reading the manuscript and coming to the ph.D defense. It was a great honor that you came, and I really appreciated your comments on the work.

I would also like to thank my two supervisors who made this work possible. Thierry Faug, I would like to thank you for your enthusiasm about our work, you gave me the will to explore the physics of granular jumps in more details. You were always ready to help me, giving great advices. I could not have imagined a better support. Itai Einav, thank you for welcoming me at the University of Sydney. You made me improve myself and widen the horizons of my thesis. I will never do a bad oral presentation if I follow your great advices.

I would like to thank François Guillard from the University of Sydney for teaching me how to use the X-rays and helping me any time I needed. Thank you also for your advices on the numerical model and other helpful discussions.

I am grateful to the Labex TEC21, which is part of ANR "Inverstissements d'avenir" program for funding, and also to the funds profided for the one-year mobility provided by by both the Idex Graduate School of Univ. Grenoble-Alpes (ANR "Investissements d'avenir" program) and the ExploRa Doc scholarship from the Region Auvergne-Rhone-Alpes, France.

I am very thankful to all my colleagues and friends at Irstea, you make this place such a nice working environment! I would like to address special thanks to the '10am coffee' people, the 'climbing at lunch time' people, the 'Grand Duc' trailers, and my office mates. Thank you Antoine, Hugo, Philomène, Maria Bellen, Rémi, Alexandra, Tijan, Florie, and so many others for your smiles and discussions. I address a special thank to Hervé Bellot for bringing me to the experimental sites at the Col du lac Blanc and the Col du Lautaret, but also teaching me the basics of speleology in your barn. A special thank should also be addressed to Guillaume Piton and Alain Recking for supervising my internship at Irstea. You gave me the (unexpected at that time) desire to do research and continue with a ph.D thesis, and of course to stay at Irstea.

As I had the great opportunity to go to Sydney for one year, and I would like also to thank the people of the University of Sydney, and in particular the people of the School of Civil Engineering. This includes the students of room 101 for discussions, support, and coffee breaks, with a special thank to Hang and Matt, and also the post-doc and researchers from higher floors, that were always ready to help or discuss on a particular point. I cannot think of the support I received in Sydney without mentioning all the very welcoming people from 'SURMC' climbing group of the University of Sydney, that made me discover their beautiful cliffs and mountains, and my friendly housemates from all over the world for the laughs, support, and shared dinners.

I would like to thank all my friends and my family, for all the moments that we shared together, in the mountains or everywhere else, and for your support. Thanks Anna and Pauline for flying for 30 hours to share holidays with me down under.

And finally, thank you Michel for coming to Australia (and further) despite your own thesis, and for all our past and coming adventures.

List of Symbols

$\bar{u}$	Incoming depth-averaged velocity (just before the jump)
$\bar{u}_*$	Depth-averaged velocity just after the jump
β	Boussinesq momentum coefficient before the jump
β_*	Boussinesq momentum coefficient after the jump
$\dot{\gamma}$	Shear rate
$\mathcal{W}$	Lucy function
μ	Interparticle friction between grains
μ_b	Friction between a grain and the bottom or a wall of the channel
μ_e	Effective friction
μ_{cr}	Critical value for the interparticle friction under which the flow regime becomes different
ϕ	Volume fraction of the bulk
ϕ_∞	Maximum packing fraction of the spheres
ρ	Density of the bulk
ρ_p	Density of a grain
ρ_r	Density of the rice
τ_b	Effective frictional stress between the fluid and the base
ζ	Slope of the channel
ζ_0	Limit angle between the free-surface and the horizontal after the jump
A	Bagnold coefficient
d	Diameter of the grains
e	Restitution coefficient between grains
Ec	Conservative energy along the channel
Ec_{conti}	Continuous conservative energy calculated from depth-averaged values
Ee	Elastic potential energy

Eg	Gravitational potential energy
Ek	Kinetic energy
El	Loss of energy by unit length $El = dEc/dx$
f_e	Hydraulic friction coefficient
Fr	Froude number $Fr = \bar{u}/\sqrt{gh\cos\zeta}$
g	Acceleration of gravity
H	Opening height of the reservoir
h	Incoming flow height (just before the jump)
h_*	Flow height just after the jump
H_{cr}	Height of the obstacle for the flow over it to become critical ($Fr = 1$)
h_{cr}	Height of snow at critical state over a dam at height H_{cr}
h_{snow}	Height of the snow cover at the foot of a catching dam against avalanches
I	Inertial number
k	Earth pressure coefficient before the jump
k_*	Earth pressure coefficient after the jump
K_0	Shape factor of the jump
L	Length of the jump
L_r	Larger length of a rice grain
L_r	Length of the roller of the jump
l_r	Smaller length of a rice grain
q	Volumetric discharge
q_c	Critical discharge
q_m	Mass discharge
r	Size of the roughness at the base of the channel
T_p	confinement timescale
T_γ	Typical time of deformation
u^p_{jump}	velocity of the propagation of the jump (0 for a standing jump)
u_0	Velocity of the sliding bottom layer of grains
u_J	Average velocity inside the jump
W	Width of the channel

w	Weight of the jump
x	Distance along the channel
z	Height along the axis perpendicular to the channel
z_0	Height of the sliding bottom layer of grains

Contents

Chapter 1

Introduction

This chapter presents a general introduction to the thesis subject, and provides a review of state of the art advances in the field. Section 1.1 introduces the problem of snow avalanches and avalanche protection dams, Sec. 1.2 reviews the literature on the standing jumps in water, the granular flows and the jumps formed in granular flows. Finally, Sec. 1.3 details the organization of this thesis and explains how to read it most efficiently.

1.1 Context

1.1.1 Snow avalanches

Types of avalanches

A snow avalanche is defined as a mass of snow flowing down a sloping surface. This mass is subjected to gravity and friction. A snow avalanche takes place in three steps, corresponding to three zones. The initiation zone is where the avalanche is triggered through a sudden imbalance between gravity and friction. It can be due to increasing mechanical surcharge (weight of new snow, animals, skiers, etc.), temporal changes of snow properties due to weather events (lack of friction due to heating), or it can be artificially triggered (preventive blasting of avalanches). The phenomenon usually takes place on the top of the mountains, at generally steeper slopes. Then, the avalanche grows up, accelerates, and flows in the propagating zone. Finally, the avalanche will stop either because it meets an obstacle large enough to stop it, or because it reaches milder slopes, after which the mass of the snow decelerates, and eventually comes to a standstill. Depending on the snow conditions, topography, and meteorology, several types of avalanches can be identified:

- Powder snow avalanche (Fig. 1.1a) is a suspension layer made of cold dry snow, dominated by turbulent entrainment, settlement of snow particles and air flow. The density, very low, is on the order of 5 to 10kg/m^3 and the flow depth can range from a few tens of meters to more than 100m. This type of avalanche has a lower impact on structures due to its low pressure, and it does not follow the topography.

- Dense snow avalanche (Fig. 1.1b) represents a flow of snow aggregates with a broad grain-size distribution dominated by friction and collision between grains. The density may vary and typically ranges from 150kg/m^3 up to 400kg/m^3. This type of avalanche tends to follow the topography through the steepest slopes. Even if they are slower than powder avalanches, they can create serious damages on their way because of their much higher bulk density. However, as they follow the topography, they can be stopped, whether it is through lower slopes or an avalanche protection dam. Above a certain amount of liquid water content, the role of water becomes important and brings new processes into play (cohesion, lubrification), and the dry granular model fails.

(a) (b)

Figure 1.1: Powder snow (or mixed) avalanche at Pointe du Dard (France) in 2007 (panel a) and dense snow avalanche with saltation developing at the front at Col du Lautaret (France) in 2011 (panel b). Photos: C. Vion and H. Bellot.

- Mixed avalanche combines the properties of the powder and dense snow avalanches above, and most generally comes with a layer of dense snow under a layer of powder snow.

Avalanche protection dams

The snow avalanches can produce huge damages when they run near villages and other sensitive areas on the mountains. Many constructions are built very close to avalanche paths, and it is a big challenge to protect them. Two types of permanent protections can be installed (See Fig. 1.2):

- "Active" protections are situated on the top of the slopes, in the initiation zones. They try to prevent the avalanche to occur. They can be wood plantations, snow fences (Fig. 1.2b) and snow nets (Fig. 1.2a).

- "Passive" protections are built after the initiation zone. The passive protections do not prevent the avalanche from occurring, but act on pre-existing, propagating avalanches. Their goal is to slow such avalanches down (retarding mounds: Fig. 1.2c), completely deflect the avalanche (deflecting dams, oblique dams, tunnels and snow sheds: Fig. 1.2d), or completely stop the avalanche (catching dams).

This thesis is focused on the dynamic properties of dense snow avalanches and how this information could be used to stop them by appropriately designing avalanche protection dams (through catching dams as a first step).

A handbook edited in 2009 by the European commission [3] summarizes our current knowledge on avalanche protection dams. In particular, the handbook explains that a jump must form for a dam to stop the avalanche, but the current equations are based on an analogy to shallow water shock theory. The aim of this thesis is to improve the equations by considering the jumps formed in flows of dry granular materials.

1.1.2 Avalanche dynamics and design of protection dams

A dense avalanche of dry snow can be characterized by the slope of its path ζ, its thickness perpendicular to the bottom h (or the thickness of its dense part in the case of a mixed

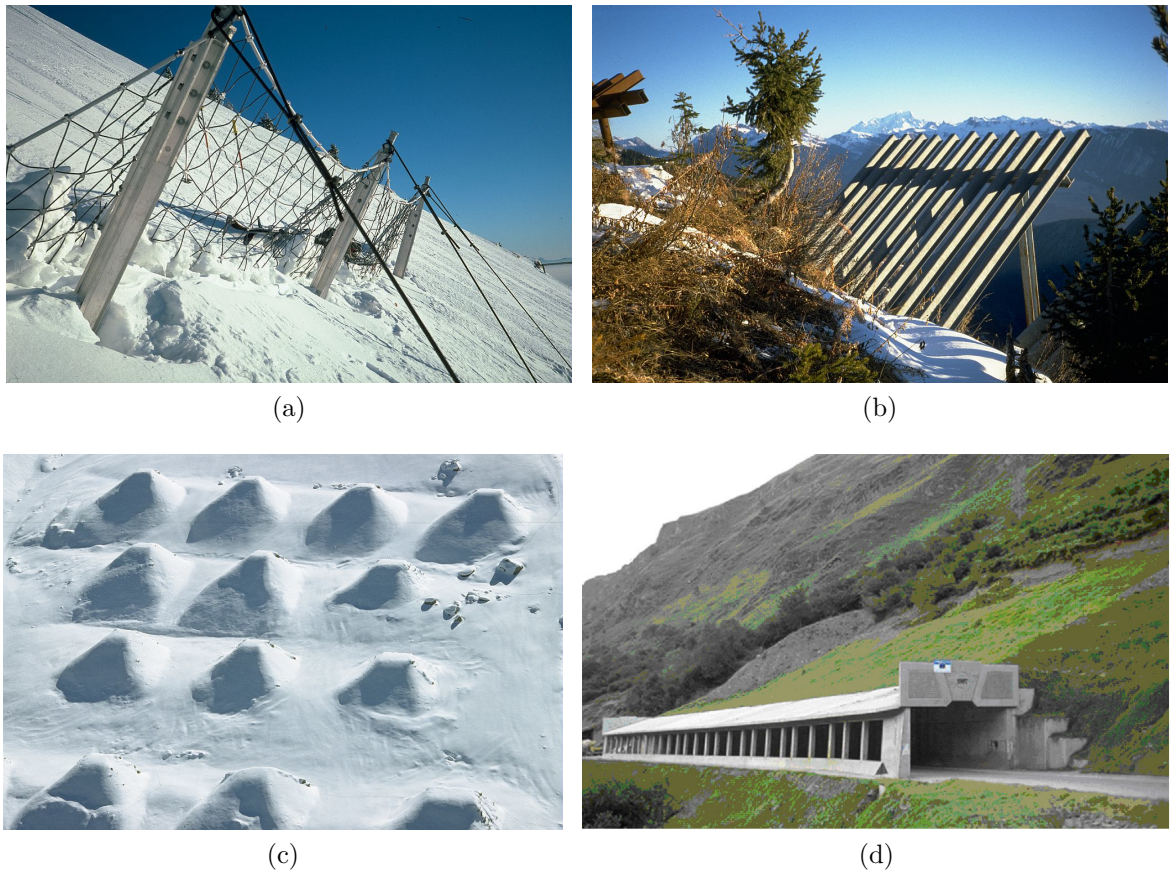

(a) (b)

(c) (d)

Figure 1.2: Examples of “active” (a: snow nets at Chamechaude, France, in 2007, b: snow fences at Le Cellier, France, in 2007) and “passive” (c: retarding mounds at Taconnaz, France, in 2007, d: snow shed at Gourette, France, in 2007) protections against avalanches. Photos from F. Rapin and F. Valla.

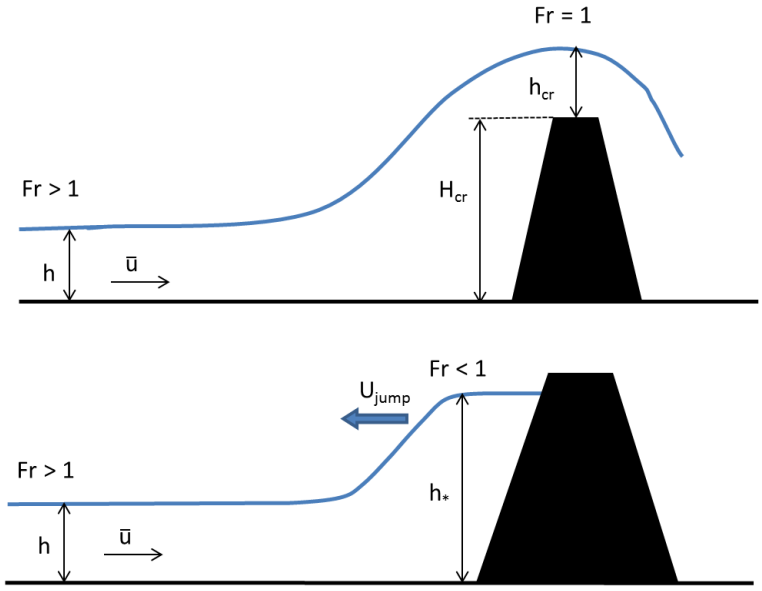

Figure 1.3: Criterion on the height of the dam to stop the avalanche. The dam needs to be higher than $H_{cr} + h_{cr}$ to avoid overflowing ; and higher than h_*, the height of the jump.

avalanche), and its depth-averaged velocity in the direction of the flow $\bar{u} = \frac{1}{h}\int_0^h u(z)dz$. The dynamics of such a shallow free-surface gravity-driven flow is well described by the dimensionless Froude number Fr, which is the ratio of the flow velocity over the maximum speed of free surface gravity waves in the flow:

$$Fr = \frac{\bar{u}}{\sqrt{gh\cos\zeta}} \tag{1.1}$$

with g being the acceleration due to gravity.

When the avalanche starts to flow on high slopes, the flow height is relatively small, the velocity is high, which leads to a supercritical flow, with $Fr > 1$: a disturbance cannot propagates upstream the flow. If the flow remains supercritical when it hits the dam, the avalanche will not stop, but continue to flow over the dam (Fig. 1.3a). In order to prevent this, the dam needs to be high enough to force the flow to become subcritical, with $Fr < 1$, which means that a disturbance can propagate upstream in the incoming flow. This transition from a supercritical to a subcritical flow, where the thickness is sharply increased and the velocity sharply decreased is called a jump.

A jump is created by a disturbance on a supercritical flow, like a dam. When the flow hits the dam, the velocity along the bottom is lowered to zero, and the thickness is increased along the dam until it reaches a thickness h_* (Fig. 1.3.b). Then, as the flow arrives on the dam, it is stopped by the flow at no velocity, and the jump is propagating in the opposite direction of the incoming flow (see Fig. 1.3b).

Then, an avalanche protection dam needs to be designed to be able to create a jump. To this extent, the dam needs to be at least higher than the height after the jump h_*. If the area to protect is very sensitive and no overflow is acceptable, another height should be considered, $H_{cr} + h_{cr}$, which is the maximum height of the dam H_{cr} over which a flow is possible (the overflow is at $Fr = 1$), plus the height of the overflow h_{cr}. Even if a dam height higher is than h_*, which should be sufficient to create a jump, a transition phase may appear for incoming flows with high Froude numbers, with some snow overflowing

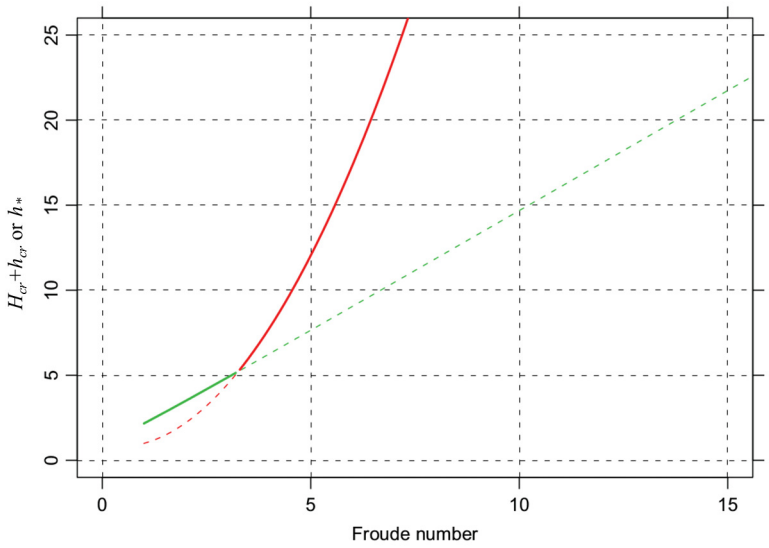

Figure 1.4: Combined criterion to be taken into account according to the Froude number [3]. Red curve corresponds to the critical height to avoid overflow $H_{cr} + h_{cr}$, green curve to the flow height after the jump which forms when the avalanche hits the obstacle h_*.

(see Fig. 1.3). The critical height is derived from a conservation of energy and is expressed as [3, 31]:

$$H_{cr} + h_{cr} = h \left[\frac{1}{k_l} + \frac{1}{2}(k_l Fr \sin\zeta)^2 - \frac{1}{2}(Fr \sin\zeta)^{2/3} \right] \tag{1.2}$$

where k_l is a coefficient for the loss of momentum discussed in [3, 31].

Finally, the thickness of the snow layer that may be already present on the ground h_{snow} has to be accounted for. The height of the avalanche protection dam H_{obst} is then expressed as:

$$H_{obst} \geq h_{snow} + \max(H_{cr} + h_{cr}, h_*). \tag{1.3}$$

As shown in Fig. 1.4 from [3], the thickness of the flow h_* after the jump can be higher or smaller than the critical height $H_{cr} + h_{cr}$ depending on the Froude number. It is then necessary to be able to predict both of them, and in particular the thickness after the jump h_*.

1.2 Standing jumps

This section provides a discussion on the jump phenomenon in order to be able to predict the height after the jump h_*, necessary for the design of avalanche protection dams. In the conditions of an avalanche hitting a protection dam, the jump which will form is not at steady state but propagates upstream. Some equations have been established for the velocity u^p_{jump} of the propagation of the jump [72]. In a reference frame moving along the slope at velocity u^p_{jump}, the jump observed will roughly have the same characteristics of a standing jump. Standing jumps are much simpler to study in the laboratory, or even through numerical simulations, while they can latter be adapted to predict unsteady

conditions through a change in reference frame. This study will only focus on standing jumps.

For a standing jump to happen, the discharge before the jump has to be the same as that after it. Achieving this condition could be easily obtained under experimental or numerical conditions, through the use of servo controller as detailed later in this thesis. Standing jumps have been widely studied in hydraulics because they are quite common in nature and industry and relate to many problems with water flow. Studies of jumps in granular materials remains scarce.

1.2.1 Standing hydraulic jumps

The jumps have been widely studied in hydraulics, because this phenomena can be observed naturally in many situations, and has also been used in structures built to dissipate energy efficiently. The current knowledge on hydraulic jumps has been reviewed in [14].

The hydraulic jumps have been mostly observed and studied in standing conditions on a flat smooth bottom [15, 30]. Under such conditions, mass and momentum conservation equations can be simplified to obtain the famous Bélanger's equation [4]:

$$\frac{h_*}{h} = \frac{1}{2}\left(\sqrt{1+8Fr^2}-1\right) \tag{1.4}$$

The jump height ratio h_*/h is directly controlled by the incoming Froude number Fr. A hydraulic jump is characterized by a sudden rise in the free-surface between a supercritical incoming flow and a subcritical outgoing flow. During the transition, a very turbulent zone with vortices, recirculation, and a high dissipation rate occurs, which is called the roller.

Several types of standing hydraulic jumps on a smooth flat bottom have been identified. Jumps with low incoming Froude numbers, just above 1, will create undular jumps, with a small height ratio, where the free-surface does not reach a constant value but oscillates around an average value. On the other hand, jumps with high incoming Froude numbers will give a big difference between the thickness before and after the jump, with a marked and easily identifiable roller.

The hydraulic jumps have also been studied under other conditions than a flat smooth bottom. In hydraulic works, the jumps are often used in order to dissipate energy. Most of the time, they are created in a sloping channel which suddenly becomes flat. Figure 1.5 shows that depending on the position of the jump compared to the limit between the sloping part and the flat part of the channel, the jump can form on what is called A-jump (foot of the jumps at the limit), B-jump (limit inside the jump), C-jump (end of the jump at the limit, or D-jump (all the jump in the sloping part of the channel). In particular, D-jumps, have been studied in [50, 48, 35]. The slope angle of the channel has a strong influence on the jump height ratio. Bélanger's equation (Eq. 1.4) is not sufficient anymore to obtain the height ratio directly as a function of the incoming Froude number. The height ratio of D-jumps is above the height ratio of a jump on a flat channel for the same Froude number.

Hydraulic jumps have also been studied on rough bases which bring dissipation by friction [13, 34]. As for sloping channels, the Bélanger's equation is not able to predict the jump height ratio. For a same Froude number, it will be lower than the one in Bélanger's equation conditions.

Other types of jumps can also be formed. A circular jump appears when a vertical jet impacts a plane surface, like the water on a sink (see [10]). The symmetry of the jet

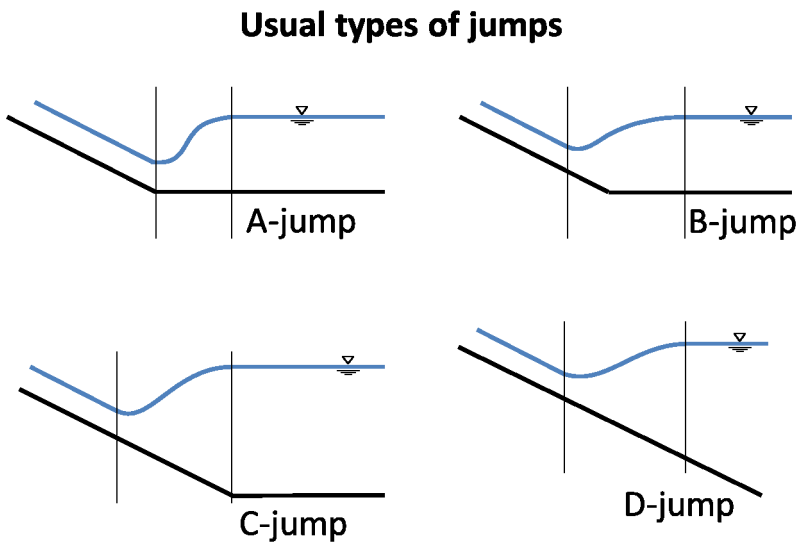

Figure 1.5: Types of hydraulic jumps depending on where they are formed [41, 50].

creates a jump all around the impact point of the jet. Opening a gate under the water between two basins at different water height will create a submerged hydraulic jump [49]. The jump exists, but takes place under the water.

In the design of avalanche protection dams, the equations for hydraulic jumps in a smooth flat base are still used, including in the 2009 handbook by the European commission [3], in order to obtain the height ratio h_*/h. However, the behaviour of the snow inside a dense avalanche is much more similar to the one of a dry granular material: it occurs only on slopes, it is compressible, and frictional-collisional processes come into play. Because of some similarities with the granular jumps, hydraulic jumps in a sloping channel (D-jumps) or on a rough base (which brings friction to the water, comparable to the friction between grains) will be studied in more details in Part I. In order to take into account the slope angle, or some frictional processes, the jump cannot be considered as a shock with no length. It is necessary to take into account the finite length, finite volume, and finite weight of the jump.

1.2.2 Granular flows and standing granular jumps

From snow to grains

The properties of the snow inside an avalanche can be studied in the run-out zone, which is easily accessible and which shows the material after any transformation in the avalanche. Figure 1.6 shows several deposits of dense-snow avalanches, which are composed of snow aggregates. Every snow aggregate is composed of many snow grains. In the initiation zone, the unstable snow fractures and begins to slide. Then, while flowing in the propagating zone, the snow will separate into pieces which will be rounded by several processes inside the flow, many of them dependent on the liquid water content: friction, collisions, segregation, mixing, crushing, aggregations etc. Figure 1.6a shows quasi-spheric snow aggregates: this is explained by the very long avalanche path (7 km, deposit in Taconnaz, France) which let the time for all the processes to occur. On the opposite, the angular snow aggregates of Fig. 1.6c suggest a much shorter flowing zone, whereas Fig. 1.6b has an intermediate length of its flowing zone. The liquid water content also influences the

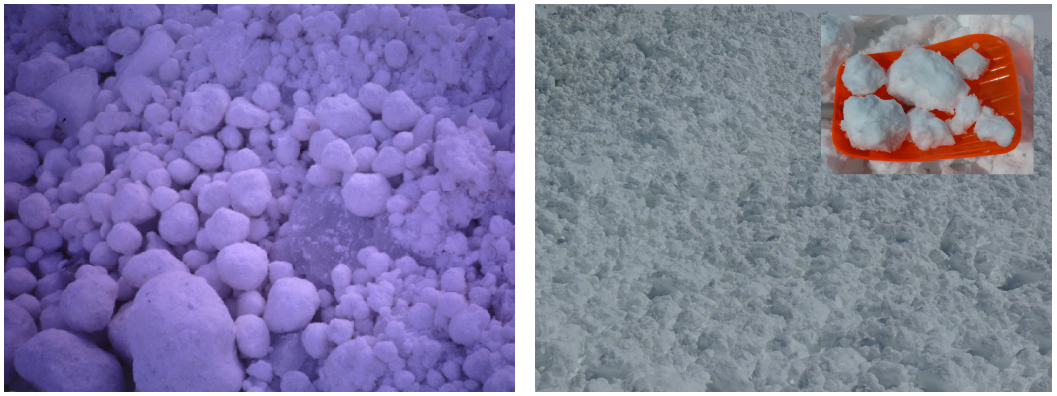

(a) (b)

(c) (d)

Figure 1.6: Snow aggregates in some avalanche deposits. (a) Rounded snow aggregates. (b) Relatively rounded snow aggregates (inset: zoom on some aggregates in a shovel of about 25cm long). (c) Angular snow aggregates. (d) Snow aggregates in a matrix.

aspect of the avalanche deposit, allowing for example snow aggregates in a matrix made of individual snow grains (Fig. 1.6d). For a certain range of liquid water content in the snow, and length of the avalanche path, we obtain rounded aggregates of snow that will behave in a similar way as a flowing granular material, which stops its motion in the deposition zone, when the slope in not high enough for the aggregates to flow or because of an obstacle. Some studies [52, 57] validated the similarities between snow avalanches and laboratory experiments with glass beads, comparing the angles where no flow can occur and the angles where no deposit remains.

Like many studies on snow avalanches, the present thesis will focus on the use of stiff spherical grains as a simplified material to represent the snow.

Granular flows

A granular material is a complex material where several regimes have been identified depending on the boundary conditions (see [36, 20]).

1. In the solid regime [58, 53], the grains do not move or move only very slowly relative to each other. There is persistent frictional contact between grains, and force chains can easily develop. It is mostly studied in soil mechanics.

2. In the liquid regime [40, 51], the grains are flowing, but the media remains dense. It is characterized by enduring contacts between grains, the particles interact with

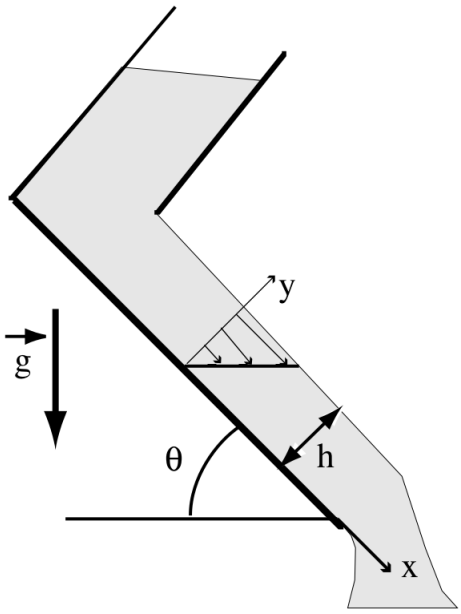

Figure 1.7: Granular flow down a slope in GDR MiDi [21]

both friction and collision. This regime has many practical applications and is generally difficult to predict.

3. In the gaseous regime [37, 24], the grains go in all directions, creating a dilute chaotic medium. The particles are mainly interacting by binary collisions. The kinetic theory applied to granular materials is relevant for this gaseous regime.

Dense granular flows have been studied for many industrial applications, or in geophysics to study natural hazards including snow avalanches. The wide range of applications implies a wide range of different physical models to study this material in the dense flowing regime. GDR MiDi thoroughly reviewed many different studies together in 2004 [21]. Six configurations have been selected, including three free-surface flows and three confined flows. One of the free-surface configurations corresponds to a dense granular free-surface flow of spherical particles down a slope, which is comparable to a snow avalanche (see Fig. 1.7).

In this configuration, two slope angles of the incline, which depend on the thickness of the flow and on the roughness of the bottom, can be identified, defining three zones. Below ζ_{stop}, no flow can occur ; above ζ_{start}, the grains can only flow ; and between ζ_{stop} and ζ_{start}, the material can flow or not depending on the previous state.

Far enough from ζ_{start} in the flowing regime, the velocity profiles obey a Bagnold-like profile. If the bottom of the chute is smooth, the first layer of grains is sliding on the bottom, and the velocity profile follows a Bagnold profile over a sliding velocity [19, 9]:

$$u(z) = \bar{u_0} + A(\zeta)\sqrt{gd}\left[\left(\frac{h-z_0}{d}\right)^{3/2} - \left(\frac{h-z_0}{d} - \frac{z-z_0}{d}\right)^{3/2}\right]. \tag{1.5}$$

The sliding velocity is noted u_0 and the limit between the sliding layer of grains and the grains following Bagnold profile is noted z_0. This thickness z_0 is often taken equal to $1.5d$ [19, 9]. The coefficient A is called Bagnold coefficient and depends on the slope angle.

The volume fraction appears to be almost constant along the flow thickness, but the value of this constant decreases if the slope angle of the incline decreases.

Several dimensionless numbers could be identified that characterize this kind of granular flows. Even if originally comes from hydraulic studies, the Froude number Fr (Eq. (1.1)) is relevant to free-surface flows of dense granular media. The Froude number is relatively close to the inertial number I, widely used in dense granular media. The inertial number shows the competitive effects on the granular media, associated with the shear rate $\dot{\gamma}$ and the confinement pressure P. This gives two characteristic times: $T_\gamma = \frac{1}{\dot{\gamma}}$ as the typical time of deformation, and $T_P = d\sqrt{\frac{\rho_p}{P}}$ the confinement timescale. The ratio gives the inertial number I:

$$I = \frac{T_p}{T_\gamma} = \frac{\dot{\gamma} d}{\sqrt{P/\rho_p}} \tag{1.6}$$

For free-surface flows down inclines, the velocity profile follows a Bagnold-like profile (Eq. (1.5)). GDR MiDi [21] shows that by integrating this velocity profile, it is possible to also express the depth-averaged inertial number $\bar{I}$ as a function of the depth-averaged velocity $\bar{u}$ and the thickness of the flow. Faug et al. [19] expressed it for the case of a smooth bottom and a sliding velocity as:

$$\bar{I} = \frac{5}{2}\frac{d}{h - z_0}\frac{(\bar{u} - \bar{u_b})}{\sqrt{\phi g (h - z_0)\cos\zeta}}. \tag{1.7}$$

Another interesting dimensionless number is the effective friction coefficient μ_e. Many studies have tried to link it to the inertial number [40]. This is called the $\mu(I)$-rheology. In the case of a free-surface flow down an inclined chute, it is simply equal to the tangent of the slope $\mu_e = \tan\zeta$.

Unlike hydraulic flows, an experimental configuration of a free-surface flow down an incline chute alimented by a reservoir full of grains (the configuration of Fig. 1.7 from GDR MiDi) allows to ensure a constant discharge of grains inside the chute. This has been studied first by Beverloo [6], who found a law for the discharge flux as a function of the height of the opening at the end of the reservoir H.

$$q_m = \alpha \phi_\infty \rho_p \sqrt{gH \sin\zeta} HW \tag{1.8}$$

with α a coefficient which depends on the channel characteristics, ϕ_∞ the maximum close packing of the grains (which depends on the grain size distribution), and W is the width of the channel.

Savage and Hutter [60] applied shallow-water equations to flows of granular media. Later studies have tried to improve the application of the depth-averaged framework by adapting it to the granular media [51].

Standing granular jumps

Granular jumps are formed in an analogous way as hydraulic jumps. This is also the transition between a thin fast (supercritical) flow with a Froude number larger than 1, and a thick slow (subcritical) flow with a Froude number lower than 1. Unlike hydraulic flows, granular media necessarily need a slope to flow, and then, the jumps can only occur on slopes. Other fundamental differences exist between hydraulic and granular jumps. Granular jumps are compressible, and frictional and collisional processes come into play.

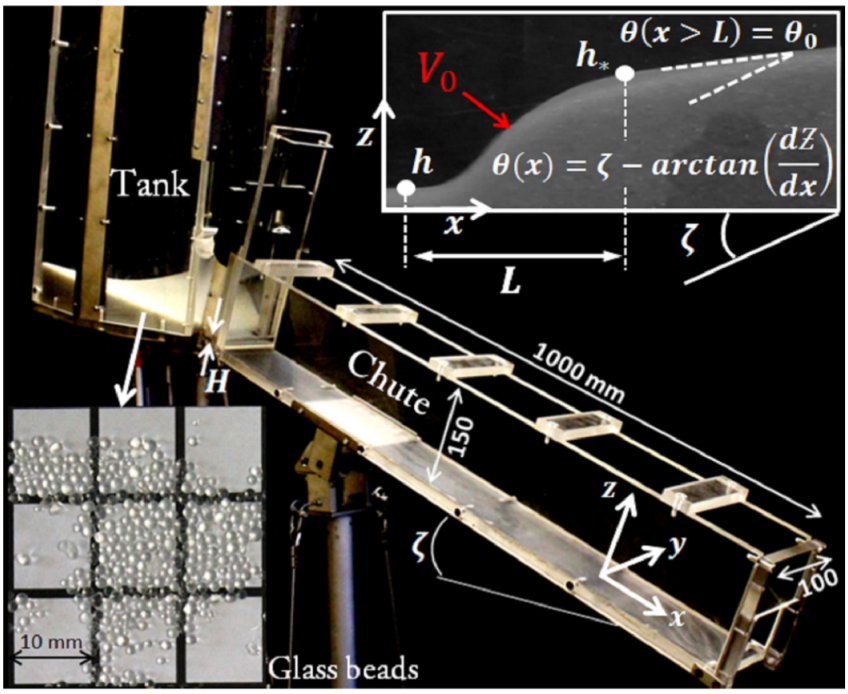

Figure 1.8: Faug et al. [19] laboratory experiment to produce granular jumps in the school of Civil Engineering of Sydney.

Even if they are less common than hydraulic jumps, previous studies have studied the jumps on a flow of granular material [61, 8, 7, 69, 38].

Many conditions can be considered for granular jumps down inclines. The granular material can be made of spheres or have other shapes, the ambient fluid (which can be air or another fluid) can be negligible or not, the inclined plane can be a rectangular channel, a plane without limits, or can have any other shape, the bottom of the inclined plane may be smooth or rough. The obstacle that creates the jump can vary as well, being a straight dam, an oblique dam, an adjustable gate, a contraction, etc.

Most studies consider the jump as a shock, focusing on the jump height ratio h_*/h without paying attention to its shape and length. This means that they consider a jump as a discontinuity in the free-surface, with no length, and thus no volume, weight or shape.

Faug et al. [19] conducted a series of laboratory experiments of granular jumps made of glass beads (Fig. 1.8). They considered their jumps as a full volume and studied extensively their shape over a wide range of slope angles and mass discharges. Their study concluded that the traditional Bélanger's equation, strictly valid for incompressible frictionless flows on a flat bottom, is suitable for predicting the relative height of the jump h_*/h on a first approximation, but it is less accurate for some slow and thick flows, or very thin or very dilute flows. They suggested that further work could focus on the jumps, and particularly on their geometry (K_0, L), friction (μ_e) and density variation (ρ_*/ρ).

The present thesis directly continues the work of Faug et al. [19]. The goal is to investigate in more detail the properties of the jumps, using as many tools as possible, including the theoretical approach, the development of numerical models and advancement of previous measurement techniques in laboratory experiments. The present study may have some implications to the design of avalanche protection dams, as the classical equations used in [3] are not always accurate enough and may underestimate or overestimate the dam height in some cases.

1.3 Reading guide

This thesis is mostly based on papers, either published or under preparation. Following the first chapter, the rest of the thesis could be seen to be structured by three main parts.

Each part presents one aspect of the work: theoretical, numerical, or experimental, and is quite independent from the others, although it should be better to read the thesis linearly. Each part corresponds roughly to a single year of work. The parts are divided into chapters. The chapters can be a journal article (published, under review, or in preparation), a discussion about the article (after its publication), or a part of the thesis work which did not end up as an article.

At the beginning of each chapter, a chapeau explains how the chapter fits the scope of the whole thesis to help the reading.

- **Part I: Theoretical relations for jumps in both hydraulic and dry granular flows.**
  - ***Chap. 2: A general relation for standing normal jumps in both hydraulic and dry granular flows.*** This chapter is an article published in *Journal of Fluid Mechanics* in 2017 [44], that summarizes a large part of the work done on the theoretical part of the thesis. It describes a new relation for the height of jumps in both water and dry granular flows, which accounts for the finite size of the jump and its compressibility, based on depth-averaged mass and momentum conservation equations.
  - ***Chap. 3: Discussion on resistive forces across water jumps.*** This chapter provides a discussion on a specific point of the previous chapter published in the *Journal of Fluid Mechanics*. The expression of the resistive force across the water jumps is further analysed. We show that a classical form of dissipation for water jumps is not able to explain the effects observed with previous laboratory experiments, and a discussion follows on the form that could take this resistive force to fit the experimental data.
- **Part II : Two Dimensional numerical simulations.**
  - ***Chap. 4: Discrete Element Method simulations of standing jumps in granular flows down inclines.*** This chapter is a conference article published in *EPJ Web of Conferences* in 2017 (Powder and Grains Conference) [46] that presents some preliminary results of the numerical work. Its interest is to present the numerical software used, YADE, based on the Discrete Element Method (DEM) and the 2D set-up designed to produce standing granular jumps.
  - ***Chap. 5: Length of standing jumps along granular flows down inclines.*** This chapter is the main chapter of Part II, presenting most of the work done on the numerical part of the thesis. It corresponds to an article submitted to *Physical Review Fluids*. It is presenting how varying macro (slope, discharge) and micro (interparticle friction coefficient, grain diameter) parameters affects the jumps patterns. A phase diagram diagram varying the macro parameters allows to differentiate the jumps as a function of their steepness and compressibility and confirms previous studies. Looking inside the jumps thanks the the micro parameters accessible by the numerical model allows to classify the jumps into three main types : laminar granular jumps, steep

colliding granular jumps, and hydraulic-like granular jumps with an internal roller.

  - ***Chap. 6: Energy dissipation in numerical granular jumps.*** This chapter relies on the numerical work to address energy balance before, during, and after the jumps. It shows how the energy dissipates before, during, and after the jumps as a function of the same macro and micro parameters as in the last chapter. It also includes a discussion on two different methods to obtain the energy: a coarse-grained method at the local scale, and an hydrodynamic method in a hydrodynamic point of view using depth-averaged values. It shows that the assumptions in the hydrodynamic model are good in the first order, but seem to miss a part of the information at the micro scale.

- **Part III: Experimental study**.

  - ***Chap. 7: X-ray radiography of standing jumps down inclines.*** This chapter summarizes all the experimental work done using a granular chute facility at the University of Sydney. Experiments have been made by varying the slope angle of the channel and the mass discharge of the incoming flow, using an innovative measurement technique based on dynamic X-ray radiography. Most of the work was done with spherical grains (glass beads). The last part is showing preliminary results with elongated grains that are able to get oriented, evidencing a totally different type of jump thanks to the change in the grains. This will become an article, currently in preparation.

Finally the main results of the whole thesis work, and some perspectives for future work are discussed in the last chapter, ***Chap. 8: Conclusions and perspectives***.

Part I

Theoretical relations for jumps in both hydraulic and dry granular flows

Chapter 2

A general relation for standing normal jumps in both hydraulic and dry granular flows

Ségolène MEJEAN, Thierry FAUG, Itai EINAV
Published in Journal of Fluid Mechanics, 816, 331-351 (2007)

This chapter summarizes the theoretical work of this thesis. The introduction (Sec. 2.1) as part of this paper may be skipped in the context of the thesis as its content is actually provided in the more general introduction to this thesis (Chap. 1). This chapter is based on mass and momentum equations in order to obtain a general relation that would work for any fluid (here: water or glass beads). Section 2.2 shows how the relation is obtained for both water and glass beads; Sec. 2.3 compares the parameters that appear in the general equation under different boundary conditions, for water and dry grains; and Sec. 2.4 applies the general equation on the jumps formed in laboratory found in the literature. Finally, Sec. 2.5 concludes on this general equation and discusses on perspectives.

Abstract: Steady free-surface flows can produce sudden changes in height and velocity, namely standing jumps, which demarcate supercritical from subcritical flows. Standing jumps were traditionally observed and studied experimentally with water in order to mimic various hydraulic configurations, for instance in the vicinity of energy dissipators. More recently, some studies have emerged to investigate standing jumps formed in flows of dry granular materials, which are relevant to the design of protection dams against avalanches. In the present paper, we present a new explicit relation for the prediction of the height of standing jumps. We demonstrate the robustness of the new relation proposed by revisiting and cross-comparing a great number of data sets on standing jumps formed in water flows on horizontal and inclined smooth beds, in water flows on horizontal rough beds, and in flows of dry granular materials down smooth inclines. Our study reveals the limits of the traditional one-to-one relation between the sequent depth ratio of the jump and the Froude number of the incoming supercritical flow, namely the Bélanger equation. The latter is a Rankine-Hugoniot relation which does not take into account the gravitational and frictional forces acting within the jump volume—over the jump length, as well as the possible density change across the jump when the incoming fluid is compressible. The newly proposed relation, which is exact for grains and a reasonable approximation for water, can solve all those issues. However, this relation can predict the height of the standing jump only if another length scale, which is the length of the jump, is known. We conclude our study by discussing empirical but simple closure relations to get a reasonable estimate of the jump length for water flows and dry granular flows. These closure relations can be used to feed the general jump relation and then predict with accuracy the height of the jumps in a number of situations, provided that well calibrated friction laws—described in the present study—are considered.

2.1 Introduction

Supercritical free-surface flows can experience a sudden change in flow conditions caused for instance by the presence of an obstruction, which produces a thicker and much slower flow, subcritical and able to propagate in the direction opposite to the incoming stream. The discontinuity in height and velocity, namely the normal jump, demarcates the transition between the incoming supercritical flow and the outgoing subcritical flow. Under certain conditions, an equilibrium is met and standing jumps can be produced. Standing jumps were observed in various experiments for a wide range of free-surface flows involving different fluids. There exist a great number of experiments with water flows in air, as reviewed by [14]. The standing jumps were also observed in other fluids, such as flows of oil—or oil mixture—in water ([73]), and flows of granular materials in air, as reported in the recent experimental study by [19] and a number of valuable references therein.

Standing jumps in free-surface flows are ubiquitous in many real-world engineering applications. For instance, the design of dissipative structures in interaction with large-scale flows, such as energy dissipators used in hydraulics [29] or protection dams against avalanches [3], needs a robust prediction of the jump heights in a broad range of flow conditions. Those practical applications motivated several theoretical, experimental and numerical studies. However, predicting the height of normal standing jumps for any kind of fluid, including water, and under different flow boundary conditions, is still a challenging question in fluid mechanics.

The following equation, known as the Bélanger equation (see [15]), and derived from mass and momentum balances across the jump discontinuity:

$$\frac{h_*}{h} = \frac{1}{2}\left(\sqrt{1+8Fr_0^2}-1\right), \tag{2.1}$$

was initially developed for horizontal water flows to predict the height h_* of the standing jump relative to the height h of the supercritical incoming flow. It predicts a one-to-one relation between the sequent depth ratio h_*/h and the Froude number defined by $Fr_0 = \bar{u}/\sqrt{gh}$ ((2.1) is only valid for supercritical incoming flows, meaning $Fr_0 > 1$). The Froude number is the ratio of the depth-averaged velocity $\bar{u}$ to the speed of gravity waves $\sqrt{gh}$. The Bélanger's equation is a Rankine-Hugoniot relation in the sense that it considers the jump as a mathematical discontinuity, thus ignoring—or neglecting—the finite length of the jump itself. In other words, the Bélanger's equation states that the jump height would only depend on the velocity and the height of the incoming flow. However it is most likely that under certain conditions volume forces, namely the component of the jump weight along the slope (for flows down an incline) and/or the resistive friction force, can come into play. Furthermore, the Bélanger equation does not consider any change in density across the jump which may occur when the incoming flow is compressible. The traditional Bélanger equation is therefore valid for jumps formed in incompressible and frictionless fluids on a horizontal and smooth bottom.

The present paper revisits a number of experimental data showing that the Bélanger equation fails in predicting the jump height because at least one assumption made to establish Bélanger's equation is violated by the experimental conditions and/or the fluid rheology at stake. The overarching aim of the paper is to overcome the gap between the prediction from Bélanger's equation and the existing experiments, using a universal relation for the height of standing jumps. A general solution, which takes into account the forces acting over the finite length of the jump, as well as the density change across the jump, is derived. It is then validated on a number of laboratory data sets available

in literature, provided minimal assumptions are made for the closure relations associated with the resistive friction force within the jump volume.

We apply mass and momentum conservation equations over the finite length of the jump. This allows us to establish a cubic equation that can be solved by Cardano's method ([12]). We revisit and cross-compare relevant experimental data on jumps involving water flows on horizontal and inclined planes, over smooth or rough beds, as well as dense and dilute flows of granular materials down an inclined plane (§2.3). Each term contributing to the general relation can be analysed and carefully checked against the various existing experiments, which allows us to highlight the robustness of this general relation in all situations. The relation is used to calibrate relevant friction closure laws for both water and granular jumps (§2.4). However the general relation can predict the height of the jump only if another length scale, which is the length of the jump, is known. As this crucial question is not yet resolved, we end §2.4 by proposing empirical but simple closure relations for the jump length. §2.5 summarizes the main outcomes of our study and concludes on the need of new developments regarding the length of the standing normal jumps.

2.2 General relation for standing jumps

We consider a free-surface flow—of either water or dry grains—down an incline, as shown in figure 2.1. Figure 2.1c (bottom panel) displays two pictures of granular jumps observed in laboratory tests by [19]: a diffuse jump at low slope angle and a steep jump, with the presence of recirculation, at high slope angle. The slope of the incline is called ζ. The depth-averaged velocity, the density, and the height (perpendicular to the bottom) of the flow are respectively $\bar{u}$, ρ and h before the jump, and $\bar{u}_*$, ρ_* and h_* after the jump. The jump length L is taken parallel to the bottom (see its exact definition in §2.3.1). When the bottom is rough, we introduce the parameter r which is the mean height of the roughness (see figure 2.1a).

The jump is defined as the part of the flow between the upstream supercritical flow and the downstream subcritical flow, both at equilibrium. In this definition, the jump cannot be considered as a shock, as done for instance in [32], [27], or [69]. In contrast to a shock, the jump has a finite length L and then a volume on which forces come into play. We apply mass and momentum conservation equations in their depth-averaged forms under steady state conditions to this jump volume, in a similar fashion as initially proposed by [61] for granular flows, and earlier by [16] for water flows. In addition, we take into account the density change across the jump, as recently considered by [19]. The forces that apply on the jump volume are the weight of the jump w (see its expression in §2.2.1), the effective frictional force acting over the jump length τ_b (see its expressions in §2.2.1 and §2.2.2 for dry grains and water, respectively), and the pressure forces acting on each side of the jump, which are assumed to be hydrostatic. The depth-averaged equations of mass and momentum conservation projected on the $x-$axis (along the slope of the incline) read as follows:

$$\rho \bar{u} h = \rho_* \bar{u}_* h_*, \tag{2.2}$$

$$\beta_* \rho_* \bar{u}_*^2 h_* - \beta \rho \bar{u}^2 h = \frac{1}{2} k \rho g h^2 \cos\zeta - \frac{1}{2} k_* \rho_* g {h_*}^2 \cos\zeta + w \sin\zeta - \tau_b L, \tag{2.3}$$

where k (respectively k_*) and β (respectively β_*) hold for the earth pressure and Boussinesq momentum coefficients before (respectively after) the jump, as will be discussed in more detail in §2.3.6.

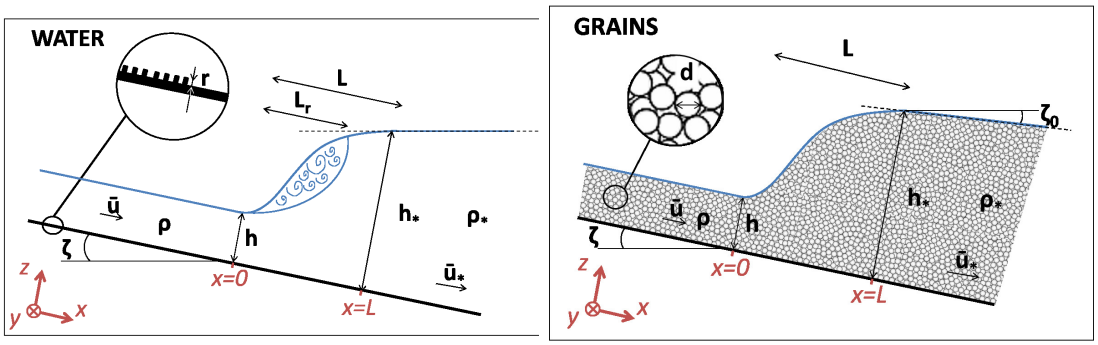

(a) (b)

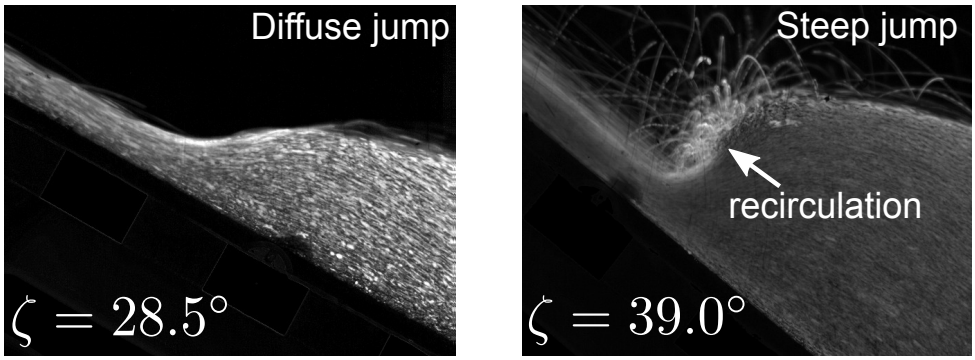

(c)

Figure 2.1: Sketch of a stationary jump made of water (a) and dry grains (b), with $\bar{u}$, ρ and h the incoming depth-averaged velocity, density and height. The star $*$ in subscript refers to the values of velocity, density and height after the jump. ζ is the slope of the channel, L the length of the jump, and r represents the mean size of the roughness. In the case of water, some authors (see [13] for instance) did not measure the jump length but the length of the roller, L_r, which is a bit smaller than the jump length, as shown in (a). In the case of a granular flow, the outgoing flow is not horizontal but inclined at a constant angle with horizontal, which corresponds to the limit angle below which no jump can form (see more details in [19]). The two pictures (c) show two granular jumps observed by [19], a diffuse jump for a low slope angle and a low Froude number, and a steep jump with recirculation for a large slope angle and a large Froude number.

2.2.1 Standing granular jumps

For flows of dry granular materials down an incline, the effective frictional stress acting over the jump length can be expressed as a Coulomb-like stress:

$$\tau_b = \mu_e \frac{w}{L} \cos\zeta, \tag{2.4}$$

where μ_e holds for the effective coefficient of friction, which includes all the sources of friction over the jump length. A depth-averaged friction law for μ_e estimated over the entire length of the jump will be proposed in §2.3.5. Combining (2.4) with the continuity equations 2.2 and 2.3 yields the following relation for a granular fluid down an incline:

$$Fr^2 \left(\beta - \frac{\beta_*}{\frac{\rho_*}{\rho}\frac{h_*}{h}} \right) = \frac{1}{2} \left[k_* \frac{\rho_*}{\rho} \left(\frac{h_*}{h} \right)^2 - k - K_0 \frac{L}{h} \left(1 + \frac{\rho_*}{\rho}\frac{h_*}{h} \right) (\tan\zeta - \mu_e) \right]. \tag{2.5}$$

The Froude number Fr takes into account the slope: $Fr = \bar{u}/\sqrt{gh\cos\zeta}$. We define the shape factor K_0 so that the weight per unit width of the jump can be written $w = \frac{1}{2} K_0 g L(\rho h + \rho_* h_*)$, as initially introduced by [61]. In other words, we have:

$$K_0 = \frac{2\int_0^L \rho(x)\mathcal{Z}(x)\,\mathrm{d}x}{L(\rho h + \rho_* h_*)}, \tag{2.6}$$

where $\rho(x)$ and $\mathcal{Z}(x)$ are the density and the height of the flow inside the jump.

Equation (2.5) can be rearranged in the form of a cubic equation:

$$\left(\frac{h_*}{h} \right)^3 + A_g \left(\frac{h_*}{h} \right)^2 + B_g \frac{h_*}{h} + C_g = 0, \tag{2.7}$$

where A_g, B_g and C_g are defined by:

$$A_g = -\frac{L}{h}\frac{K_0}{k_*}(\tan\zeta - \mu_e),$$

$$B_g = -\frac{2\beta Fr^2 + k + K_0 \frac{L}{h}(\tan\zeta - \mu_e)}{k_* \frac{\rho_*}{\rho}},$$

$$C_g = \frac{2\beta_* Fr^2}{k_* \left(\frac{\rho_*}{\rho} \right)^2}.$$

It is worthy to note that under incompressible ($\rho_* = \rho$), isotropic ($k_* = k = 1$), and plug flow ($\beta_* = \beta = 1$) jump conditions, (2.7) takes the form of a Bélanger-like but implicit relation:

$$\frac{h_*}{h} = \frac{1}{2}(\sqrt{1 + 8\chi Fr^2} - 1), \tag{2.8}$$

where χ is a parameter which measures the deviation from the traditional Bélanger's equation (for the latter, we simply have $\chi = 1$):

$$\chi = \frac{1}{1 - \frac{K_0 L}{h_* - h}(\tan\zeta - \mu_e)}. \tag{2.9}$$

The Bélanger-like equation above is practical to gauge the expected effect of each contribution to the jump height. $\chi > 1$ represent granular jumps which are thicker than horizontal frictionless incompressible jumps, while $\chi < 1$ holds for thinner jumps. The dimensionless parameter $L/(h_* - h)$ appears in the above equation. The measured values from existing laboratory experiments with granular materials will be analysed and compared to the values measured in the tests with hydraulic flows, in §2.3.3.

2.2.2 Standing hydraulic jumps

For hydraulic jumps, the very low viscosity of water has negligible effect, and then is not taken into account like in Bélanger equation. However, in the presence of roughness on the bottom of the flume, we must take into account the turbulent stress acting over the jump length, which takes the following form:

$$\tau_b = f_e \rho {u_J}^2. \tag{2.10}$$

The hydraulic friction coefficient f_e is estimated over the entire length of the jump (see its expression in §2.3.5), and u_J is the velocity averaged over the length of the jump. The latter can be approximated by $u_J \simeq K_0 \frac{\bar{u}+\bar{u}_*}{2}$, which—using mass conservation—yields $u_J = \frac{K_0}{2}\left(1+\frac{1}{h_*/h}\right)\bar{u}$. The turbulent stress reads as follows:

$$\tau_b = f_e \rho \frac{K_0^2}{4}\left(1+\frac{1}{h_*/h}\right)^2 \bar{u}^2. \tag{2.11}$$

Considering an incompressible ($\rho_*/\rho = 1$) and isotropic ($k = 1$ and $k_* = 1$) fluid and combining (2.11) with the continuity equations 2.2 and 2.3 then gives the following relation for a hydraulic flow down an incline:

$$\begin{aligned} 2\beta_* Fr^2 \left(\frac{h_*}{h}\right) - 2Fr^2\beta\left(\frac{h_*}{h}\right)^2 = \left(\frac{h_*}{h}\right)^2 - \left(\frac{h_*}{h}\right)^4 \\ +K_0\frac{L}{h}\left[\left(\frac{h_*}{h}\right)^2 + \left(\frac{h_*}{h}\right)^3\right]\tan\zeta - f_e\frac{K_0^2}{2}Fr^2\frac{L}{h}\left(1+\frac{h_*}{h}\right)^2 \end{aligned} \tag{2.12}$$

The above relation is of degree four. However, if we assume that h_*/h is much greater than 1, this can be simplified to a cubic equation:

$$\left(\frac{h_*}{h}\right)^3 + A_w\left(\frac{h_*}{h}\right)^2 + B_w\frac{h_*}{h} + C_w = 0, \tag{2.13}$$

where A_w, B_w and C_w are defined by:

$$\begin{aligned} A_w &= -\frac{L}{h}K_0\left[\tan\zeta - f_e\frac{K_0}{2}Fr^2\right], \\ B_w &= -\left(2\beta Fr^2 + 1 + K_0\frac{L}{h}\tan\zeta\right), \\ C_w &= 2\beta_* Fr^2. \end{aligned}$$

We have checked that using the equation of degree four, instead of the above cubic equation, does little change for the hydraulic data sets investigated in the present paper. For other hydraulic data for which h_*/h would be close to 1, the equation of degree four should be solved instead.

2.2.3 Cubic relation for both granular and hydraulic jumps

If we define a dimensionless number Γ_e equal to μ_e for grains and to $\frac{1}{2}f_e K_0 Fr^2$ for water, and a parameter λ which takes the value 1 for grains and 0 for water, we obtain a cubic equation valid for both hydraulic and granular flows:

$$\left(\frac{h_*}{h}\right)^3 + A\left(\frac{h_*}{h}\right)^2 + B\frac{h_*}{h} + C = 0, \tag{2.14}$$

with

$$A = -\frac{L}{h}\frac{K_0}{k_*}(\tan\zeta - \Gamma_e),$$
$$B = -\frac{2\beta Fr^2 + k + K_0\frac{L}{h}(\tan\zeta - \lambda\Gamma_e)}{k_*\frac{\rho_*}{\rho}},$$
$$C = \frac{2\beta_* Fr^2}{k_*\left(\frac{\rho_*}{\rho}\right)^2}.$$

For water, we have $k_* = k = 1$ (isotropic fluid) and $\rho_*/\rho = 1$ (incompressible fluid).

The cubic equation, which is exact for grains and an approximation for water, can be solved by using Cardano's method ([12]). After the resolution, the only physically meaningful solution for the depth ratio (real and positive) is the following:

$$\frac{h_*}{h} = 2\sqrt{-\frac{p}{3}}\cos\left(\frac{1}{3}\arccos\left(-\frac{q}{2}\sqrt[3]{\frac{27}{-p^3}}\right)\right) + \frac{1}{3}\frac{L}{h}\frac{K_0}{k_*}(\tan\zeta - \Gamma_e) \tag{2.15}$$

where:

$$q = \frac{2\beta_* Fr^2}{k_*(\frac{\rho_*}{\rho})^2} - \frac{2}{27}\left(\frac{L}{h}\frac{K_0}{k_*}\zeta_\Gamma\right)^3 - \frac{1}{3\frac{\rho_*}{\rho}}\frac{L}{h}\frac{K_0}{{k_*}^2}\zeta_\Gamma\left(2\beta Fr^2 + k + K_0\frac{L}{h}\zeta_{\Gamma,\lambda}\right),$$
$$p = -\frac{1}{k_*\frac{\rho_*}{\rho}}\left(2\beta Fr^2 + k + K_0\frac{L}{h}\zeta_{\Gamma,\lambda}\right) - \frac{1}{3}\left(\frac{L}{h}\frac{K_0}{k_*}\zeta_\Gamma\right)^2.$$

We introduced the notation $\zeta_\Gamma = \tan\zeta - \Gamma_e$ and $\zeta_{\Gamma,\lambda} = \tan\zeta - \lambda\Gamma_e$ (we remind here that $\lambda = 1$ for grains and $\lambda = 0$ for water).

Equation (2.15), which provides the general solution for the height of a standing jump, has up till now never been proposed in literature to our knowledge. The sequent depth ratio, which is a function only of the Froude number in the Bélanger equation, here becomes a function of several variables:

$$\frac{h_*}{h} = \mathcal{F}\left(Fr, \frac{\rho_*}{\rho}, \frac{L}{h}, \tan\zeta, \Gamma_e, K_0, \beta, \beta_*, k, k_*\right). \tag{2.16}$$

In particular, we note that the general relation can predict the height of the standing jump only if another length scale, namely the length of the jump, is known. In the present paper, this relation will be carefully compared to well-documented experiments on standing jumps formed in both hydraulic flows [50, 34, 35, 48, 13] and dry granular flows [19], for which the jump length L was actually measured, in addition to its height h_*.

The important parameters characterizing the deviation from Bélanger's prediction are the shape of the jump (via the parameter K_0), the jump length through L/h in the general solution (see (2.15)) or $L/(h_* - h)$ in the reduced relation for granular jumps (see (2.8)), the gravity force through the slope angle ($\tan\zeta$) and the resistive friction force resulting from the dissipation in the jump caused by the boundary walls (through the dimensionless number Γ_e). In the following section, we revisit in detail the existing laboratory measurements of those parameters by considering both hydraulic and granular flows. This analysis allows us to identify some analogies and differences between the two fluids.

2.3 Hydraulic and granular jumps data revisited and compared

In the present section, we compare the parameters discussed at the end of the previous section, which were measured in a number of experiments under different boundary conditions with either water or dry granular materials.

2.3.1 Types and definitions of the jumps

The data revisited in our study include (i) hydraulic jumps formed down smooth inclines measured by [35], [48], and [50], (ii) hydraulic jumps on a rough bottom by [13] and [34], and (iii) granular jumps down smooth inclines recently studied by [19]. Both granular and hydraulic jumps considered here were formed on a portion of constant slope, with a gate at the outlet. In hydraulics, they are called D-jumps (only the data from D-jumps from the above references about water jumps are studied here). It is also possible to form jumps in the middle of a slope break (the so-called A,B, or C-jumps in hydraulics).In the present paper, the jump we consider separates two flow conditions: the incoming supercritical flow where the free-surface is parallel to the bottom (i.e. $\tan\zeta - \mathrm{d}\mathcal{Z}/\mathrm{d}x = \tan\zeta$), and the downstream subcritical flow where, the angle of the free surface becomes constant ($\tan\zeta - \mathrm{d}\mathcal{Z}/\mathrm{d}x = 0$ for hydraulic flows, or $\tan\zeta - \mathrm{d}\mathcal{Z}/\mathrm{d}x = \tan\zeta_0$ for dry grains). The jump is defined as the part of the flow between those two zones, thus corresponding to the flow region $0 \leq x \leq L$ in figure 2.1. This allows to define the length L, and the heights $h \equiv \mathcal{Z}(x = 0)$ and $h_* \equiv \mathcal{Z}(x = L)$. Note that the flows of dry granular materials are compressible, thus producing compressible jumps. In particular, compressible jumps were recently addressed by [19] who carefully estimated the density change across the jump ρ_*/ρ in their experiments. Based on this definition of L, figure 2.2a shows examples of the shape of granular jump profiles evolving with the Froude number, as measured in the laboratory by [19].

2.3.2 Variation of the shape factor K_0

The shape factor K_0, defined by (2.6), is useful to estimate the averaged value over the jump length of physical quantities (see for instance the estimation of u_J) that depend on the position within the jump. The shape factor was only measured by [35] and [48] for hydraulic jumps, and by [19] for granular jumps. Figure 2.2b shows how the shape factor K_0 measured in the aforementioned studies varied with the Froude number Fr of the incoming flow. Data by [35] for water, and by [19] for granular fluids, are remarkably of the same order of magnitude. Both data show that K_0 increases with Fr. This trend was however not observed by [48] who found a nearly constant K_0 (equal to 1) in their experiments with water, though the range of Fr which they investigated was similar. Note that a slight decrease of K_0 with slope was observed by [48]. However this decrease is not observed by [35]. In the present paper (see §2.4), we will consider $K_0 = 1$ for other experimental studies for which K_0 was not directly measured or estimated: this concerns the data by [50] for water jumps down a smooth incline, and by [13] and [34] for water jumps on a rough bed.

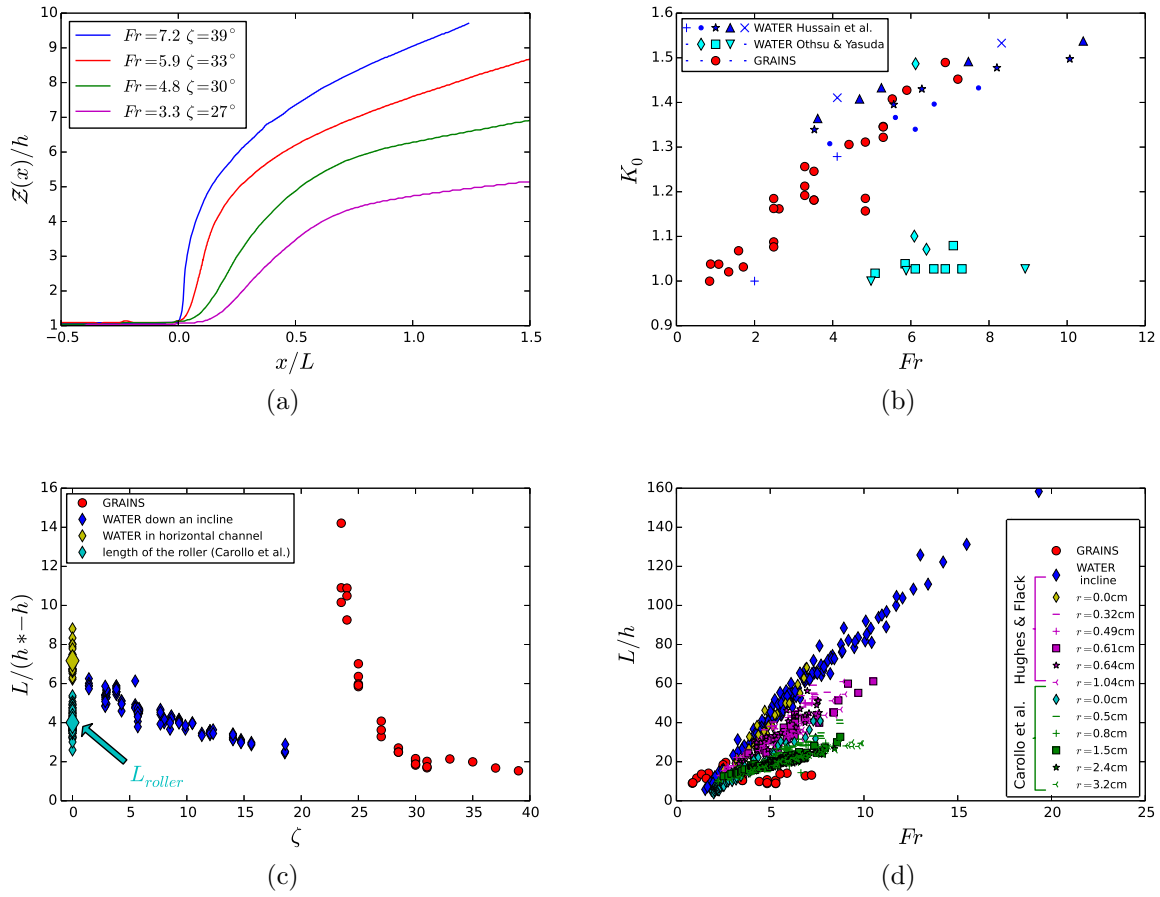

Figure 2.2: (a) Examples of normalized granular jump profiles showing a transition from diffuse to steep jumps, from [19]. Comparison of parameters that play a role in (2.15), or (2.8): (b) K_0 versus Fr; (c) $L/(h_* - h)$ versus ζ; (d) L/h versus Fr. The following conditions are considered: water flows down an inclined channel (data from [48, 35]), water flows on a rough bed (data from [13, 34]), and flows of dry granular materials (data by [19]). Note that in figure 2.2c, the data by [13] is below all other data with water because this the length of the roller, L_r, which was measured instead of the jump length (see figure 2.1a and text for explanation). For $\zeta = 0$, a great number of tests were conducted, and the data showed a scatter related to some effect of Fr (figure 2.2c): we then show a bigger symbol that corresponds to the average value.

2.3.3 Variation of the relative length $L/(h_* - h)$

The relative length $L/(h_* - h)$, which appears in the simplified implicit relation (2.8) derived from the assumption $\rho_*/\rho = 1$ in the case of granular jumps, is analysed here. With both grains and water, $L/(h_* - h)$ is a decreasing function of the slope, as shown in figure 2.2c. It is worth noticing that $L/(h_* - h)$ reaches a finite value around $6-8$ for water flows at $\zeta = 0$, as shown in figure 2.2c. Such a range is consistent with values reported by a number of earlier studies, as for instance in [55] and [2]. For valuable reviews which summarize the great number of experimental data on the length of hydraulic jumps, one can mention the works by [29] and, more recently, by [63]. It should be noted that in the paper of [13] it is not the total length of the jump L, but the length of the roller L_r which was measured (see sketch in figure 2.1a). However, the sequent depth was not measured at the end of the roller but—like in the other papers—at the end of the jump. Strictly, (2.15) should apply to L and h_* or to L_r and the flow height at the end of the roller, but should not apply to L_r and h_*. The length of the roller is generally smaller than the length of the jump and approaches the latter when the Froude number increases, as reported by [54]. Such a difference between L and L_r becomes clear at $\zeta = 0$ and $r = 0$. For an horizontal smooth bed, $L/(h_* - h)$ is around 7 (data of [35], [50], and [34] shown by yellow points in figure 2.2c), while $L_r/(h_* - h)$ is around 4 (data of [13] shown by turquoise points in figure 2.2c).

Steady granular flows can only occur above a slope angle ζ_0, which was about 23° in the laboratory test by [19]. No jump can form below this limit angle, and when $\zeta \mapsto \zeta_0$, the relative length of the jump $L/(h_* - h)$ starts diverging, as seen in figure 2.2c. However, for higher values of ζ, the values seem to align with the data with water. The Froude number of granular flows is mainly controlled by the slope angle, and decreases with slope. In contrast, it is possible to form supercritical water flows at high Fr (far above the critical Froude number) on low slope angles, which can then produce strong hydraulic jumps of finite length. While approaching the slope ζ_0, Fr tends towards the critical Froude number, meaning that simultaneously h_* approaches h: the jump is more and more diffuse and finally disappears, as observed by [19]. The behaviour of granular jumps close to ζ_0 would need further investigation.

2.3.4 Variation of the relative length L/h

Figure 2.2d shows how the jump length relative to the height of the incoming flow evolves with the Froude number. The behaviour of the relative length of the jump, L/h, changes strongly between dry granular flows and hydraulic flows. For granular jumps, L/h is almost independent of Fr, and relatively small (around $10 - 20$ in the tests by [19]), by comparison to the value obtained with hydraulic jumps (from 10 to 160). Those results suggest that the friction between grains is able to dissipate efficiently the energy of the incoming flow, over a relatively small distance.

On the contrary, figure 2.2d suggests that the relative length of the jump L/h is highly correlated with the Froude number in hydraulic flows, whether the channel is inclined or horizontal, smooth or rough. At a given Fr, it is clear from figure 2.2d that the relative length of the jump is smaller if the bottom is rough, and it decreases as the typical roughness size increases. This means that a rough channel bottom is more able to dissipate energy than a smooth one. This result shows the key role played by the friction forces acting within the jump volume, thus justifying the general jump relation which we are proposing here.

Interestingly, the slope has no effect on the relative length L/h of the jumps formed on

a smooth bottom: the blue points for the jumps in water flows down a smooth incline, and the yellow points for the jumps in water flows on a horizontal smooth bottom, are aligned in figure 2.2d. This means that at a given Fr, the jump length is only proportional to the height of the incoming flow and does not depend on the slope angle. We will propose simple closure relations for L/h in §2.4.4

2.3.5 Depth-averaged friction laws derived using minimal assumptions

Determining the dimensionless number Γ_e, namely the effective friction coefficient μ_e within the granular jump or the hydraulic friction coefficient f_e within the hydraulic jump, is of course a very challenging question, linked to the rheology of the fluid at stake, the system size and/or the boundary conditions (bottom roughness in particular). We adopt here a back-analysis strategy. In the first step, we compute the exact values of Γ_e needed to match (2.15) to the experimental data. In the second step, we compare those exact values to the predictions from friction laws derived using minimal assumptions under which the dimensionless number Γ_e is a function of the incoming flow features. In the present section, we consider $\beta = \beta_* = 1$ and $k = k_* = 1$ in (2.15). Those assumptions will be discussed in §2.3.6.

Friction law for hydraulic flow on a rough bottom

Based on the phenomenological theory of Kolmogórov, [22] proposed to calculate the turbulent friction coefficient f_e in rough pipes with the following formula:

$$f_e = \kappa_\tau \kappa_u \left(\frac{r}{R_h} + ab\Re^{-3/4} \right)^{1/3}, \tag{2.17}$$

where κ_τ and κ_u are dimensionless numbers, and a and b are constants (see more details in [22] for typical values for flows in rough pipes), R_h is the hydraulic radius which is equal to $(Wh)/(W+2h) \approx h$ for the free-surface flows investigated here, r is the typical roughness size, and $\Re = \bar{u}R_h/\nu \approx Fr\sqrt{g}h^{3/2}/\nu$ is the depth-averaged Reynolds number (ν being the fluid viscosity).

For the data revisited in the present study, the Reynolds number was always larger than 10^7. We can therefore neglect the influence of $\Re$ in (2.17) and express the dimensionless number Γ_e (with $R_h \sim h$):

$$\Gamma_e = \frac{1}{2} K_0 \kappa_\tau \kappa_u \left(\frac{r}{h} \right)^{1/3} Fr^2 \tag{2.18}$$

Figures 2.3a and 2.3c show the values of Γ_e back-calculated from the general jump relation, namely (2.15), as a function of the Froude number for the data from [34] and [13], respectively (For the data of [50], [35] and [48], the bottom is smooth, then $r = 0$ and $\Gamma_e = 0$). At a given Froude number, Γ_e is higher for higher r and, at a given r, Γ_e increases with Fr. Those trends are compatible with the friction law given by (2.18) (see black circle symbols representing the turbulent friction law for some specific values of r in Figs. 2.3a and 2.3c). Figures 2.3b and 2.3d depict the best calibration of $\kappa_\tau \kappa_u$ to fit the dimensionless number Γ_e extracted from the hydraulic friction law ((2.18)) on the Γ_e derived from the general jump relation (2.15) for the data from [34] and [13], respectively. Though some scatter is observed, the results of the calibration show that (2.18) is suitable for describing the value of Γ_e within the jump provided that the product $\kappa_\tau \kappa_u$ is

taken equal to 0.0086 for the data of [13], and equal to 0.0026 for the data of [34]. Those two values of $\kappa_\tau \kappa_u$ have the same order of magnitude, both leading to a f_e compatible with typical values for hydraulic turbulent friction. A number of sources may explain the difference however: some discrepancies in the geometry of the experimental set-up, some differences in the way of estimating r in the two studies and, first of all, the fact that the calculated Γ_e from the general jump relation in [13] uses the roller length, L_r, instead of the jump length L (see previous discussion in §2.3.3) . Though the above questions remain open, (2.18) will be used in §2.4, as a good approximation of basal effective friction within the water jump on a rough bottom.

Friction law for granular flows

It is still a challenging question to predict accurately the friction law for granular flows down rough or smooth inclines, though many valuable studies were conducted in the past recent years, as recently reviewed by [39] and references therein. In the present paper, we use a minimal assumption that the effective friction μ_e is given by the sum of a constant Coulombian-like friction coefficient, associated with the slope above which flows are possible, and a turbulent-like friction proportional to the square of the Froude number of the incoming flow, associated with the inertial forces that come into play at high Fr:

$$\mu_e = \mu_s + \alpha Fr^2, \tag{2.19}$$

where μ_s and α are the two parameters needed for the friction law. Such a law can be seen as a rough approximation of a number of granular flow models proposed in recent studies, and capable of covering a wide range of shallow flow conditions from dense inertial, liquid, flows to high-speed collisional, gaseous, flows [42, 5, 33].

Figure (2.4a) shows the friction μ_e derived from the general jump relation, namely (2.15), as a function of the Froude number. We remind that μ_e corresponds to an effective coefficient of friction estimated over the entire length of the jump. The data is compatible with the friction granular law given by (2.19). We can match (2.19) to the experimental data on granular jumps down a smooth incline reported by [19], and the best fit is found with $\mu_s = 0.38$ and $\alpha = 0.0068$. $\mu_s = 0.38$ is equivalent to a friction angle of 20.8°. The results are displayed in figure 2.4b. Note that if μ_s is estimated as equal to $\arctan(\zeta_0)$, in accordance to $\zeta_0 = 23°$ as reported by [19], it yields $\mu_s = \tan\zeta_0 = 0.42$ and we obtain the best match between μ_e calculated with (2.19) and μ_e back-calculated by fitting the general jump relation (2.15) with $\alpha = 0.0053$.

Note that [19] proposed a different analysis by considering a depth-averaged $\mu(I)-$rheology spatially integrated over the length of the jump. Their analysis was successful at demonstrating that the $\mu(I)-$rheology holds inside the volume of the jump. However, their approach was not predictive because μ_e was a function of the depth-averaged inertial number of the jump (averaged value over the length of the jump), which was by construction a function of the downstream jump features (h_*, $\bar{u}_*$ and ρ_*), in addition to the upstream jump features. Moreover, their analysis was limited to non-accelerating slopes for which flows were relatively dense, as detailed in [19]. Other laws exist to improve the $\mu(I)-$rheology, like the one proposed by [71], but they have many parameters and still do not take into account the inertia at high Froude numbers. In contrast, the more simple closure relation proposed here for friction, namely (2.19), can be predictive in the sense that we seek μ_e as a function of the incoming flow features only (h and $\bar{u}$). Moreover, it can be extended to fast accelerating and more dilute flows for which resistive forces proportional to $\bar{u}^2$ are no longer negligible.

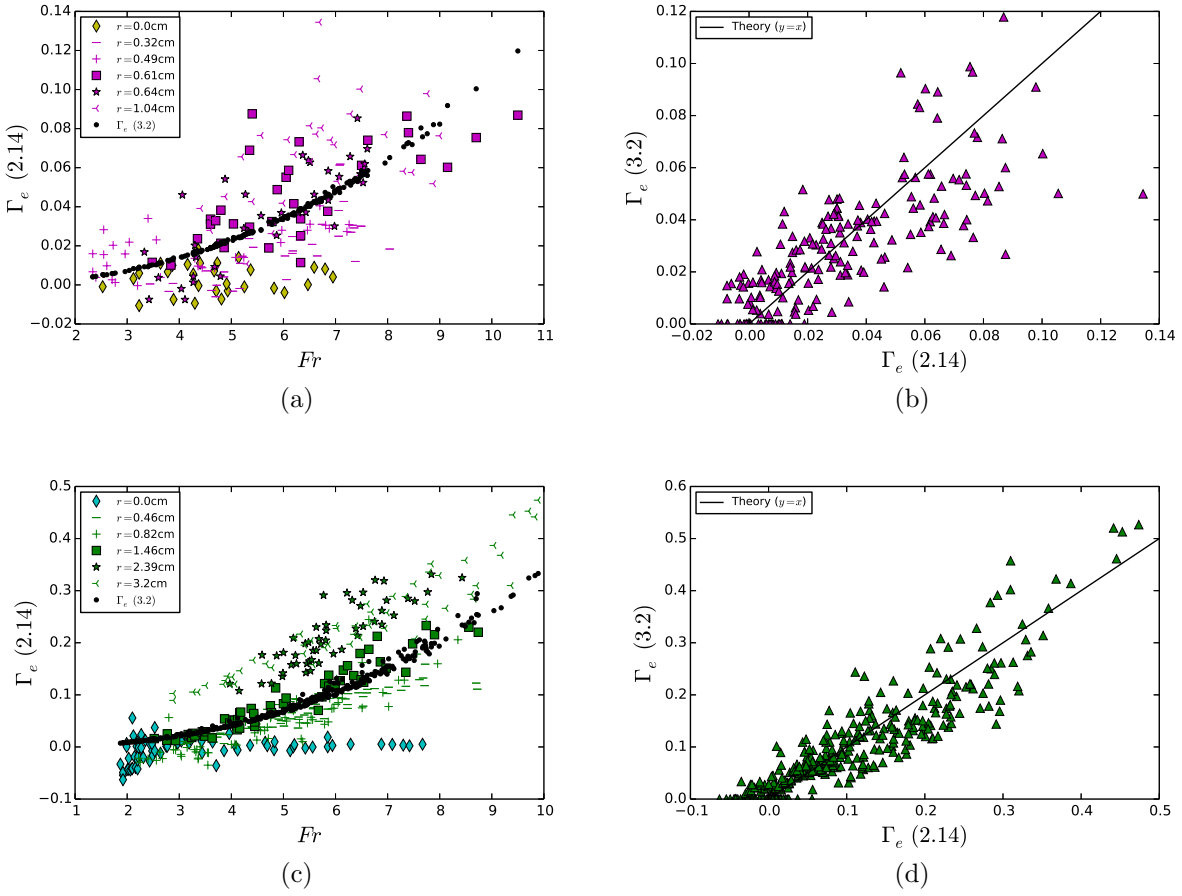

Figure 2.3: Calibration of $\kappa_\tau \kappa_u$ in the friction law given by (2.18) for water flows on a rough bed: (a) Γ_e derived from the jump relation as a function of the Froude number for data from [34]; (b) Best match between Γ_e calculated from (2.18) and Γ_e back-calculated from the data and (2.15) obtained with $\kappa_\tau \kappa_u = 0.0026$ for data from [34]; (c) Γ_e derived from the jump relation as a function of the Froude number for data from [13]; (d) Best match between Γ_e calculated from (2.18) and Γ_e back-calculated from the data and (2.15) with $\kappa_\tau \kappa_u = 0.0086$ for data from [13] (calculation with L_r). In figure 2.3a (figure 2.3c respectively), the black circle symbols depict a prediction from (2.18) with $r = 0.64$cm ($r = 1.5$cm respectively).

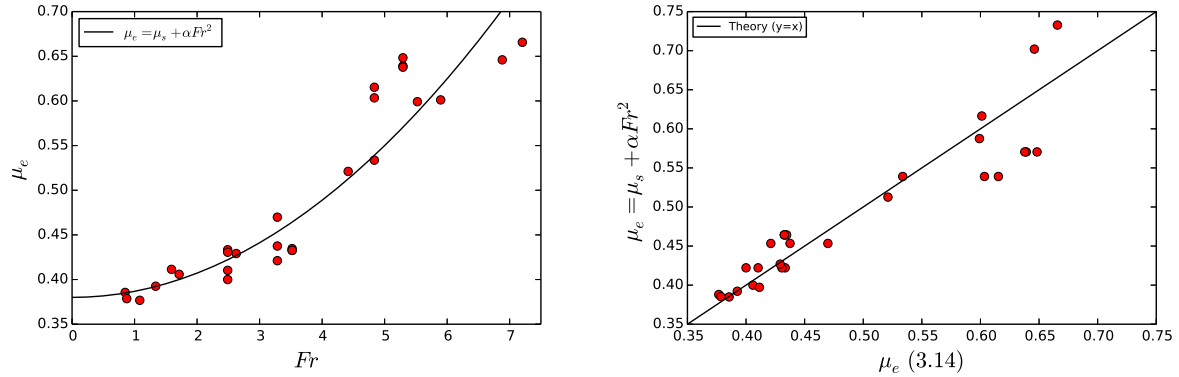

(a) (b)

Figure 2.4: Calibration of μ_s and α in the friction law given by (2.19) for dry granular flows: (a) μ_e derived from the jump relation as a function of the Froude number for data from [19]; (b) Best match between μ_e calculated from (2.19) and μ_e back-calculated with the data and (2.15) obtained with $\alpha = 0.0068$ and $\mu_s = 0.38$ for data from [19].

2.3.6 Discussion on other parameters in general jump relation: ρ_*/ρ, k, k_*, β and β_*

When the fluid at stake is compressible, it is important to consider the change in density across the jump. Such an effect has been recently identified by [19] who investigated standing jumps formed in dilute granular flows. Their study clearly showed the transition towards highly compressible jumps when the incoming granular flow became dilute. Not taking into account the change in density ρ_*/ρ across the jump leads to a prediction which overestimates the jump height (see figure 10 in [19]), itself being reduced by the energy dissipated (through collisions) to transit from a dilute supercritical flow to a much denser subcritical flow.

In the present study, the parameters k, k_*, β, and β_* were all taken equal to 1. This choice is strictly valid for fast hydraulic flows only.

The parameter β is defined as the ratio between the depth-averaged value of the velocity square and the square of the depth-averaged velocity: $\beta = \bar{u^2}/\bar{u}^2$. It depends on the shape of the velocity profile: $\beta = 1$ for plug flows, $\beta = 4/3$ for a linear velocity profile, and $\beta = 5/4$ for a Bagnold velocity profile. [19] reported sliding velocities at the base of their granular flows and Bagnold-like velocity profiles above it. The theoretical value of β for such velocity profiles is given by the following relation:

$$\beta = 1 + \frac{9}{100\frac{\delta}{\gamma} + 36}, \tag{2.20}$$

where $\delta = u_b^2 + \frac{6}{5}A(\zeta)\sqrt{gd}\left(\frac{h}{d}\right)^{3/2} u_b$ and $\gamma = A(\zeta)^2 gd\left(\frac{h}{d}\right)^3$. The sliding velocity u_b is taken at the base of the flow, d denotes the grain diameter, and $A(\zeta)$ the Bagnold constant which is a function of the slope angle. Note that for any positively defined values for δ and γ in (2.20) above, the value of β can only vary between 1 and 1.25. Indeed, using the values measured by [19] for u_b and $A(\zeta)$, we find β varying from 1.04 (at the highest ζ) to 1.2 (at the lowest ζ). Taking $\beta = 1$ for the incoming flows before the jumps is then reasonable for the highest slopes (high Fr), while it is an underestimate at the lowest slopes (low Fr). The velocity profiles downstream of the granular jump were not measured, thus preventing

an estimation of β_*. A recent study by [59] has shown the importance of accounting for the exact value of β while deriving the rheology of dense granular flows down inclines. A similar approach will need to be conducted in the future to investigate how the relation proposed for jumps can be influenced by the values of β and β_*.

The coefficient k relates the normal stresses σ_{xx} and σ_{zz} through the relation $\sigma_{xx} = k\sigma_{zz}$. A number of studies consider $k = 1$ for flows of dry granular flows, as described by—among other studies—[64] and [51]. Other studies propose to extend soil mechanics concepts to the dynamics of granular flows and calculate k as an earth pressure coefficient, as reported for instance by [60]. As discussed by [18], it is most likely that $k = 1$ is relevant for the incoming steady uniform, or slightly accelerating flow (before the jump), while k_* might be different from 1 in the decelerating flow after the jump. Extensive discrete element simulations on granular jumps, in light of the recent simulations on three-dimensional steady and uniform flows performed by [70], are needed in the future in order to check the validity of this assumption.

2.4 General jump relation versus laboratory experiments

2.4.1 Hydraulic, incompressible, jump down a smooth incline: $\Gamma_e = 0$, $\rho_*/\rho = 1$

We consider here hydraulic flows down a smooth incline. The standing jumps are then modelled by frictionless ($f_e = 0$ giving $\Gamma_e = 0$) and incompressible ($\rho_*/\rho = 1$) conditions. Because of the slope ζ, we must take into account the component along the slope of the weight of the jump acting within the jump volume. This situation should be well described by (2.15) with $\rho_*/\rho = 1$ and $\Gamma_e = 0$. Figure 2.5a depicts the sequent depth ratio as a function of the Froude number for different slope angles ζ, as reported by [35], [48], and [50]. As expected, increasing the slope ζ produces jumps thicker than those predicted by Bélanger's equation (line in figure 2.5a) and the gap increases with ζ. By considering $\Gamma_e = 0$ ($f_e = 0$), $\rho_*/\rho = 1$, the values actually measured in the experiments for L/h and K_0, and the input value of $\tan\zeta$, we verify that the jump height measured in the experiments can be predicted by (2.15) whatever ζ (see blue diamond symbols in figure 2.7a, which is provided in §2.4.4).

2.4.2 Hydraulic, incompressible, jump on rough horizontal channel: $\Gamma_e \neq 0$, $\rho_*/\rho = 1$

In the situation analysed here, the fluid is still incompressible ($\rho_*/\rho = 1$), the slope is zero ($\tan\zeta = 0$) but a turbulent friction between the fluid and the bed exists ($f_e \neq 0$ yields $\Gamma_e \neq 0$) because of the presence of a rough bed, described by the roughness coefficient r. When r is null, the system is described by Bélanger's equation, and when it is not, (2.15) has to be used with $\rho_*/\rho = 1$ and $\tan\zeta = 0$. Figure 2.5b displays the sequent depth ratio as a function of the Froude number for different bed conditions, as reported by [13] and [34]. As expected, increasing the bed roughness leads to jumps thinner than those predicted by Bélanger's equation (line in figure 2.5b) and the gap between the experiments and Bélanger's equation increases with r. Moreover, at a given r, it is observed that the gap between Bélanger equation and the experiments increases when Fr increases. By considering $\tan\zeta = 0$, $\rho_*/\rho = 1$, the values measured for L/h and K_0, and a Γ_e that

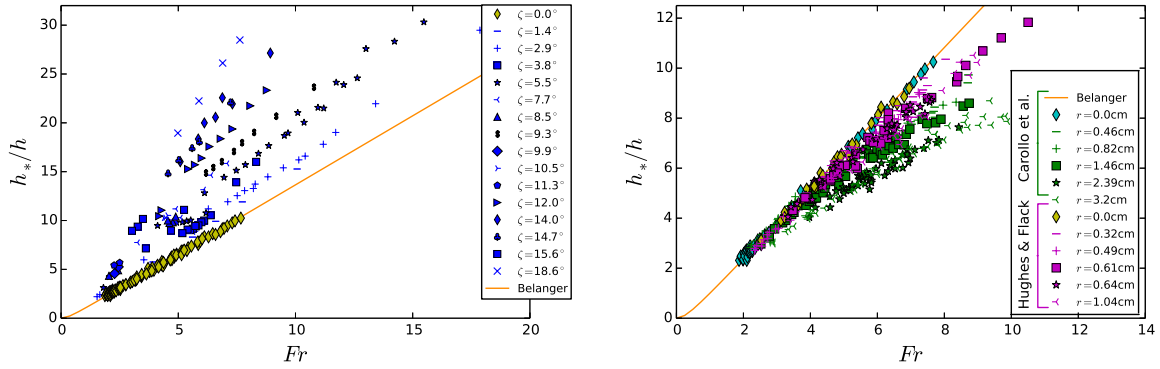

(a) (b)

Figure 2.5: Sequent depth ratio of standing water jumps, as a function of the Froude number, formed in hydraulic flows down smooth inclines, as reported by [35], [48] and [50] (a), and in horizontal flows down a rough bottom, as reported by [13] (b). The continuous line depicts the prediction of the Bélanger's equation in both graphs.

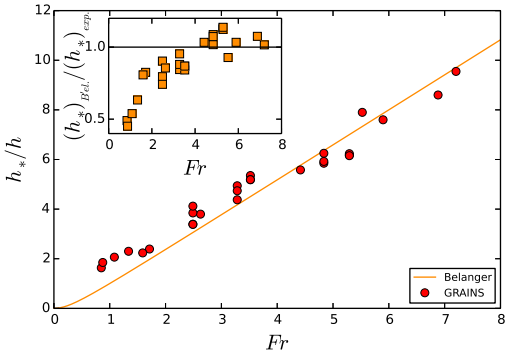

Figure 2.6: Sequent depth ratio for dry granular materials flowing down an incline versus the Froude number (laboratory data reported by [19]), compared to Bélanger's equation (continuous line). Inset: Sequent depth ratio calculated with Bélanger's equation, scaled by the sequent depth ratio measured in the experiments by [19].

follows a turbulent friction law given by (2.18), we verify that the exact jump height can be predicted by (2.15) whatever r and Fr (see triangle symbols in green and magenta shown in figure 2.7a, which is provided in §2.4.4).

We have checked that using the equation of degree four (see (2.12) in §2.2.2) does little change to the results displayed in figure 2.7a, thus showing that the cubic equation is a good approximation for water jumps.

2.4.3 Granular, compressible, jump on a smooth incline: $\mu_e \neq 0$, $\rho_*/\rho \neq 1$

For granular flows, all parameters of (2.15) come into play. Flows of granular materials are compressible ($\rho_*/\rho \neq 1$) and frictional ($\Gamma_e = \mu_e \neq 0$) flows, and they can occur only if the slope is greater than a limit angle ($\tan\zeta > \tan\zeta_0 \neq 0$). All those effects are included in (2.15).

Figure 2.6 shows the sequent depth ratio for standing jumps formed in granular materials down an incline versus the Froude number, as reported by [19]. The Bélanger equation (line in figure 2.6) looks to predict quite well the sequent depth ratio of granular jumps at high Froude numbers, for which the effect of the difference between $\tan\zeta$ and μ_e is relatively small, but it is not true for lower values of the Froude numbers. The prediction of Bélanger equation becomes very poor at low Fr, as shown in the inset of figure 2.6 which reports the values of h_*/h predicted by Bélanger's equation (square symbols) versus the values of h_*/h actually measured in the laboratory tests. By considering the values of ρ_*/ρ, L/h and K_0 measured by [19], as well as the exact values of $\tan\zeta$, and a μ_e that follows the friction law given by (2.19), we verify that we can reproduce the height of granular jumps measured in the laboratory (see red-coloured circle symbols in figure 2.7a) whatever the value of the Froude number of the incoming flow.

2.4.4 Analysing both water and granular fluids

Figure 2.7 displays the height of the jumps predicted by the general relation proposed for jumps as a function of the height of the jumps actually measured in both water and granular fluids.

Verification of calibration regarding the friction laws

The collapse of the height of the jump shown in figure 2.7a is a verification of our calibration procedure regarding the friction laws. It was obtained by feeding the general solution, given by (2.15), with the values actually measured in the experiments for K_0 (or taken equal to 1 when it was not known: [50], [13] and [34]), L/h, and ρ_*/ρ (when the latter ratio was not 1: dilute granular flows), and by using minimal assumptions for the dimensionless number Γ_e depending on the fluid and/or bottom roughness under consideration. The calibrated value used for $\kappa_\tau\kappa_u$ for water, and μ_s and α for dry grains, are given in §2.3.5 and §2.3.5, respectively.

Prediction using simple relations for L/h and K_0

The general relation can predict the height of the jump only if another length scale, namely the jump length, is known. In order to make the general relation predictive, it is interesting to push forward our analysis by proposing an empirical law for L/h instead of using the values actually measured of the laboratory experiments. Back to the variation of L/h observed in the experiments (see figure 2.2d), it appears to be reasonable to approximate the jump length by a linear function of the Froude number for the water flows:

$$\frac{L}{h} = c(Fr - 1), \tag{2.21}$$

where c takes the following values: $c = 9.76$ for the smooth bottom, $c = 7.71$ for the rough bottom in [34] and $c = 4.54$ for the rough bottom in [13]. Note that the latter value is much lower because it is based on the roller length, which is smaller than the jump length. If we exclude those measurements based on the length of the roller, a reasonable value of c to match the maximum of the measurements on the length of water jumps would be 8.7 (mean value stemming from the data on a smooth bottom and the ones on a rough bottom by [34]). The above law assumes that the jump length vanishes ($L = 0$) when Fr reaches unity, which is the critical Froude number for water. Predicting theoretically the length of the jump is still a question not resolved in hydraulics. There are a number of

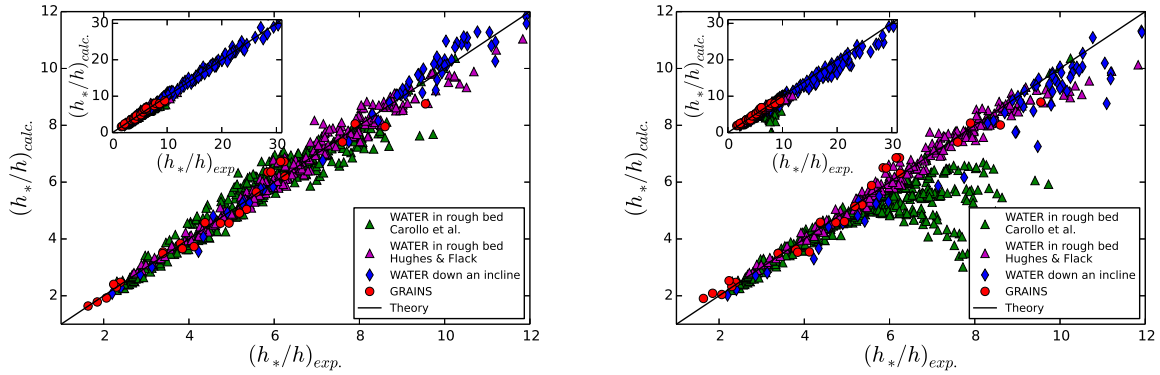

(a) (b)

Figure 2.7: Sequent depth ratio calculated with (2.15) under minimal assumptions on closure relations for friction (when relevant: see text), versus the measured sequent depth ratio in experiments with water or dry grains: verification using the values of L/h actually measured (a), and prediction using empirical but simple closure relations for L/h depending on the fluid type (b). The insets show all the data available and revisited in the present paper, while the main graphs are a zoom on values of h_*/h smaller than 12 that correspond to a wide spectrum of fluid and boundary conditions.

experimental studies on the length of hydraulic jumps, and a number of empirical laws were proposed for L/h, as reviewed by [29] and [63]. Equation (2.21) reproduces well the data shown in figure 2.2d and is similar to the equation proposed earlier by [65].

The relative jump length is—in strong contrast to water—nearly constant for the dry granular flows (see red circles in figure 2.2d). The mean value extracted from the data by [19] is:

$$\frac{L}{h} \simeq 14.1, \tag{2.22}$$

and the median value is 12.3. Figure 2.7b shows the height of the jump predicted by (2.15) fed with the above closure relations for L/h (instead of using the measured values for L/h), while keeping the calibrated parameters for the friction laws (values of $\kappa_\tau \kappa_u$ for water flows on a rough bed, and of μ_s and α for the dry granular flows, discussed in §2.3.5 and 2.3.5, respectively). We use $L/h = 14.1$ for grains, and $L/h = c(Fr - 1)$ with $c = 8.7$ for water. In addition, we systematically consider $K_0 = 1$. The collapse between the laboratory data and the analytical prediction remains very good for most of the data, which shows the robustness of the general relation proposed fed with simple closure relations for μ_e and L/h. The high values of h_*/h measured by [13] is discarded from the analytical prediction in figure 2.7b because it corresponds to conditions for which the gap between L_r (the roller length) and L (the jump length) is the highest.

2.5 Discussion and conclusion

The present paper presented a general explicit relation for the prediction of the sequent depth ratio (h_*/h) of standing jumps formed in free-surface flows, which was derived from depth-averaged mass and momentum conservation applied to the control-volume surrounding the jump. We obtained a cubic equation for grains and an equation of degree

four for water. The latter can be approximated by a cubic equation, as long as we have h_*/h much greater than 1. The cubic equation, which is exact for grains and a reasonable approximation for water, could be solved by Cardano's method. By revisiting different laboratory configurations involving (i) water flows on a horizontal smooth bed or down smooth inclines, (ii) water flows on horizontal rough beds, and (iii) dense and dilute flows of dry granular materials down a smooth incline, we were able to clearly delineate the importance of each contribution to the height of the standing jumps, as fully predicted by the general relation proposed. Our study demonstrates that this general relation is robust for a wide range of experimental conditions in the laboratory. The sequent depth ratio of the standing jump is not a function of the Froude number only. This clearly shows the limits of the traditional Bélanger equation that stems from a Rankine-Hugoniot relation and assumes—by construction—that the jump volume shrinks into a singular surface. The sequent depth of the jump is a function of the slope inclination: at a given Fr, water jumps formed down a smooth incline are thicker than those formed on a horizontal smooth bed, which highlights the crucial role played by the component of the jump weight along the slope (figure 2.5a). It is also a function of the resistive friction force: at a given Fr, horizontal water jumps formed on a rough bed are thinner than those formed on a smooth bed, because energy is dissipated by friction (figure 2.5b). At low Fr, the standing jumps formed in dense flows of dry granular materials are thicker than those predicted by the Bélanger equation (see inset of figure 2.6), because the contribution due to the jump weight reduced by the granular friction force (apparent weight along the slope) comes into play. At higher Fr, the latter contribution of the apparent weight of the jump—which tends to increase the jump height, is counter-balanced by the decrease in density across the jump—which tends to decrease the jump height. This competition explains why standing jumps formed in fast dilute flows of dry granular materials remain however well predicted by the traditional Bélanger equation (high Fr in inset of figure 2.6), as observed by earlier studies [8, 26].

In order to take into account the forces acting within the jump volume, it is needed to feed the new general relation with the relative jump length (L/h) and with an information on its shape (K_0), as well as with a closure relation for the friction force. In the present paper, we cross-compared the existing laboratory data to derive simple yet relevant closure relations for the friction laws, as discussed in §2.3.5 and §2.3.5. Back to figure 2.2d, the variation of L/h as a function of the experimental configuration (boundary conditions, rheology of the fluid at stake) is quite complicated. L/h appears to depend weakly on Fr for dry granular materials, while it increases (roughly) linearly with Fr for water but the increase rate with Fr depends on the bottom roughness. As a conclusion to our study, it appears crucial to devote future research to the length of the standing normal jumps and, to a lesser extent, the shape of the jump. Understanding how the geometry of the standing jumps varies with the boundary conditions, the system size, and the nature of the fluid in consideration, and thus how it is coupled with the basal effective friction, appears to be a promising approach to further understand the rheology of complex fluids such as granular flows. Future work should systematically investigate the assumption of decoupling the jump length, L/h, and the parameters that characterize the dimensionless number Γ_e (namely μ_s and α for grains, and f_e for water). Regarding the theoretical aspects presented in the current paper, it is worthwhile to note that deriving an equation for energy conservation—in addition to mass and momentum conservation, would open a path to predict the geometry of the jump (size and shape) but this remains a challenging issue.

Chapter 3

Discussion on resistive forces across water jumps

This chapter presents a correction and a discussion on a particular point in the previous article. In the previously published chapter in 2017 [44], an error was introduced that affects the derived equation for water jumps, in the term related to the resistive force acting across the jump. Here, this term is corrected, that is followed by a discussion about the form that the resistive force across the water jumps could take, in order to capture the effect of the roughness on the height of water jumps evidenced by experimental data.

3.1 Correction of the equation for water jumps

3.1.1 An error in the resistive force term

In the previous article (Chap. 2), we tried to obtain a general equation for water jumps which would take into account any type of jump, including jumps formed in a sloping or rough channel. Section 2.2.2 was dedicated to the finding of this equation. The starting points are the mass and momentum conservation equations:

$$\begin{cases} \rho u_* h_* = \rho u h. \\ \rho u_*^2 h_* - \rho u^2 h = \rho \frac{1}{2} g h^2 \cos\zeta - \rho \frac{1}{2} g h_*^2 \cos\zeta + w \sin\zeta - \tau_b L. \end{cases} \tag{3.1}$$

However, we realized after publication [44] that we made a mistake in transitioning from Eq. (2.12) to Eq. (2.13) which had affected the term that takes into account the resistive force across the water jump.

The corrected form of the equation for the water jumps is therefore as follows (Eq. (2.12)):

$$\begin{aligned} 2\beta_* Fr^2 \left(\frac{h_*}{h}\right) - 2Fr^2\beta \left(\frac{h_*}{h}\right)^2 = \left(\frac{h_*}{h}\right)^2 - \left(\frac{h_*}{h}\right)^4 \\ + K_0 \frac{L}{h} \left[\left(\frac{h_*}{h}\right)^2 + \left(\frac{h_*}{h}\right)^3 \right] \tan\zeta - f_e \frac{K_0^2}{2} Fr^2 \frac{L}{h} \left(1 + \frac{h_*}{h}\right)^2 \end{aligned} \tag{3.2}$$

If we apply to this equation the approximation as in the previous chapter, considering that the jump height ratio h_*/h is always much greater than 1, the correct form of Eq. (2.13) is:

$$\left(\frac{h_*}{h}\right)^3 + A_w \left(\frac{h_*}{h}\right)^2 + B_w \frac{h_*}{h} + C_w = 0, \tag{3.3}$$

where A_w, B_w and C_w are defined by:

$$A_w = -\frac{L}{h} K_0 \tan\zeta,$$
$$B_w = -\left(2\beta Fr^2 + 1 + K_0 \frac{L}{h}\tan\zeta - f_e \frac{K_0^2}{4} Fr^2 \frac{L}{h}\right),$$
$$C_w = 2\beta_* Fr^2.$$

The mistake was made on the frictional term that operates in the B_w term (function of h_*/h) instead of the A_w term (function of $(h_*/h)^2$). We understand that the frictional term will have less effect in the correct equation (Eq. (3.3)) than in the erroneous equation (Eq. (2.13)).

3.1.2 Possible effect on the general relation

Figure 3.1 shows the prediction of the equation for the water jumps with the initial mistake, but that can be considered as a fit of the experimental data by [13] and [34] (red cruxes). Fig. 3.1 also shows the prediction of both the corrected equation (blue points) and its approximation (blue "plus" symbols), and the prediction of Bélanger equation (Eq. (2.1), orange line).

We see that the mistake does not change anything for the effect of the slope of the channel, but changes the result for jumps with a frictional bottom. The corrected equation predicts almost no effect on the jump height ratio when friction is added to the bottom of the channel in a water jump. This is in contradiction with the experimental results by [13] and [34], fitted with the red cruxes: when roughness is added to the bottom of a chute with no slope, the induced friction has a significant effect on the jumps created. The jump height ratio h_*/h is lower than the height ratio of a jump in a smooth base, and increasing friction, the jump height ratio reduces (see Fig. 2.5b). Another effect is the decrease of the relative jump length L/h, up to twice as small as a jump on a smooth base (see Fig. 2.2d).

This means that our definition of the resistive force across a water jump induced by roughness on the base of the chute is not relevant.

3.2 Resistive force across rough water jumps

3.2.1 New expression for velocities inside water jumps

As already stated in the previous chapter (Chap. 2 or [44]), the resistive force across the water jump is supposed to take the following form:

$$\tau_b = f_e \rho u_J^2. \tag{3.4}$$

However, the present corrected equation (Eq. (3.3)) is not describing the reality observed in the laboratory experiments. One improvement could come from the averaged velocity inside the jump u_J. In Eq. (3.3), we decided to approximate the velocity inside the water jumps as follows:

$$u_J \simeq K_0 \frac{\bar{u} + \bar{u}_*}{2}, \tag{3.5}$$

with

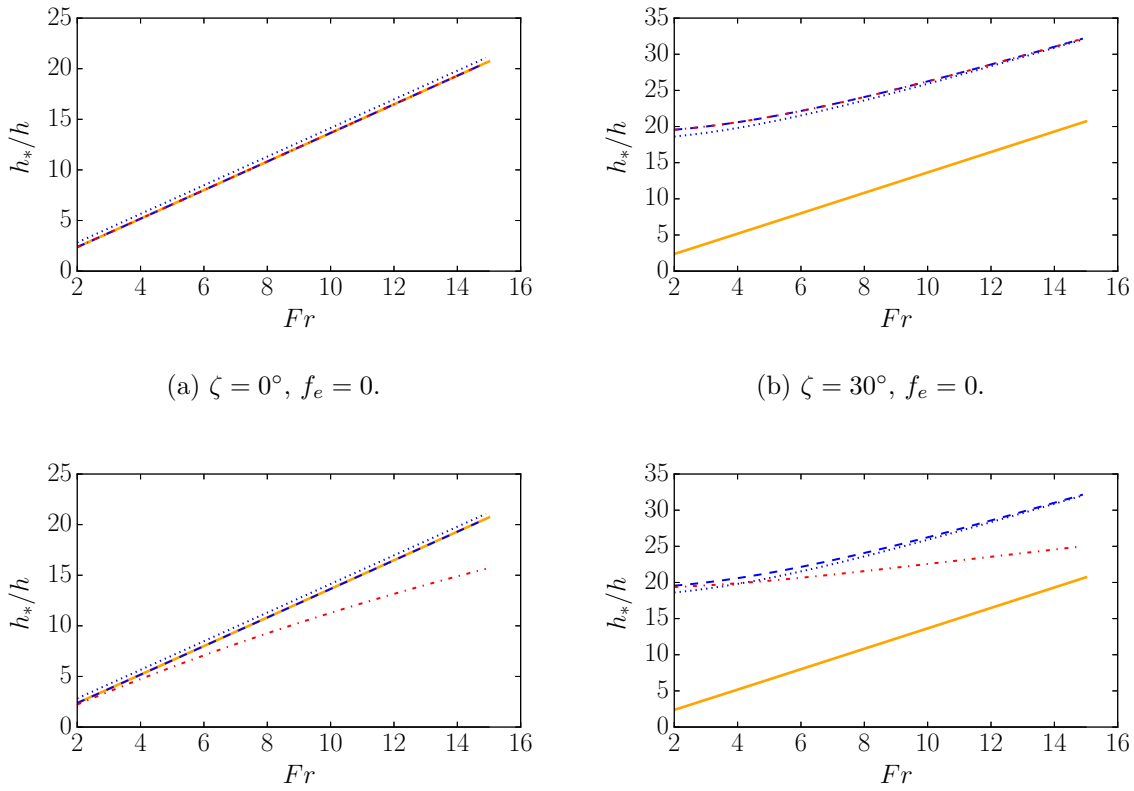

(a) $\zeta = 0°$, $f_e = 0$.

(b) $\zeta = 30°$, $f_e = 0$.

(c) $\zeta = 0°$, $f_e = 0.003$.

(d) $\zeta = 30°$, $f_e = 0.003$.

Figure 3.1: Jump height ratio h_*/h as a function of the Froude number for two slope angles ζ and two bottom friction coefficients f_e, with $L/h = 30$ and $K_0 = 1.05$. The red dashed line corresponds to the water equation initially mistaken but that can be considered as a fit of the experimental data points (Eq. (2.12)), blue dashed line to the correction of this equation (and blue dashplot line for its approximation (Eq. (3.3))), and the orange line corresponds to the prediction of Bélanger equation (Eq. (2.1)).

$$K_0 = \frac{2\int_0^L \rho(x)\mathcal{Z}(x)\,\mathrm{d}x}{L(\rho h + \rho_* h_*)}, \tag{3.6}$$

which led, with the mass conservation equation, to the following equation:

$$u_J = \frac{K_0}{2}\left(1 + \frac{1}{h_*/h}\right)\bar{u}. \tag{3.7}$$

However, from the definition of K_0 itself and the mass conservation, we could have had access to a better candidate to describe the velocity inside the jump. Mass conservation equation gives:

$$(\rho h)_J u_J = cst = \rho h \bar{u}. \tag{3.8}$$

This means that:

$$u_J = \frac{\rho h \bar{u}}{(\rho h)_J}. \tag{3.9}$$

From the definition of K_0 itself (Eq. (3.6)) and the fact that $(\rho h)_J = \frac{1}{L}\int_0^L \rho(x)\mathcal{Z}(x)\,\mathrm{d}x$; we obtain:

$$u_J = \frac{h\bar{u}}{K_0(\frac{h+h_*}{2})}. \tag{3.10}$$

Then, a better candidate for the velocity inside the water jumps is:

$$u_J = \frac{2\bar{u}}{K_0(1+\frac{h_*}{h})}. \tag{3.11}$$

The final equation for the resistive force across the water jumps which can be re-injected in the general equation is:

$$\tau_b = f_e \rho \left(\frac{2\bar{u}}{K_0(1+\frac{h_*}{h})}\right)^2. \tag{3.12}$$

If we inject this new expression in the water jump equation, we obtain the following equation:

$$\begin{aligned}
&\left(\frac{h_*}{h}\right)^5 + \left(\frac{h_*}{h}\right)^4\left[2 - K_0\frac{L}{h}\tan\zeta\right] - \left(\frac{h_*}{h}\right)^3\left[2Fr^2 + 3K_0\frac{L}{h}\tan\zeta\right] \\
&- \left(\frac{h_*}{h}\right)^2\left[2Fr^2 + 2 + 3K_0\frac{L}{h}\tan\zeta\right] \\
&+ \frac{h_*}{h}\left[2Fr^2 - 1 - K_0\frac{L}{h}\tan\zeta + 8f_e\frac{Fr^2}{K_0^2}\frac{L}{h}\right] + 2Fr^2.
\end{aligned} \tag{3.13}$$

Which, with the approximation $h_*/h >> 1$ leads to the following equation:

$$\left(\frac{h_*}{h}\right)^4 - K_0\frac{L}{h}\tan\zeta\left(\frac{h_*}{h}\right)^3 - 2Fr^2\left(\frac{h_*}{h}\right)^2 + 8f_e Fr^2 = 0. \tag{3.14}$$

Figure 3.2 shows the same curves as in Fig. 3.1c, with the addition of the jump height ratio predicted by Eq. (3.14) with the corrected velocity inside the jump u_J (purple cruxes).

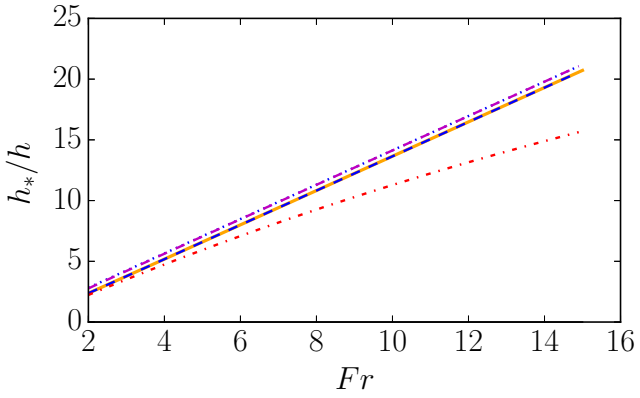

Figure 3.2: Jump height ratio h_*/h as a function of the Froude number Fr predicted by the equation of the fit of the experimental data (red dashed line), the corrected equation (blue dashed line) and its approximation (blue dashplot line), the corrected equation with a more accurate velocity (purple dashed line), and Bélanger equation (orange line). The slope is $\zeta = 0°$, the friction coefficient $f_e = 0.003$, the relative length $L/h = 30$, and the shape factor $K_0 = 1.05$

Using the exact calculation of the mean velocity u_J across the jump, from mass conservation, does not improve the results. The approximation initially done with Eq. (3.5) to estimate the jump velocity is not responsible for the non accuracy of the equation. On the opposite, the term f_e is present in the constant term (independent of h_*/h), thus having nearly no effect on the results.

3.2.2 Other options for resistive forces across water jumps

Modifying the velocity u_J in Eq. (3.4) is not enough to fit the experimental data. The other parameter we can adjust is the friction coefficient f_e. We remind here that this coefficient was extracted from [22], and takes the following form:

$$f_e = \kappa_\tau \kappa_u \left(\frac{r}{R_h} + ab\Re^{-3/4} \right)^{1/3}, \tag{3.15}$$

where κ_τ and κ_u are dimensionless numbers, and a and b are constants (see more details in [22] for typical values for flows in rough pipes), R_h is the hydraulic radius which is equal to $(Wh)/(W + 2h) \approx h$ for the free-surface flows investigated here, r is the typical roughness size, and $\Re = \bar{u}R_h/\nu \approx Fr\sqrt{g}h^{3/2}/\nu$ is the depth-averaged Reynolds number (ν being the fluid viscosity).

In the previous chapter, this friction coefficient, representative of the total jump length, was calculated based on the features of the incoming flow. But if we look closely at Eq. (3.15), The Reynolds numbers $\Re_*$ at the outgoing section of the jumps are always very large (like the Reynolds numbers $\Re$ before the jump), so we can neglect them, and the term r/h_* is also small. We can conclude that changing f_e by taking into account what happens after the jump in section S_* will not change the general form of the equation.

3.2.3 New empirical expression that fit the data

In the corrected equation, with the exact mean velocity across the jump derived from mass conservation, we can apply the approximations $h_*/h \gg 1$ and $K_0 \simeq 1$ to the resistive force across the water jump, and consider f_e as a constant c_1 times the term $(r/h)^{1/3}$:

$$\tau_b = 4 f_e \rho \frac{u^2}{K_0^2} \frac{1}{\left(1 + \frac{h_*}{h}\right)^2} \approx c_1 \left(\frac{r}{h}\right)^{1/3} \rho u^2 \frac{1}{\left(\frac{h_*}{h}\right)^2}. \tag{3.16}$$

If we apply the same approximations to the expression which fitted the experimental data by [13] and [34] , we obtain:

$$\tau_b = c_2 \left(\frac{r}{h}\right)^{1/3} \rho u^2 \left(\frac{h_*}{h}\right). \tag{3.17}$$

Comparing Eqs. (3.16) and (3.17), it is clear that Eq. (3.16) for the resistive force across the water jump will never fit the experimental data. The experimental data by [13] and [34] and the fitting curve expressed with Eq. (3.17) showed that the resistive force across the water jumps should increase with the jump height ratio, which is not the case in Eq. (3.16). Even a resistive force based only on the incoming flow characteristics will not increase with the jump height ratio, and thus is missing what is happening experimentally.

This means that the classical turbulent expression for a resistive force in water flows is not able to express what is happening for water jumps on a rough surface. The physical resistive force should have a term (h_*/h in Eq. (3.17)) that amplifies the effects of the roughness by taking into account the geometry of the jumps. Note that mass conservation equation shows that this term is also equal to $1/(u_*/u)$, the inverse of the velocity reduction.

Another way to clearly see that the resistive force on Eq. (3.16) will never play a role on the jump height ratio is to write the general equation for the resistive force of water jumps on a rough flat base on the implicit form:

$$\frac{h_*}{h} = \sqrt{1 + \frac{8Fr^2}{1 + \frac{2\tau_b L}{\rho g \cos\zeta (h_* - h)^2}}} - 1. \tag{3.18}$$

This shows that in order to affect the jump height ratio, the resistive force across the water jump τ_b should have a term able to balance the $(h_* - h)^2$ in the denominator.

Part II

Two Dimensional numerical simulations

Chapter 4

Discrete Element Method simulations of standing jumps in granular flows down inclines

Ségolène MEJEAN, Thierry FAUG, Itai EINAV
Published in EPJ Web of Conferences (Powder and Grains, 2017)

This chapter shows part of the methodology, and preliminary results using the numerical simulations of standing granular jumps down inclines using the Discrete Element Method. As this article was written at a stage of preliminary results, the reader may wish to skip this chapter and move to the next one for a full description of all the results. Nevertheless, Sec. 4.2.1 is of interest for readers who wish to know the details of the Discrete Element Method, specially the contact laws used and the microscopic parameters.

4.1 Introduction

A standing jump is a rapid change in height and velocity in a free-surface flow, demarcating supercritical from subcritical flows. The phenomenon is well-known for hydraulic jumps on a smooth horizontal bottom, where the jumps obey Bélanger equation: $h_*/h = (\sqrt{1+8Fr^2}-1)/2$, where h and h_* hold respectively for the height before and after the jump, and $Fr = \overline{u}/\sqrt{gh}$ is the Froude number of the flow before the jump, with $\overline{u}$ the depth-averaged velocity and g the acceleration of gravity. However, this equation is not suitable for a granular flow which can occur only down an incline because of the frictional nature of granular materials, and which may be compressible [19]. A recent study [44] confirmed the deviation from Bélanger equation for grains, and even for unfrictional incompressible flows like water when the bottom is rough or inclined. Some applications like the design of avalanche protection dams need an accurate prediction of the geometry of the jumps formed in a flow of dry granular materials whatever the incoming regime [19]. As highlighted in [44], the jump height ratio does not depend on Fr only but is rather a function of a number of parameters:

$$\frac{h_*}{h} = f\left(Fr, \frac{L}{h}, \frac{\rho_*}{\rho}, \tan\zeta - \mu_e, \beta, \beta_*, k, k_*\right), \tag{4.1}$$

where L is the jump length, ζ the incline slope, ρ and ρ_* hold for the density before and after the jump, respectively, and μ_e is the effective friction (see [44]). The coefficients β, β_*, k and k_* will be defined in Sec.4.2.3. In particular, Eq.4.1 suggests that h_*/h can be predicted for any incoming flow and boundary conditions provided L/h is known.

Our study aims to reproduce numerically a standing jump formed in a flow of granular materials thanks to the Discrete Element Method (DEM), in order to measure precisely the macroscopic parameters needed for Eq.4.1, and to decipher the internal structure of the jump. In granular media, the jump is defined as the part of the flow between the

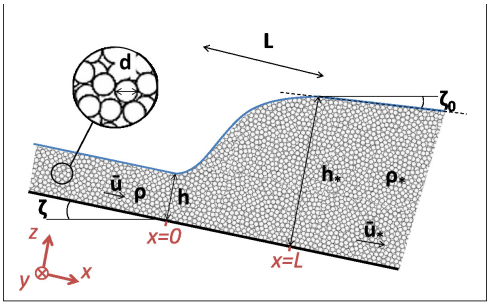

Figure 4.1: Sketch of a granular jump and notations

incoming flow, where the free-surface is parallel to the incline, and the outgoing flow, where the slope of the free-surface is constant and equal to the critical slope ζ_0 below which no flow can occur, as proposed in [19]. For the largest ζ, the flow is slightly accelerating (non-uniform, but still at steady state). In those cases, the slope angle of the free-surface is however very small compared to the changes in the jump, and is not considered here (like in [19]). The main variables defining a jump are summarized in Fig.4.1. The depth-averaged velocity after the jump is noted $\bar{u}_*$, and the mean diameter of the grains is d.

Section 4.2 describes the DEM contact-laws, the numerical set-up used to create a jump, and the techniques to measure all the variables of interest. Section 4.3 shows that this method allows to create a wide variety of jumps, and presents some of the first results. Finally, a short conclusion is given on the main challenging issues this granular jump numerical set-up will allow to investigate.

4.2 DEM simulations of standing jumps

This section describes how granular flows are simulated thanks to DEM, using YADE open-source software [74].

4.2.1 Microscopic contact laws

In order to model the grains interacting each other, we chose the classical following viscoelastic law:

$$\begin{cases} \mathbf{F_n} = k_n \delta_n \mathbf{n} + c_n \dot{\delta_n} \mathbf{n} \\ \mathbf{\Delta F_s} = k_s \dot{\delta_s} \mathrm{dt}\ \mathbf{s} \\ F_s \leq \mu F_n \end{cases} \tag{4.2}$$

In this equation, $\mathbf{F_n}$ and $\mathbf{F_s}$ are the normal and tangential forces. $\mathbf{F_n}$ is the sum of a linear spring (of stiffness k_n, and proportional to the normal overlap δ_n) and a dashpot of damping coefficient c_n that depends on the restitution coefficient e. $\mathbf{F_s}$ is incremented at each time step dt as a linear spring (of stiffness k_s proportional to the derivative of the tangential overlap $\dot{\delta_s}$) restricted to a Coulomb threshold force defined by the friction coefficients μ and μ_b for grain-grain and grain-wall interactions, respectively. In this study, the tests are carried out in two dimensions (2D), with only one particle across the width. This is made by blocking one degree of freedom in translation and two degrees of freedom in rotation for each particle. k_n and k_s are calculated from the values of Young's modulus E—which was taken equal to 1×10^6 to respect the limit of rigid grains condition, and Poisson coefficient ν taken equal to 0.3: $k_n = Ed/2$ and $k_s = \nu k_n$, considering one

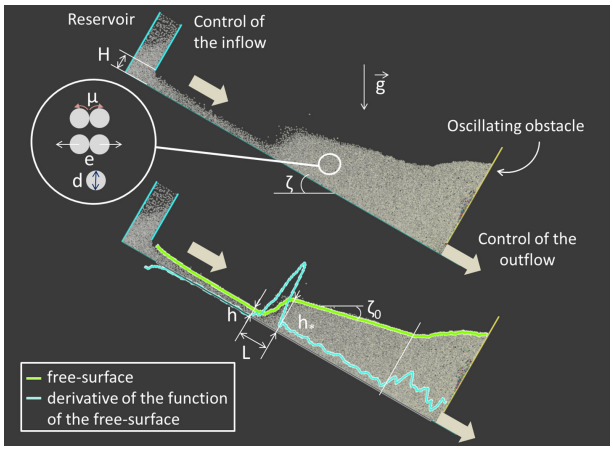

Figure 4.2: DEM numerical set-up to produce standing granular jumps. ($\zeta = 30°, H = 0.5, d = 2cm, \mu = 0.5, e = 0.5$)

Table 4.1: Default values (first line) and ranges (second line) of the varying parameters for the 53 preliminary tests.

ζ [°]	H [m]	d [cm]	μ [$-$]	e [$-$]
20	0.35	4	0.5	0.5
$[15-40]$	$[0.35-1.1]$	$[1-6]$	$[0.05-1]$	$[0.2-1]$

diameter d for all particles. A polydispersity of 15% around the chosen diameter $d = 4$ cm is considered to avoid crystallization effects. The bed-friction coefficient was $\mu_b = 0.25$. The grain density $\rho_P = 2500$ kg m^3 to mimic the density of glass beads usually used in laboratory models. The time-step was $dt = 3 \times 10^{-4}$s.

4.2.2 DEM set-up to produce the jumps

The numerical set-up is shown in Fig.4.2. A reservoir permanently filled up with grains feeds an incline. At the exit, a gate initially retains the grains. When there are enough grains in the incline, the gate moves up. Every 150 time steps, the outflow discharge is calculated and compared with the inflow. The gate then slightly moves, up or down to adjust the discharge and guarantee a steady state. This is a slight difference from the laboratory model where the gate was adjusted by the operator and fixed [19]. The strong advantage of DEM is that many control variables can be changed to see their effect on the jump: the slope angle ζ, the height H of the reservoir exit (that controls the inflow), but also the grain diameter, the interparticle friction and the restitution coefficient. All parameters have a default value, and each parameter was varied—the other ones being fixed at the default value (see Tab.4.1).

4.2.3 Measurement techniques

Geometry of the jump

When a simulation runs, the first step is to reach a steady state. Then, the free-surface is calculated by discretising the incline, and identifying the highest grain in each cell. This is made a hundred times at several time steps to obtain a smooth time-averaged free-surface at continuum scale. The latter allows to identify the beginning of the jump, which is the location where the free-surface is not parallel to the bottom anymore—when

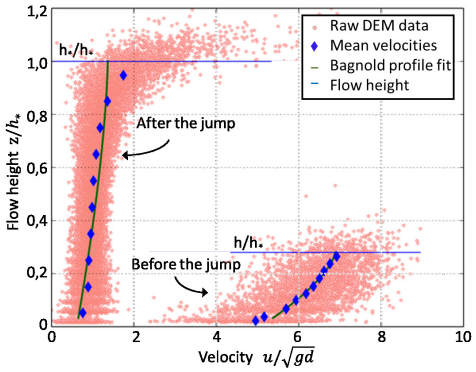

Figure 4.3: Velocity profiles across flow-depth before and after the jump for one test: $\zeta = 20°$, $H = 0.5$m, $d = 4$cm, $\mu = 0.5$, $e = 0.5$. Blue diamonds are velocities averaged over height increments; green lines are fits with Eq.4.3

the derivative of the function describing it becomes non-zero (Fig.4.2). We also identify the end of the jump, where the slope of the free-surface becomes constant—meaning that the derivative is constant. Once a steady state is reached and both the beginning and the end of the jump are well identified, a new simulation is done to record the variables of interest.

Velocity profiles

An example of velocity profiles recorded before and after the jump is shown in Fig.4.3. The raw DEM data sets exhibit a noticeable scattering caused by the (discrete) fluctuating nature of the flowing grains, but the mean velocities are well-described at continuum scale and they can be fitted by a Bagnold profile with basal slip, as already suggested in [9, 19], which is given by the following equation:

$$u(z) = u_b + A\sqrt{gh}\left[\left(\frac{h - z_0}{d}\right)^{3/2} - \left(\frac{h - z}{d}\right)^{3/2}\right] \tag{4.3}$$

where u_b denotes the sliding velocity of the basal layer, which is taken at $z = z_0 = 1.5d$ (following [9, 19]) and A is the Bagnold pre-factor, which was let free in the fits of Fig.4.3. The hypothesis of the Bagnold profile seems very appropriate for the velocity of the incoming flow. But Fig.4.3 shows that it is less satisfying for the outgoing flow, because of a change in concavity next to the free-surface that will need further investigation in the future.

Measuring accurately the velocities thanks to DEM makes it possible to calculate precisely the Boussinesq coefficient, β before the jump (or β_* after the jump), which is defined by the relation $\beta = \bar{u^2}/\bar{u}^2$. The variations of β and β_* with Fr and Fr_* respectively are given in Fig.4.4(a). It clearly shows that the usual assumption that $\beta = 1$ is very accurate for median values of the Froude number that we find most of the time in the incoming flows, while it may become an underestimate for very low values of the Froude number as found in the downstream flow.

Earth pressure coefficients k,k_*

The earth pressure coefficients, noted k and k_* before and after the jump respectively, relate the normal stresses through the relation $\sigma_{xx} = k\sigma_{zz}$. In this study, k and k_* were

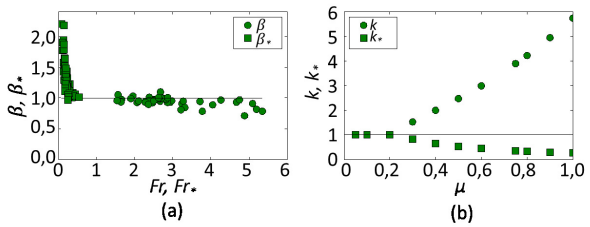

Figure 4.4: (a) Boussinesq coefficients β or β_* versus the Froude number Fr or Fr_*. (b) Earth pressure coefficients calculated from Eq.4.4 versus the grain-grain friction μ.

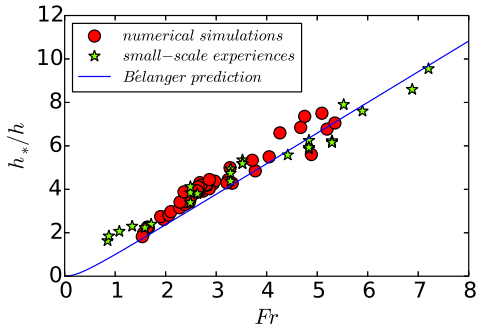

Figure 4.5: h_*/h versus Fr obtained with the present numerical experiments (red circles) compared to the laboratory experiments conducted by [19] (green stars).

not directly measured but derived from soil mechanics concepts, as proposed by Savage and Hutter [60]:

$$k_{pass/act} = \frac{2\left(1 \pm \sqrt{1 - (1 + \tan^2 \varphi_s)\cos^2 \varphi_e}\right)}{\cos^2 \varphi_e} - 1, \tag{4.4}$$

where $\varphi_s = \tan^{-1}(\mu_b)$ is the bed friction angle and $\varphi_e = \tan^{-1}(\mu)$ the internal friction angle. When μ becomes lower than μ_b, we can consider $k = k_* = 1$. The variations of k and k_* with μ according to Eq.4.4 are plotted in Fig.4.4(b). Because the inter-particle friction coefficient used in DEM is known to be different from the macroscopic (internal) friction coefficient ([67]), our assumption for Equation 4 remains questionable. Future work will consider shear-dependent friction coefficients, such as developed by [40].

4.3 A rich variety of granular jumps

The method presented in Sec.4.2.2 allows to create a wide range of jumps, and confirms the results obtained in the laboratory [19] as shown in Fig.4.5. We could observe steep or diffuse jumps, compressible or incompressible jumps, and identify the presence or absence of a recirculation zone. Figure 4.6 displays pictures of jumps—with the internal streamlines drawn, obtained for different ζ and H/d.

4.3.1 Jump steepness

The two characteristic length-scales of a jump are its height ratio h_*/h and its relative length L/h (if not neglected like in Bélanger equation). Combining the two leads to the steepness coefficient $\mathcal{S} = (h_* - h)/L$ with respect to the slope of the bottom. $\mathcal{S}$ can

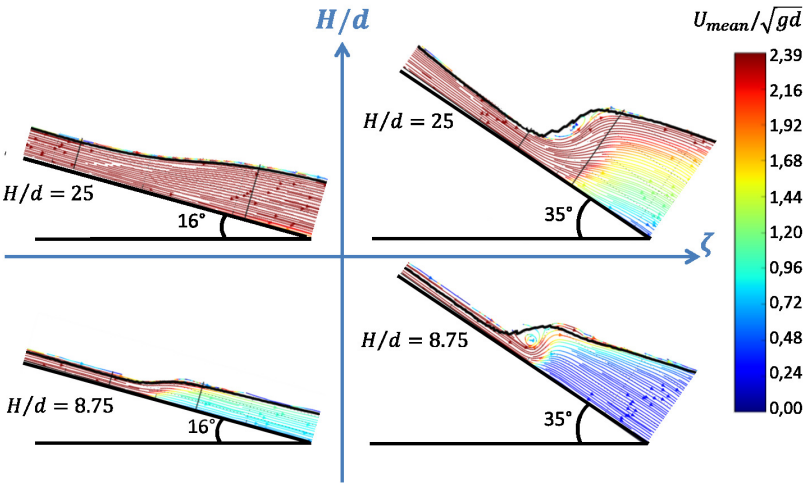

Figure 4.6: $(H/d,\ \zeta)$ phase diagram for granular jumps. In each picture of the jumps, the streamlines are drawn, thus allowing us to identify the presence or absence of a recirculation zone

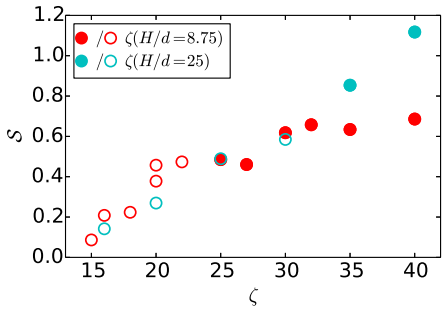

Figure 4.7: Steepness $\mathcal{S}$ versus the slope ζ for two values of H/d ($d = 4$ cm). Empty—full—circles represent the jumps without—with—a recirculation zone.

grow by increasing ζ, and weakly depends on H/d (Fig.4.7). It is also correlated with the presence of recirculation as a very steep jump will be instable, thus promoting the recirculation. A larger opening of the reservoir leads to a higher discharge and a denser jump, more stable. As such, the recirculation appears for higher ζ and $\mathcal{S}$. It is worthwhile to note that jumps with recirculation were also observed for very low μ, typically smaller than μ_b. This result–likely to unravel the key role played by friction in the birth of jump recirculation, will need further investigation in the future.

4.3.2 Jump compressibility

The granular jump compressibility is defined as the ratio ϕ_*/ϕ (where $\rho = \rho_P\phi$) between the volume fractions before and after the jump. ϕ_* was systematically found to be close to 0.81 (whatever the incoming flow and boundary conditions), which is nearly equal to the 2D granular random close packing. Then, once the incoming flow is dilute ($\phi < \phi_*$), a compressible jump is obtained. Our simulations showed that it is possible to tend toward an incompressible jump ($\phi_*/\phi \mapsto 1$) by different ways: increasing H/d, decreasing ζ, decreasing d or decreasing μ.

4.4 Conclusion

The current paper presented preliminary DEM simulations of standing jumps formed in flows of granular materials down an incline. The first results are consistent with the recent findings in laboratory tests [19]. This novel numerical set-up now offers the possibility to study in detail how the jump geometry and its internal structure are influenced by a number of parameters, and will allow to investigate the energy dissipation inside the jump, as proposed in [44].

Chapter 5

Length of standing jumps along granular flows down inclines

Ségolène MEJEAN, François Guillard, Thierry FAUG, Itai EINAV
Submitted to Physical Review Fluids

This chapter summarizes most of the results obtained with the numerical simulations of granular jumps down inclines using Discrete Element Method. It is the next logical step from the conclusions in Part I, justifying why we should focus on the length of the jump to obtain closure relations for the general relation. The introduction (Sec. 5.1) was already treated in Chap. 1 and Part I. Section 5.2 presents the methodology for accessing important variables from the numerical simulations. Section 5.3 presents the wide range of observable granular jumps in the simulations, and separates them into three different types of jumps. Section 5.4 focuses on the length of the jumps and its evolution with some control parameters. Finally, the conclusion (Sec. 5.5) collates the data together to compare them and highlight why the type of the jump should be taken into account.

Abstract: Granular jumps—the change in height and depth-averaged velocity during granular flows—occur during transitions from thin and fast flows (supercritical) to thick and slow flows (subcritical). The present paper describes discrete element method simulations inspired by recent laboratory experiments, which produce standing jumps in two-dimensional free-surface dry granular flows down a slope. Special attention is paid to characterizing and measuring the finite length of those standing granular jumps, as well as to deciphering their internal structure. By varying macroscopic quantities, such as slope angle and mass discharge, and microscopic properties, such as interparticle friction and grain diameter, a rich variety of granular jump patterns is observed. Hydraulic-like granular jumps with an internal water-like roller are identified, in addition to diffuse laminar granular jumps and steep colliding granular jumps. Moreover, the analysis of the results using a recently proposed depth-averaged relation for the prediction of jump heights strongly suggests that the dissipation mechanisms at stake are remarkably different when transitioning from one jump pattern to another.

5.1 Introduction

Granular materials are ubiquitous in nature and are often involved in a myriad of industrial processes. When an assembly of grains experiences different boundary conditions, it can move across different states of matter, from solid through to liquid and gaseous phases [36, 20]. Those transitions are for instance observed in free-surface flows of dry granular materials down a slope [21], which are relevant to a number of large-scale mass flows in nature, such as landslides, debris flows and snow avalanches. When the front of a granular flow hits a solid surface, either horizontal [7] or inclined [38], its profile presents a sudden change in height and velocity. As granular flows impact barriers—which are commonly

used for stopping or diverting landslides, debris flows and avalanches—they experience such a sudden change in height and velocity, as reported by [18, 68] and references therein. The profile change in height and velocity is called a *granular jump*. Granular jumps can be gradual or very sharp, and accompanied by a change in density when the incoming flow is dilute enough (far below the random close packing density of a quasi-static assembly of grains). Granular jumps along free-surface flows are often described by classical shallow-water shock equations, which are based on the simplification that the jump volume shrinks into a singular surface. However, granular jumps do have a finite volume (and length), as clearly demonstrated from the laboratory study on standing jumps recently conducted by [19].

The overarching aim of the present study is to carefully analyse the properties that control the length of standing granular jumps, using the numerical discrete element method. The length of the standing granular jumps represents the efficiency of the material to dissipate energy as it transitions from a thin and fast flow to a thicker and slower flow. Therefore studying the length and internal structure of standing granular jumps can help in deciphering the various mechanisms at the origin of energy dissipation, and thus advance the knowledge of the physics of dense granular flows. A recent study [44] proposed a general relation for the height ratio of a standing granular jump, h_*/h, as a function (noted $\mathcal{F}$ in Eq.(5.1) below) of the incoming Froude number of the flow $Fr = \bar{u}/(gh\cos\zeta)^{1/2}$, the normalized length of the jump, L/h, and the difference between the tangent of the slope angle ($\tan\zeta$) and the effective friction μ_e under a generalized Coulomb friction assumption (within the depth-averaged framework):

$$\frac{h_*}{h} = \mathcal{F}\left(Fr, \frac{L}{h}, \tan\zeta - \mu_e, \frac{\rho_*}{\rho}...\right), \tag{5.1}$$

where h is the thickness of the fast and thin incoming flow, $\bar{u}$ is the depth-averaged velocity, h_* is the jump height (outgoing section of the jump), L the length of the jump and g the gravity acceleration ($g = 9.81$ m.s^{-2}). $\rho = \phi\rho_P$ and $\rho_* = \phi_*\rho_P$ are the density of the granular bulk before and after the jump, respectively, where ϕ is the volume fraction and ρ_P is the grain material density. For more details on this equation and related input parameters readers are referred to [44].

A recent experimental work [19] showed that considering a constitutive law based on the $\mu(I)-$rheology (proposed by [40]) through the effective friction μ_e defined above could give a good prediction of the jump height ratio h_*/h, provided that the incoming flows were steady and uniform. However, it is necessary to include an additional dissipative term, which depends on the velocity-squared of the incoming flows, when the flows are fast and accelerating [44]. Moreover, no theoretical framework currently exists to predict the length of the jumps, thus rendering Eq.(5.1) not fully predictive. The present paper provides a detailed study of the internal structure of standing granular jumps and their length with the help of discrete element simulations in two dimensions. Several characterization methods based on the free-surface of the jump, the velocity field, and the density field across the jump are proposed and compared. The influence of both macroscopic (mass discharge, slope angle) and microscopic (interparticle friction, grain diameter, restitution coefficient) input parameters on the length of the jumps are analysed. The internal flow of the granular jumps allows us to clearly identify three different types of jumps, thus providing crucial information on the jump length variation.

Section 5.2 presents the numerical set-up of the discrete element simulations used to produce the two-dimensional standing jumps, largely inspired by a laboratory device designed by [19]. Section 5.3 discusses the rich variety of granular jumps observed in

the numerical simulations, confirming and further extending some of the results obtained with the previous laboratory tests [19]. In particular, a new type of granular jump is identified. Some more quantitative aspects associated with each type of granular jump are addressed in Sec. 5.3. The variation of the jump length with both macroscopic and microscopic input parameters is analysed in detail in Sec. 5.4 for the different types of jump. Finally, the paper ends with a discussion on the main outcomes of the present study and recommendation for future work (Sec. 5.5).

5.2 Methods

5.2.1 Numerical set-up to produce standing jumps

Simulations using the Discrete Element Method (DEM) are carried out with the YADE open source software [66], with spherical grains whose interaction is modelled by a visco-elastic force for normal contact directions and an elastic force capped by a Coulomb friction threshold for tangential contact directions. The details of this classical contact model used in DEM for dense granular flows are described in [46]. The simulations are carried out in two dimensions, meaning that there is only one grain across the width of the flume and that side-walls effects are ignored, in contrast to the laboratory tests on granular jumps conducted by [19]. The grain diameter distribution varies 15% around the average diameter. This corresponds to a polydispersity which is high enough to avoid crystallization effects yet low enough to prevent grain segregation processes.

The numerical set-up used to produce the jumps is shown in Fig. 5.1, which describes an inclined plane of slope ζ that sustains a granular flow supplied by an upstream reservoir with an opening height H that is permanently feeding in grains. An initially closed retaining gate is placed at the exit of the incline. Under these conditions, a propagating granular jump is formed once the grains impact the retaining gate at the bottom of the plane. When the travelling jump reaches the middle of the incline, the retaining gate is moved vertically in order to make the jumps stationary. To this purpose, the incoming and outgoing discharge rates are continuously measured, while the retaining gate is constantly adjusted vertically to balance the two flow rates. When the steady flow state is reached, the gate still has the possibility to move up or down if the outgoing discharge becomes different from the incoming discharge, in order to maintain a steady flow during all the simulation. A number of numerical simulations are performed by varying the slope of the incline ζ and the opening height of the reservoir H (which controls the mass discharge). The effects of microscopic grain properties are also examined by varying the grain diameter d, the interparticle friction μ, and the restitution coefficient e.

5.2.2 From micro to macro: coarse-graining

The spatial fields of volume fraction, velocity, and energy flux are calculated on a grid with a space-step of half a grain diameter d, using a coarse-graining method similar to the one described in [23, 25, 70]. The flowing particles are labelled from 1 to N. From statistical mechanics, the density of the granular medium at a given position $\mathbf{r}$ and time t is defined by:

$$\rho(\mathbf{r},t) = \sum_{\|\mathbf{r}-\mathbf{r_i}(t)\|\leq c} (m_i \mathcal{W}(\|\mathbf{r}-\mathbf{r_i}(t)\|)\,, \tag{5.2}$$

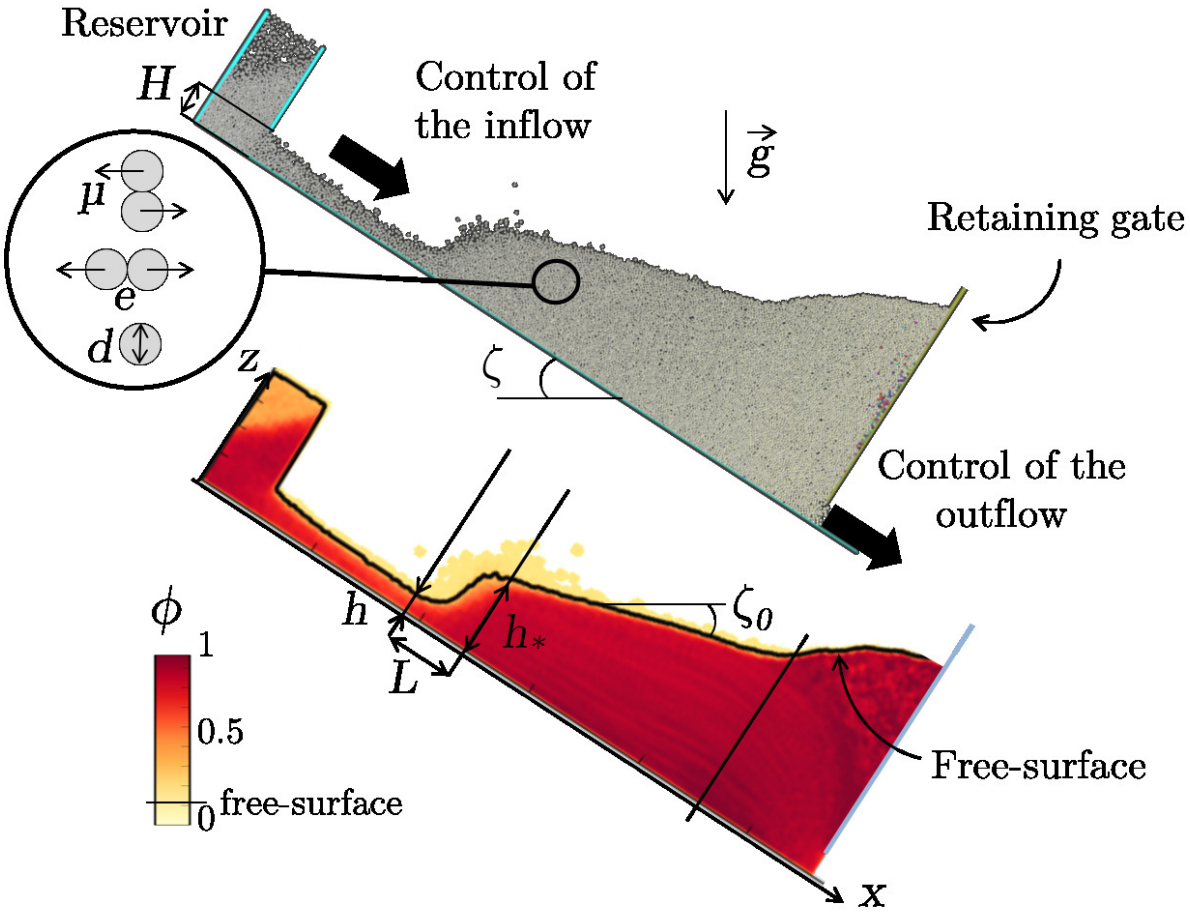

Figure 5.1: Discrete element method numerical set-up (top) and example of a volume fraction field obtained by coarse-graining (bottom).

with $\|\mathbf{r}-\mathbf{r_i}\|$ the distance between the centre of the i^{th} grain with mass m_i to the point $\mathbf{r}$ on the grid. A Lucy function $\mathcal{W}$ was used for the coarse-graining [43], which for two spatial dimensions takes the form [56]:

$$\mathcal{W}(\mathbf{r}) = \frac{5}{\pi c^2}\left[-3\left(\frac{r}{c}\right)^4 + 8\left(\frac{r}{c}\right)^3 - 6\left(\frac{r}{c}\right)^2 + 1\right], \tag{5.3}$$

with c the range of the Lucy function, here taken equal to $2.5d$, which is large enough to smoothen out the discrete nature of the granular system while observing the continuum gradients.

Any other coarse-grained value $f(\mathbf{r},t)$ (e.g., f may represent any variable such as the velocity or the energy) could be calculated from:

$$f(\mathbf{r},t) = \frac{\sum_{\|\mathbf{r}-\mathbf{r_i}(t)\|\leq c}\left(f(\mathbf{r_i},t)m_i\mathcal{W}(\|\mathbf{r}-\mathbf{r_i}(t)\|\right)}{\rho(\mathbf{r},t)}. \tag{5.4}$$

For a steady flow state, the coarse-grained fields can be averaged in time, over a sufficient number of time steps such that the results is insensitive to increasing number of frames. The free-surface is defined from the field of volume fraction ϕ, with a threshold of 0.15, which largely indicates a transition from a loose gaseous-like to a denser fluid-like medium. A typical result obtained for the volume fraction field is shown on Fig. 5.1. Furthermore, the depth-averaged variables will also be described in the following along the $x-$axis of the inclined plane, by averaging the values of the points of the grid that are under the free-surface for each x, and weighting them by the density at that point:

$$f(x) = \frac{\sum_{z\leq h(x)}\rho(x,z)f(x,z)}{\sum_{z\leq h(x)}\rho(x,z)}. \tag{5.5}$$

Some examples of the velocity profiles at different given positions along the chute extracted from the two-dimensional velocity field will be shown in Sec. 5.3.

5.2.3 Defining the length(s) of the jump

The aim of the DEM simulations presented in the current paper is to define and determine accurately the length of standing granular jumps, as a closure relationship for Eq.(5.1). Until now, the jump length has always been defined only visually through observation of the free-surface [19, 44, 46]. This definition is tacitly based on the assumption that the jump begins when the free-surface is no longer parallel to the bottom, and ends when it reaches a constant angle which corresponds to the minimum angle to have a flow. As can be seen in Fig. 5.2, a jump is characterized by a rapid change not only in the flow thickness h, but also in the depth-averaged velocity $\bar{u}$ and in the volume fraction ϕ. By considering h, $\bar{u}$ or ϕ, it is possible to define at least three different lengths for the jump.

The volume fraction was already used above as a criterion for determining the free-surface of the flowing medium, i.e. to distinguish between the dense flowing layer and the gaseous phase of particles undergoing zero to binary collisions above the free-surface (viz., using the threshold of 0.15 in volume fraction on Fig. 5.1). However, Fig. 5.2 shows that the depth-averaged variation of the volume fraction along the x coordinate is not very smooth, so a criterion for defining the jump length based on volume fraction is probably not going to be reliable. That said, the length of the jump defined by the volume fraction appears to be very close to the length of the jump defined by the velocity.

Both the free-surface curve used in the previous studies [19, 46] and the depth-averaged velocity curve proposed in the present study exhibit a smooth signal. Their corresponding

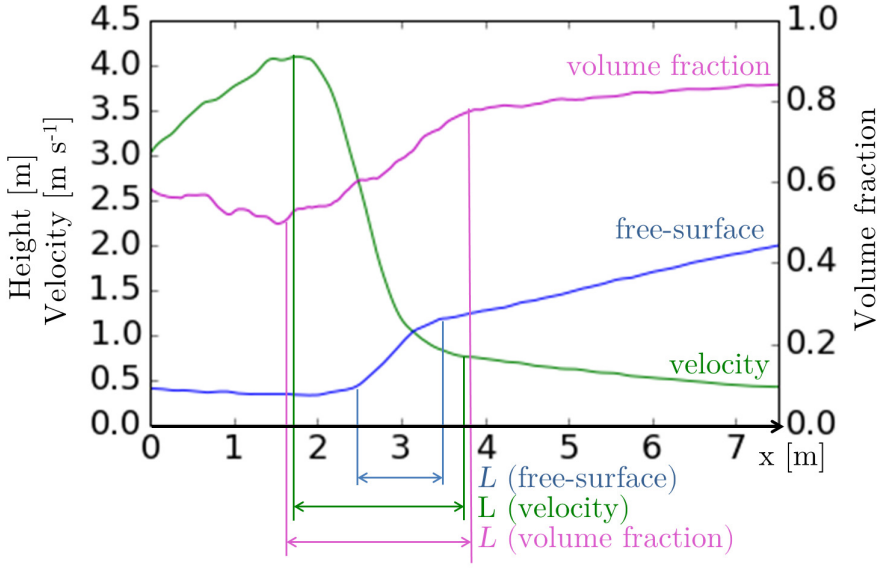

Figure 5.2: Three different jump lengths identified for a single standing (laminar) granular jump, based on the depth-averaged variable considered: h (blue line), $\bar{u}$ (green line) or ϕ (pink line). This jump was obtained with $\zeta = 28°$, $H = 0.5$ m, $\mu = 0.5$, $d = 4.0$ cm.

curves also show the transition between the fast and thin flow regime (supercritical) and the slow and thick flow regime (subcritical). The start of the jump is relatively easy to determine. In the case of the velocity curve, this point is well defined in terms of the local maximum of the curve. In the case of the free-surface curve, that point is well defined too, as already discussed previously. The end of the jump is not as straightforward to determine, regardless of the criterion used (either the free-surface or the depth-averaged velocity curves). However, in both cases, one can find the point where the curve describing the corresponding variable (h or $\bar{u}$) along the plane becomes a straight line. This method requires a smoothing of the function that describes the variable considered. The smoothing function used was a Savitzky-Golay filter [62], as it gave sufficiently smooth results without loosing the information of the points where there are strong variations. Then, the transition point is defined when the derivative of the function describing the variable becomes constant. As the two methods give different results, the question is then which of these two length definitions is the more relevant?

The length of the jump region can be considered as the length of a transition zone between two different possible stable flow states. That length should be a function of the given set of initial conditions (slope angle, discharge rate, frictional properties of the side and bottom walls, and the properties of the grains): any disturbance from a stable state observed along the inclined plane should be considered as being a part of the jump region itself. Figure 5.2 shows that a disturbance already occurs on the depth-averaged velocity curve and the depth-averaged volume fraction curve while the changes are not yet detected on the free-surface curve. Moreover, the end of the jump given by the velocity curve (similar to the one given by the volume fraction curve) stands beyond the end of the jump given by the free-surface curve (Fig. 5.2), suggesting that disturbances also occur after the end of the jump detected from the free-surface curve. For these reasons it seems reasonable to choose the depth-averaged velocity as the criterion to determine the jump region. In the rest of this study, the length L will always refer to the length of the jump

-	H [m]	ζ [°]	d [m]	μ	μ_b	e
default value	0.5	20	0.04	0.5	0.25	0.5
range	$0.4 - 1.1$	$22 - 50$	$0.02 - 0.06$	$0.04 - 1.0$	-	$0.1 - 1.0$

Table 5.1: The default and range of values for the parameters of the jumps: height of the opening of the reservoir H, slope of the flume ζ, average grain diameter d, interparticle friction coefficient μ, friction coefficient between the grains and the bottom of the inclined plane μ_b, and the restitution coefficient between grains e.

measured from the velocity profile, as described above.

5.3 The different types of jump

The numerical set-up allows to obtain a wide spectrum of standing granular jump patterns by varying the control parameters over the ranges listed in Table 7.1. The restitution coefficient e between the grains did not have any discernible influence on the jumps created. For that reason, all the jumps reported in the present work are based on a restitution coefficient $e = 0.5$.

Figure 5.3a shows some examples of the streamlines inside the jumps obtained by coarse graining the velocities from the DEM. A transition from steep jumps at high slope angles to much more diffuse jumps at the lower slope angles is observed. Under high mass discharges, the granular media tend to remain dense and nearly incompressible. In contrast, the jumps become much more compressible at lower mass discharges. A recirculation zone can be identified under some specific conditions when, either the slope angle and/or the mass discharge are high. Those different 2D numerical jump patterns are fully consistent with previous 3D experimental results. Additionally, Fig. 5.3b shows the experimental phase diagram obtained in [19], which compares qualitatively well with the phase diagram obtained numerically (Fig. 5.3a) in the present study, by varying both ζ and H.

The advantage of the current numerical simulations is that the streamlines can be accessed before, inside and after the jumps. Recirculation zones can for instance be clearly identified in the top right corner of the numerical phase diagram in Fig. 5.3a, with one of the streamlines showing a rolling pattern that is developing at the foot of the steep jump. A criterion to identify the recirculation more easily than with the streamlines, and even estimate its size, will be discussed in Sec. 5.3.

Recirculation patterns are also observed once the interparticle friction μ is decreased to values smaller than a critical friction μ_{cr}, as depicted on Fig. 5.4. The recirculation here always takes place into the interior of the jump and can run along almost the entire length of the jump. This type of recirculation is different from the one observed in the phase diagram (Fig. 5.3a), which is located close to the free-surface at the foot of the jump. Note that the recirculation observed in the phase diagram at high slope angles is either just below the free-surface (high discharge rates) or above (lower discharge rates). The recirculation pattern observed under small values of interparticle friction is rather closer to the fully-developed internal roller that one observes with hydraulic (non-frictional) flows. That water-like granular roller was not observed in the experimental work in [19] as the interparticle friction coefficient is inherent to the material and thus cannot be easily controlled experimentally. In the following, we will discuss in more detail the properties of the different types of jump patterns.

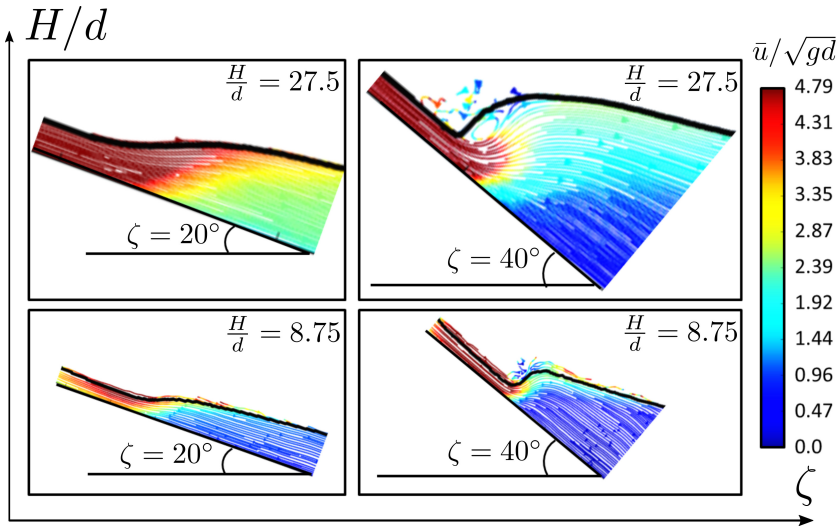

(a) Numerical phase diagram with streamlines

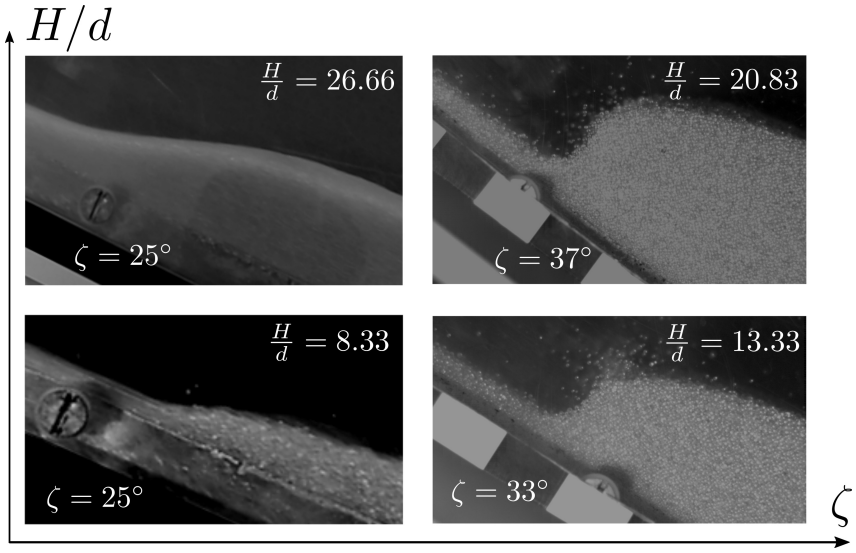

(b) Experimental phase diagram (pictures)

Figure 5.3: Numerical and experimental phase diagrams of jump patterns, for various slopes ζ and discharge height ratio H/d. (a)hase diagram obtained numerically in the present study. The streamlines inside the jumps are drawn with a colour indicating the local velocity. All the simulation use an interparticle friction $\mu = 0.5$ and a bottom friction $\mu_b = 0.25$. (b)hase diagram obtained experimentally by [19] using glass beads.

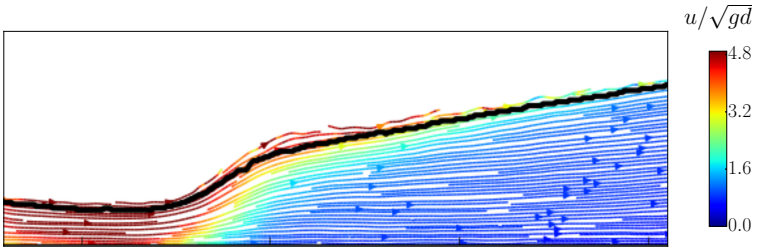

(a)

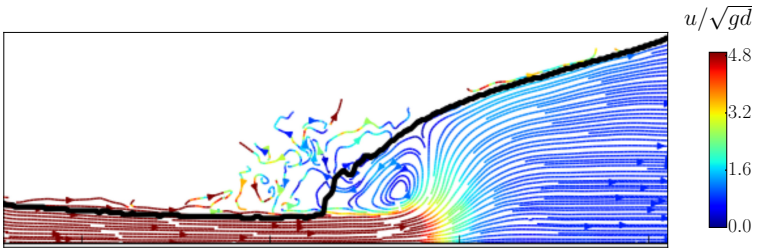

(b)

Figure 5.4: Transition from (a) laminar granular jump ($\mu = 0.8 > \mu_{cr}$) to (b) hydraulic-like granular jump with the presence of a water-like roller ($\mu = 0.1 < \mu_{cr}$). The streamlines are drawn in each jump as in Fig. 5.3a with colours representing the corresponding velocity.

5.3.1 Laminar granular jumps

Figure 5.2 shows the height of the free-surface, the depth-averaged velocity, and the depth-averaged volume fraction of a laminar granular jump. The streamlines of this type of jump (see the two pictures on the left side of Fig. 5.3a) are showing a smooth transition from one stable state (thin flow, high velocity) to another (thick flow, low velocity).

In this kind of jumps, the energy is deemed to dissipate due to the friction developing between the grains. The depth-averaged volume fraction in such jumps (see purple curve in Fig. 5.2) exhibits a monotonic growth while transitioning from one state to the other. We will show in Sec. 5.4 that, for such laminar granular jumps, the length L of the jump could be expressed as a linear function of the incoming thickness h.

Figure 5.5 shows the velocity profiles of a laminar jump. As discussed in previous studies about granular flows down smooth inclines [9, 19], the incoming velocity profile (red curves in Fig. 5.5) follows a Bagnold profile with a sliding velocity at the bottom. The velocity as a function of depth $u(z)$ is given by:

$$u(z) = u_b(\zeta) + A(\zeta)\sqrt{gd}\left[\left(\frac{h - z_0}{d}\right)^{3/2} - \left(\frac{h - z_0}{d} - \frac{z - z_0}{d}\right)^{3/2}\right], \tag{5.6}$$

with $u_b(\zeta)$ the sliding velocity and $A(\zeta)$ a coefficient, both dependent on the slope angle ζ, and $z_0 = 1.5d$ the typical thickness of the layer made of grains sliding on the chute bottom (roughly assumed to be independent on ζ). Empirical expressions for $u_b(\zeta)$ and $A(\zeta)$ are discussed in [19].

After the end of the jump (blue curves in Fig. 5.5), the velocity profile is totally different: the sliding velocity is much lower and the shear rates are much weaker. Inside the jump region (green curves in Fig. 5.5), the velocity profiles adjust from the upstream stable flow state to the downstream gradually decelerating flow state. The curves showing

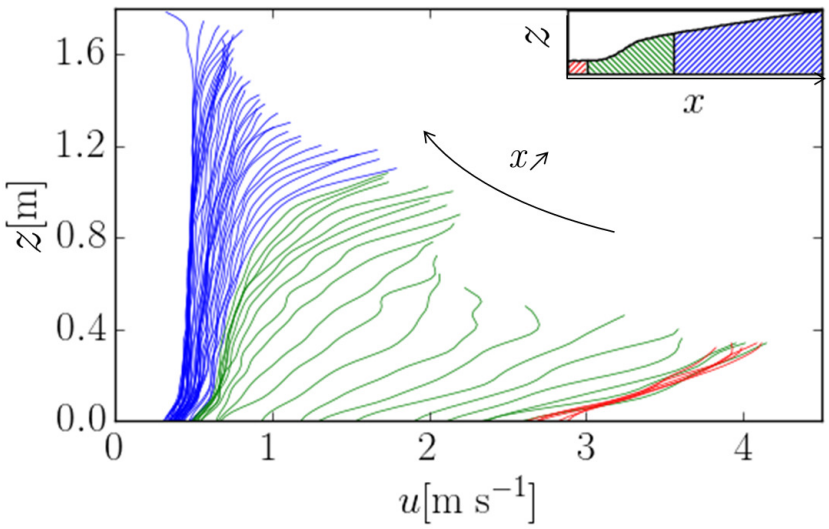

Figure 5.5: Velocity profiles of a laminar granular jump ($\zeta = 24°$, $d = 4$cm, $H = 0.5$m, $\mu = 0.5$) before (red), inside (green) and after (blue) the jump. The velocity profiles shown were measured every 0.12 m along the inclined plane.

those profiles are well separated because of a significant decrease of velocity along the $x-$axis within the jump region, while they collapse well before the jump (non-accelerating flow) and are quite close to each other after the jump (slightly decelerating flow).

5.3.2 Steep colliding granular jumps

Starting from the conditions under which a laminar granular jump is formed, increased slope angle as in Fig. 5.6 gradually destabilizes the jump, with the possibility of an accompanying recirculation pattern. The jump region in that case is very short and steep, while the gravity forces are having a strong influence on the flow. In particular, the grains of the incoming collisional flow add a strong eroding force on the grains inside the jump, whereas the grains on top of the jump are pulled down by gravity in an avalanching process.

This recirculation can be seen in the streamlines (see the pictures depicted on the first row of Fig. 5.6 for cases c, d and e). This phenomenon becomes even more obvious when plotting the variations of the depth-averaged volume fraction $\phi(x)$ along the chute as displayed on Fig. 5.6 (second row). Here, a significant drop in volume fraction takes place from the middle to the end of the jump for cases c, d and e. The general profile resembles that of a laminar granular jump but the presence of the significant drop in volume fraction emphasizes the granular recirculation process.

Figure 5.7 shows the velocity profiles of a steep (recirculating) colliding jump. As for the laminar granular jumps, the incoming velocity profiles (red curves in Fig. 5.7) follow a Bagnold profile with a sliding velocity (Eq. (5.6)). The velocity profiles after the jump (blue curves in Fig. 5.7) are also similar to the velocity profiles after a laminar granular jump (blue curves in Fig. 5.5). However, because of the recirculation, the velocity profiles inside a steep colliding granular jump (green curves in Fig. 5.7) are very different from the ones in a laminar granular jump (green curves in Fig. 5.5). At a given position x inside the jump, the magnitude of the velocity is first increasing with the height, and then

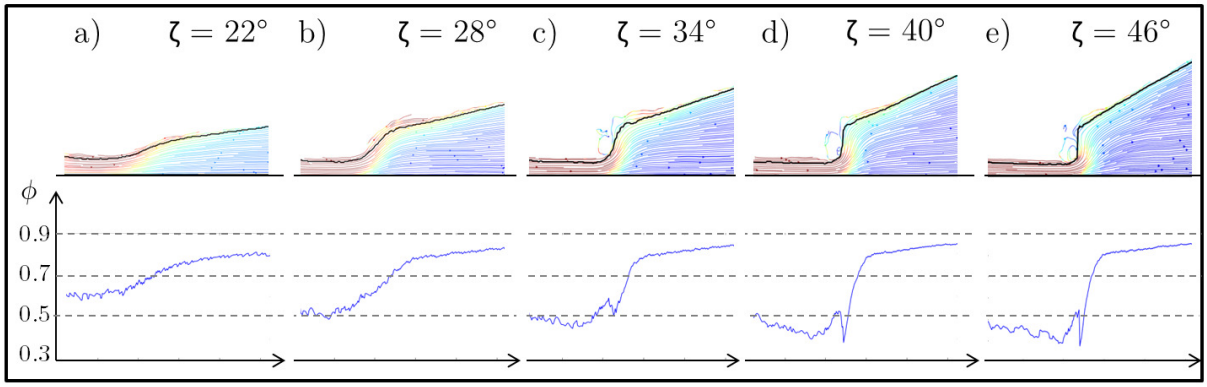

Figure 5.6: Transition from a laminar granular jump (cases a and b) to a steep colliding granular jump (cases c, d and e) by varying the slope: streamlines (first row) and longitudinal variation of the depth-averaged volume fraction (second row).

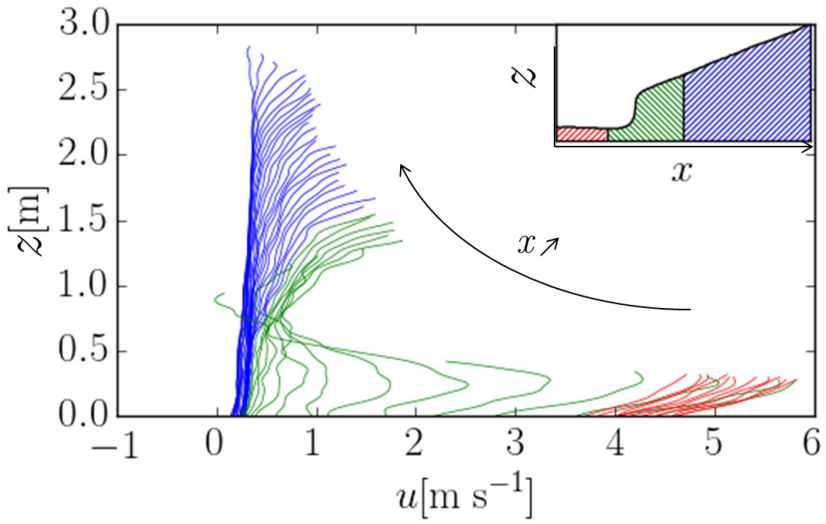

Figure 5.7: Velocity profiles of a steep colliding granular jump ($\zeta = 38°$, $d = 4$cm, $H = 0.5$m, $\mu = 0.5$) before (blue), inside (green) and after (red) the jump. The velocity profiles shown were measured every 0.12 m along the inclined plane.

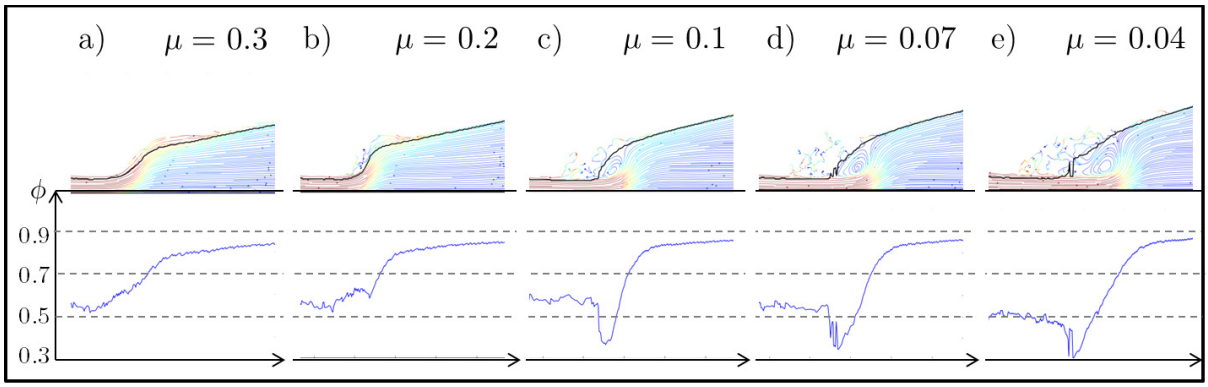

Figure 5.8: Transition from a laminar granular jump (a) to a hydraulic-like granular jump with a water-like roller (b,c,d,e) by varying the interparticle friction coefficient: streamlines (first row) and longitudinal variation of the depth-averaged volume fraction (second row).

strongly decreases beyond a certain position z. At some points, the decrease is so strong that the velocity along the inclined plane may even become negative, clearly indicating a recirculation process. At the same time, the sliding velocity is decreasing rapidly. Close to the end of the jump, the upper part of the velocity profile is increasing again, in a way that aligns with the outgoing flow after the jump.

5.3.3 Hydraulic-like granular jumps with an internal roller

The hydraulic-like jump is characterized by a water-like roller developing within the jump, below the free-surface of the flow (see Fig. 5.4b). Its dynamics is different from the one of the colliding jump with granular recirculation developing close to the free-surface, as discussed in the previous sub-section. The hydraulic-like jump is created when the interparticle friction is lowered below a critical friction coefficient μ_{cr}. As the interparticle friction decreases, the properties of the flow inside the jump tend to be similar to what is commonly observed for a frictionless fluid like water. The instable zone of the recirculation looks like the roller phenomenon known to appear in hydraulic jumps (see [44] and references therein). Like rollers in hydraulic jumps in water, this large recirculation zone seems to have a strong influence on the other features of the jump.

Figure 5.8 shows the transition from a laminar granular jump to an hydraulic-like jump with a presence of an internal water-like roller, in terms of the streamlines and the depth-averaged volume fraction. The water-like roller may extend along almost the entire length of the jump. The drop in volume fraction identifying the recirculation zone does not appear in the middle of the jump like for the colliding granular jumps described in the previous section, but at the very beginning, and it is wider, thus indicating a different leading mechanism at stake. This difference can also be seen by comparing the velocity fields shown by the colour of the streamlines depicted on Fig. 5.6 and Fig. 5.8. In the first case (cases c, d and e on Fig. 5.6), the rapid incoming flow stays attached to the free-surface and the recirculation takes place above the free-surface, while it penetrates far into the jump in the second case (cases c, d and e on Fig. 5.8), when the friction between the grains is very low, thus offering much less resistance to the incoming stream.

Figure 5.9 shows the velocity profiles of a hydraulic-like jump. Because of the low friction between the grains, the velocity profiles are very different from those in laminar granular jumps (Fig. 5.5) and colliding jumps with recirculation (Fig. 5.7). The incoming

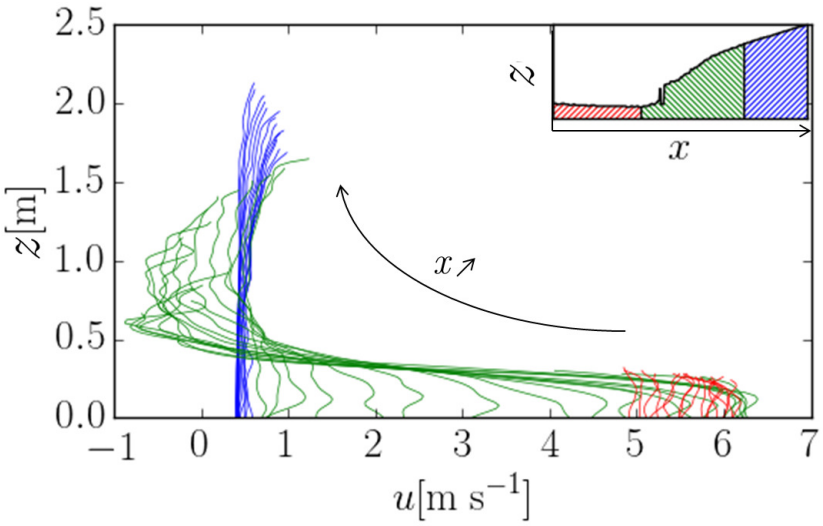

Figure 5.9: Velocity profiles of a hydraulic-like jump ($\zeta = 25°$, $d = 4$cm, $H = 0.5$m, $\mu = 0.04$) before (red), inside (green) and after (blue) the jump. The velocity profiles shown were measured every 0.12 m along the inclined plane.

velocity profiles do not follow a Bagnold profile anymore, as can be seen from the red curves drawn in Fig. 5.9. The incoming flows look like a plug flow with nearly no shear over depth. After the jump (blue curves in Fig. 5.9), the profiles are more similar to what we observe in both laminar and colliding granular jumps. This means that the friction between grains does not play such an important role after the jump. As those jumps are characterized by a roller, some velocity profiles inside the jump (green curves in Fig. 5.9) exhibit velocities that are sometimes largely negative. The overall shape of those velocity profiles inside the hydraulic-like jump with an internal water-like roller differs from the shape of the profiles measured in the steep colliding jump with free-surface recirculation.

It is worthy to note that Figs. 5.5, 5.7, and 5.9 all prove that the criterion based on the depth-averaged velocity defined in Sec. 5.2.3 is accurate enough to delimitate the three zones before, inside, and after the jump.

5.4 Jump length variation with input parameters

In this section, a detailed investigation on the influence of different parameters on the jump patterns and the length of the jump (based on the depth-averaged velocity as discussed in Sec. 5.2.3) is presented. First, the effect of varying the slope angle, the mass discharge and the grain diameter for a given interparticle friction greater than the bottom friction is studied. Second, the effect of varying interparticle friction is analysed.

5.4.1 Slope angle

The slope angle ζ, which controls the Froude number $Fr = \bar{u}/(gh\cos\zeta)^{1/2}$ of the incoming flow on a smooth bottom [19, 44], has a strong influence on the jump pattern: the diffuse jumps at small Fr become steeper with increasing Fr and a granular recirculation zone appears. That recirculation zone can be seen as the result of a stable granular flow (whose free-surface is inclined at ζ_0) being eroded by the thin and fast incoming collisional flow,

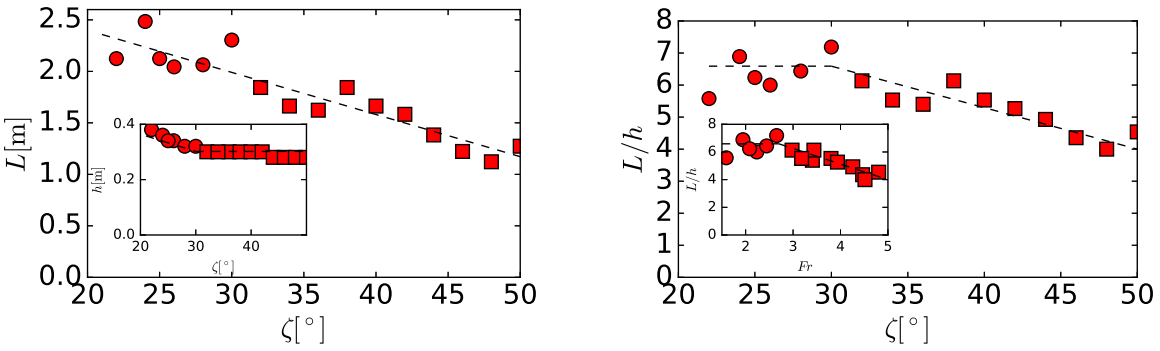

(a) (b)

Figure 5.10: Jump length L (a)nd jump length relative to incoming flow thickness L/h (b)ersus the slope angle ζ. Inset of (a) incoming thickness of the flow h as a function of ζ. Inset of (b) jump length relative to the incoming flow as a function of the Froude number. The circles correspond to the granular laminar jumps and the squares to the steep colliding granular jumps with recirculation.

and thus producing backward avalanche-flows starting from the top of the jump. The recirculation zone observed at high ζ ceases when the kinetic energy of the fast incoming collisional flow (and its high eroding capacity) is reduced at lower ζ.

The length of the jump is decreasing with the slope angle (see Fig. 5.10a). When the jump is purely laminar, the incoming thickness of the flow h is also decreasing with the slope angle, proportionally to the jump length (see circles in the inset of Fig. 5.10a). However, above a certain slope angle, the incoming thickness does not decrease any longer (squares in the inset of Fig. 5.10a). The relative jump length L/h is therefore constant when the jump is purely laminar (L is a function which increases linearly with h) and starts decreasing with the slope angle (and thus the Froude number) when some recirculation appears, as shown in Fig. 5.10b. This yields a decrease of L/h when Fr is increased (inset in Fig. 5.10b), in strong contrast with what would be observed in hydraulic flows (cf., the data gathered on figure 2d in [44] for water).

5.4.2 Mass discharge

The length of the jump is an increasing function of the opening height H of the gate at the exit of the tank, as shown in Fig. 5.11a. Comparing Fig. 5.11a with the inset of Fig. 5.11a, one observes that the increase of the jump length L with the opening height H, and the increase of the thickness h of the incoming flow with H are proportional (see black dashed lines in Fig. 5.11a). Thus, normalizing the jump length by the thickness of the incoming flow leads to the result that L/h is essentially independent of the mass discharge (Fig. 5.11b). In other words, the length L of the laminar granular jump is only a function of the incoming thickness h.

5.4.3 Grain diameter

Still considering laminar granular jumps, an increase in the grain diameter produces similar effects as the ones observed with an increase of the opening height of the reservoir. The increase of the length L of the jump with the grain diameter d is proportional to the increase of the thickness h of the incoming flow with d (see the black dashed lines in

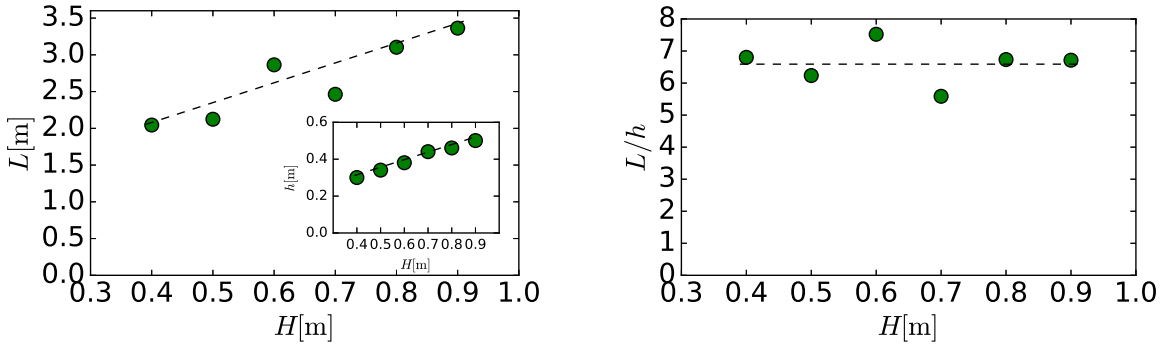

(a) (b)

Figure 5.11: Jump length L (a)nd jump length relative to incoming flow thickness L/h (b)ersus the opening height H at the exit of the tank (which controls the mass discharge). Inset in (a) thickness h of the incoming flow as a function of the opening height H of the reservoir. Since L versus H and h versus H have the same slope in (a) L/h in (b)s independent of the mass discharge.

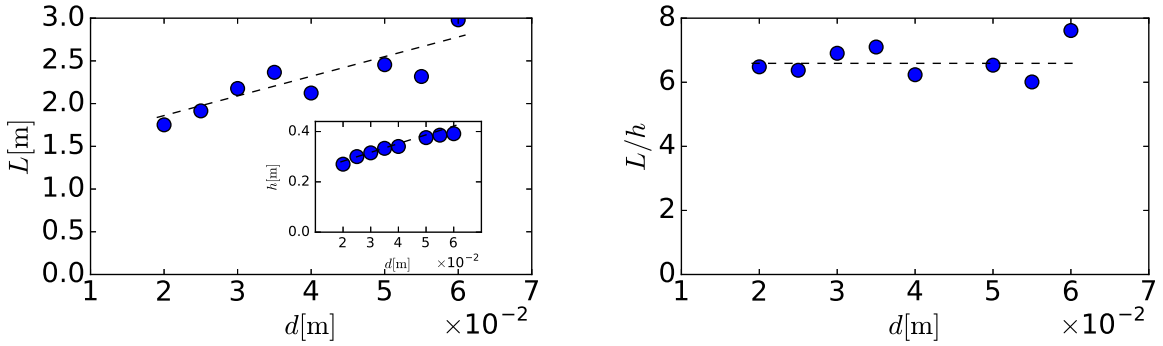

(a) (b)

Figure 5.12: (a)ump length L, (b)ump length relative to incoming flow thickness L/h versus the grain diameter d. Inset in (a) thickness h of the incoming flow as a function of d. L versus d and h versus d in (a)ave the same slope, thus L/h in (b)s independent of d.

Fig.5.12a and its inset). Thus, L is a function of h only, and the normalized length L/h remains essentially constant with the grain diameter as depicted in Fig. 5.12b.

5.4.4 Interparticle friction

The effect of varying the interparticle friction becomes significant once the interparticle friction falls below a critical friction μ_{cr}. For μ greater than μ_{cr}, the granular jump exhibits the smoothed streamlines, and the value of the interparticle friction does not have a strong influence on the jump length (see Fig. 5.13a). For μ smaller than μ_{cr}, the curvature of the streamlines increases and a hydraulic-like roller forms inside the jump, which seems to influence the jump length (Fig. 5.13a). However, the jump length relative to the thickness of the incoming flow remains nearly unchanged by varying μ.

To further highlight the transition from laminar granular jumps to hydraulic-like granular jumps (with the presence of a water-like roller), the evolution of Fr, h_*/h, ζ_0 and ϕ are drawn on Fig. 5.14. A sharp increase of h_*/h is observed when μ decreases below μ_{cr},

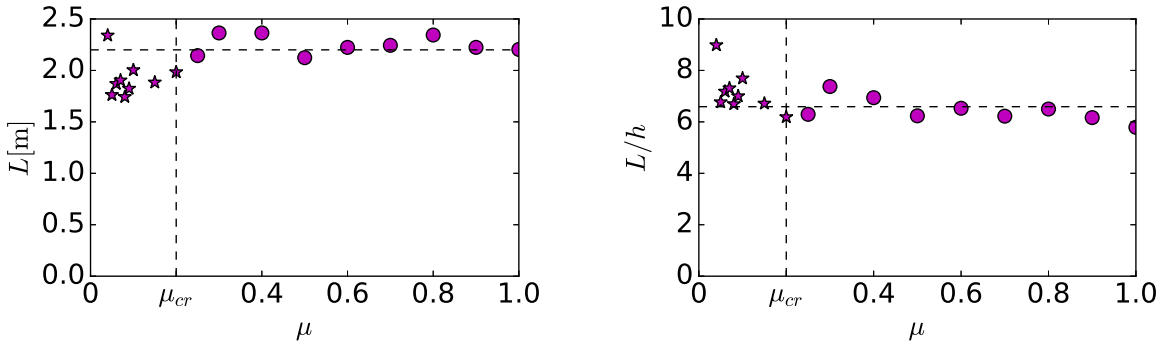

(a) (b)

Figure 5.13: (a)ump length L and (b)ump length relative to incoming flow thickness L/h, both against the interparticle friction coefficient μ. The circles represent laminar granular jumps and the stars denote hydraulic-like jumps with a water-like roller.

consistent with the simultaneous sharp increase of Fr, while ϕ remains nearly insensitive to μ. In addition, the angle ζ_0 at which the free-surface of the super-stable flow downstream of the jump is inclined drops and tends towards zero. This asymptotic behaviour resembles the phenomenon observed with water flows.

5.5 Discussion and conclusions

5.5.1 Jump height ratio

Referring to Eq.(5.1) described in the introduction, Fig. 5.15 depicts the thickness of the jump h_* relative to the thickness of the incoming flow h as a function of the Froude number of the incoming flow for all jumps. The prediction of the Bélanger equation [15], classically used in hydraulics, suggests:

$$\frac{h_*}{h} = \frac{1}{2}\left(\sqrt{1+Fr^2}-1\right), \tag{5.7}$$

and is also plotted. This is, in a fact, a reduced form of Eq.(5.1) for $\rho_*/\rho = 1$ and $L/h = 0$ (see [44] and references therein). Interestingly the relation between h_*/h and Fr is not affected by the jump type. However, there exists a noticeable gap between the prediction of the Bélanger equation and the numerical data, which is always above the Bélanger model for Fr in the range $1.5-4$ and tends to be closer to Bélanger equation at higher Froude numbers (range $4-5$ in this study). This trend is highlighted by the inset of Fig. 5.15. This result is in full agreement with previous experimental results (see figure 6 in [44]) and further highlights the need of a richer theoretical framework for predicting the jump height, for instance based on Eq.(5.1). In the following we discuss the main outcomes of the present study in terms of the jump length depending on the jump type considered.

5.5.2 Length of the jumps

Figure 5.16 shows the dimensionless length L/h of all the jumps investigated in this study as a function of the Froude number Fr of the incoming flow, by distinguishing the three

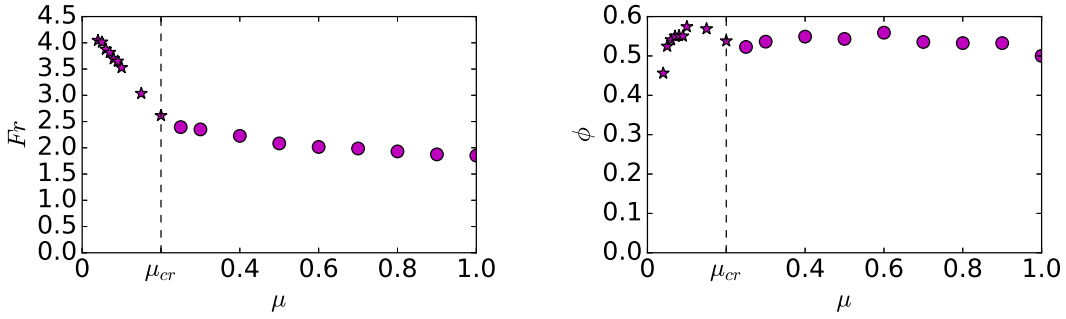

Figure 5.14: The transition from laminar granular jumps to hydraulic-like jumps, as visible in Fig. 5.4, seen through the change in different variables as a function of μ: (a)he Froude number Fr, (b)he incoming volume fraction ϕ, (c)he relative height of the jump h_*/h, and (d)he angle of the free-surface after the jump ζ_0. Stars represent hydraulic-like jumps and dots denote laminar jumps.

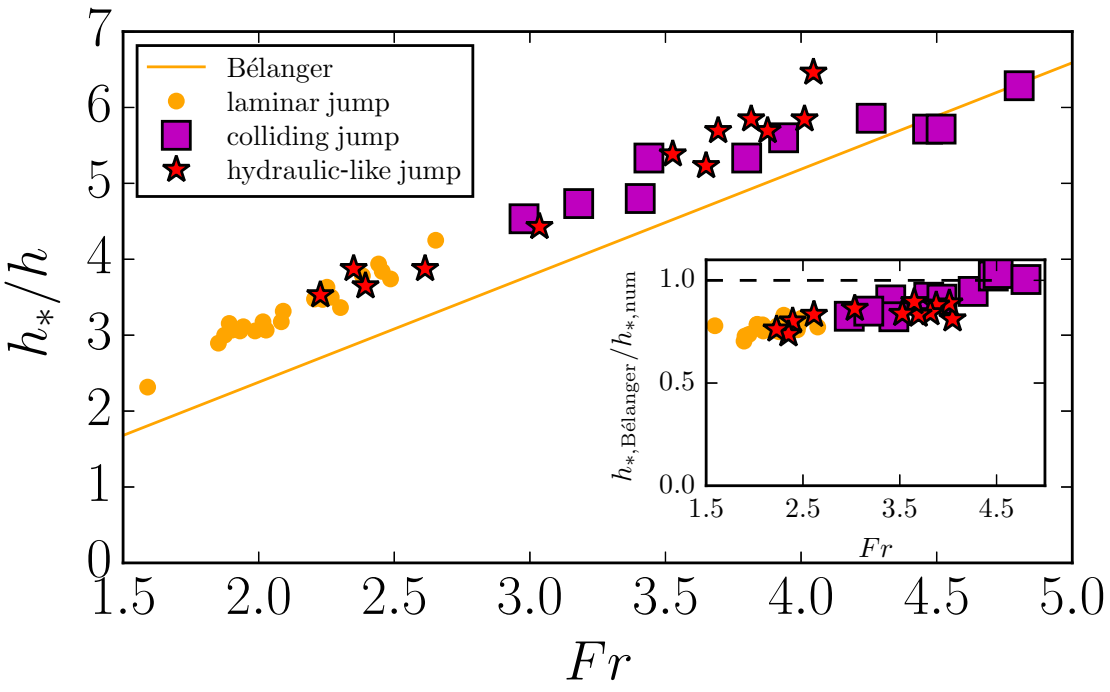

Figure 5.15: Jump height ratio, h_*/h, as a function of the Froude number, Fr, for all jumps investigated in the present study. The continuous line shows the prediction of the Bélanger equation used in hydraulics (see text).

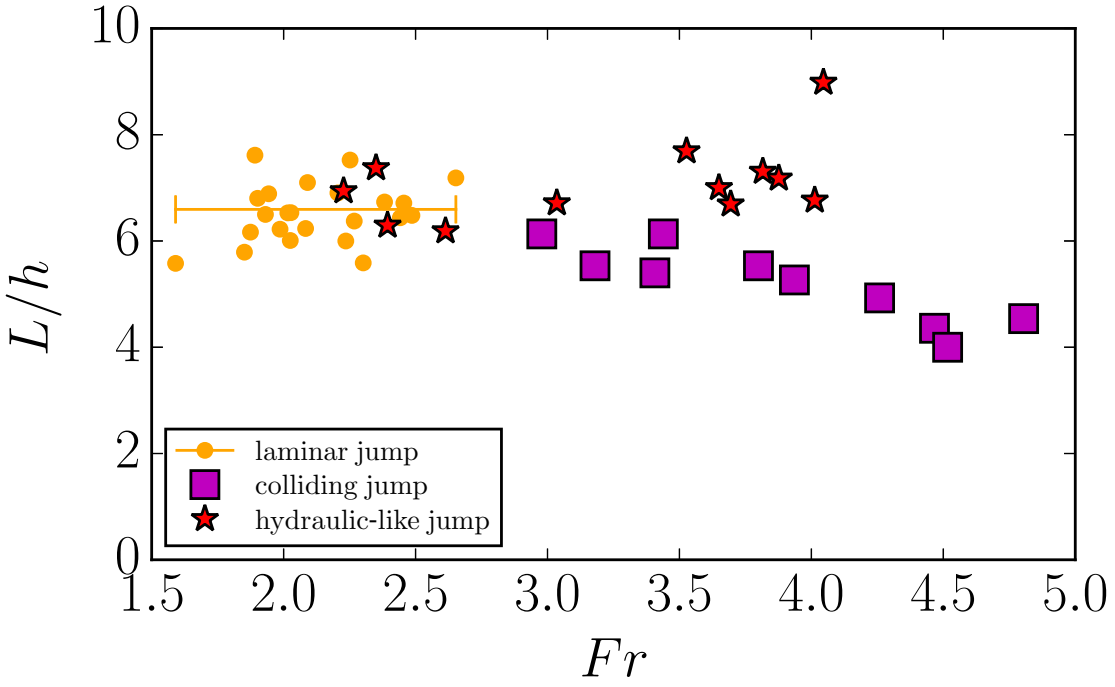

Figure 5.16: Dimensionless length of the jump L/h versus the Froude number Fr for all jumps. The orange-coloured line shows that L/h is rather constant (within the uncertainty for measuring the jump length) for laminar granular jumps.

types of jump identified. One can notice that the relation between L/h and Fr depends on the jump type, which is in strong contrast to the previous results that the relation between h_*/h and Fr is not affected by the jump type (see Fig. 5.15). Based on Eq.(5.1), this means that changes in μ_e or ϕ_*/ϕ, are expected to be balanced by a change in L/h, keeping the jump height ratio h_*/h versus Fr constant. This result strongly supports the idea that the length of the jump (L/h) and the constitutive law (μ_e and ϕ_*/ϕ) are interrelated. In other words, the variation of the jump length with Fr and the dissipation mechanisms inside the jump are closely related. Analysing the differences in terms of the jump length between the various types of jump may give insights into the different dissipation mechanisms inside the jump.

The laminar jump occurs for Fr in the range $1.5-2.5$ and its size shows some variability with Fr in that range: the mean value of L/h is around 6.5. The colliding jumps with a recirculation at their foot appear at higher slopes, which correspond to higher Fr. Instead of being constant, L/h is a decreasing function of Fr, ranging from $L/h = 6$ for $Fr = 3$ to $L/h = 4$ for $Fr = 5$. For the jumps with an internal water-like roller, L/h exhibits a slight increase with Fr. This behaviour resembles the increase of L/h with Fr as generally observed with water flows.

It is worthy to note that at a given Froude number, L/h is higher for the hydraulic-like jumps with an internal water-like roller than for the steep colliding jumps with recirculation taking place close to the free-surface at the foot the jump (see for instance the data for $Fr = 4$).

5.5.3 Effective friction depending on the jump type

In a previous work on standing granular jumps [44], a general relation depending on an effective friction coefficient μ_e was proposed (see Eq.(5.1) in the introduction). It is possible to use this relation in order to get this effective friction coefficient inside the jump for the different types of jumps identified in the present work. An expression for μ_e then reads as follows:

$$\mu_e = \tan\zeta + \frac{2Fr^2(\beta - \frac{\beta_*}{\frac{\rho_*}{\rho}\frac{h_*}{h}}) - k_*\frac{\rho_*}{\rho}\left(\frac{h_*}{h}\right)^2 + k}{K_0\frac{L}{h}\left(1 + \frac{\rho_*}{\rho}\frac{h_*}{h}\right)} \tag{5.8}$$

with k and k_* the earth pressure coefficients before and after the jump, which were both taken equal to 1 in this study (for further discussion see [60, 17, 44]), and β and β_* the Boussinesq momentum coefficients, which correspond to the ratios between the depth-averaged value of the velocity-squared and the square of the depth-averaged velocity ($\beta = \overline{u^2}/\bar{u}^2$). K_0 is a shape factor so that the weight per unit width of the jump can be written as $w = K_0 gL(\rho h + \rho_* h_*)/2$, as initially introduced by [61]:

$$K_0 = \frac{2\int_0^L \rho(x)h(x)\,\mathrm{d}x}{L(\rho h + \rho_* h_*)}, \tag{5.9}$$

where $\rho(x)$ and $h(x)$ are the density and height of the flow inside the jump.

This effective friction coefficient μ_e is a good indicator of the efficiency of energy dissipation inside the jump for each type of jump. The variation of μ_e with Fr is plotted for all our jumps in Fig. 5.17. One observes a remarkable difference between the types of jump: μ_e is independent of Fr for the laminar granular jumps but is an increasing function of Fr for the steep colliding granular jumps, and even becomes a decreasing function of Fr for the hydraulic-like jumps. Note that the general relation established under the assumption of a Coulomb rheology and proposed for granular jumps by [44] may be questionable when the interpartticle friction coefficient μ is lower than μ_{cr}. As such, the value μ_e extracted from Eq.(5.8) should be considered with caution in the case of hydraulic-like jumps with a roller. This is, however, a useful way to further highlight the differences between the latter jump type and the other jumps.

Figure 5.17 and the general behaviour of the jumps (streamlines patterns, recirculation or not, evolution of the length with input parameters) can help in drawing some underlying assumptions for the development of a dissipation model depending on the jump type.

The effective friction inside the jumps, μ_e, and the length of the jumps relative to the incoming flow thickness, L/h, are constant with the Froude number in case of laminar granular jumps (circles in Fig. 5.10a and 5.17). The jump length is sensitive to changing the thickness of the flow: increasing either the mass discharge (through H) or the grain diameter (d) produces an increase of the jump length, but the ratio L/h remains independent of either H or d. The streamlines show a gradual transition from the stable state upstream from the jump to the stable state after the jump, and the granular flow is dense. All of this suggests that the dominant dissipation process for this type of jumps stems from enduring frictional contacts between the grains.

As the recirculation inside the jump increases, the length L of the jump decreases (squares in Fig. 5.10a), while the effective friction μ_e within the jump increases (squares in Fig. 5.17). This highlights the dissipative role of the recirculation phenomenon. In those types of jumps, there are still enduring frictional contacts between the grains, but binary gaseous-like collisions come into play in the recirculation zone (evidenced by the overall

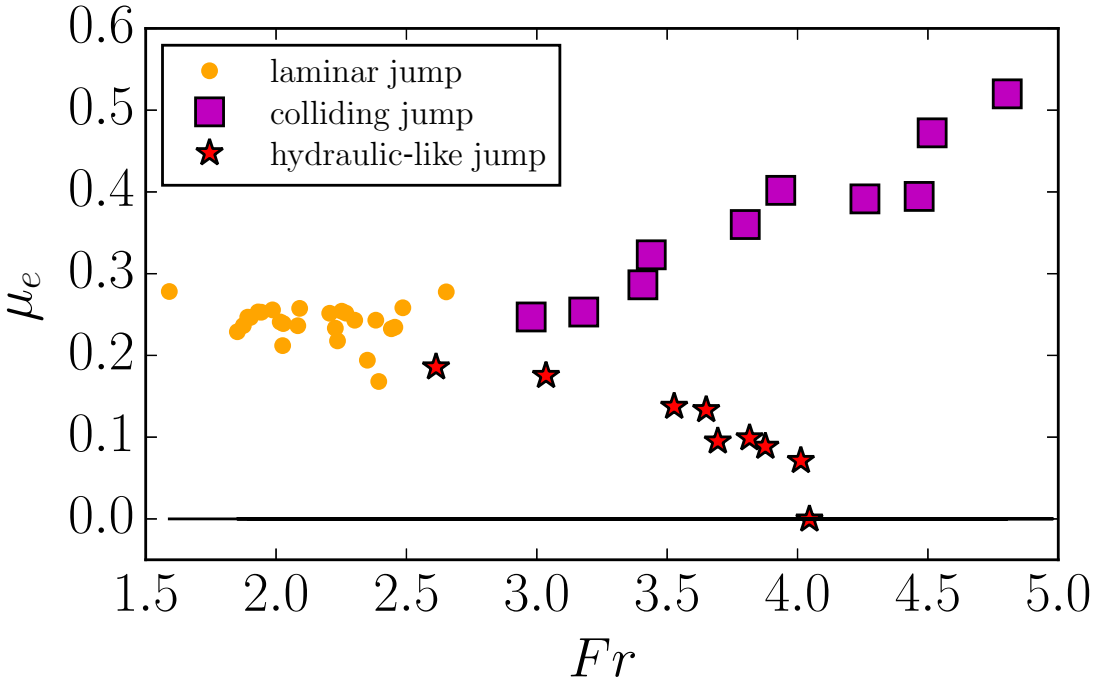

Figure 5.17: Effective friction inside the jump μ_e extracted from Eq. (5.8) as a function of the Froude number for all types of jumps.

shapes of the streamlines and the drop in the depth-averaged volume fraction along the chute). This observation indicates that the steep jump, with a granular recirculation zone, is efficient at dissipating energy over a shorter distance. The presence of the recirculation zone characterized by active bouncing of particles probably contributes to higher rates of energy dissipation. This suggests that a theory describing energy dissipation in granular jumps at high ζ (high Fr) should not be limited to including a frictional term only but should also account for a collisional term. For such jumps with fast and thin incoming flows, μ_e may be written (in first approximation) as the sum of a constant Coulombian friction μ_s and a velocity-squared dependent term in the form αFr^2. Note that, however, we could not find any relevant values of μ_s and α to fit at the same time both the laminar (circles in Fig.5.15) and the colliding (squares in Fig. 5.17) granular jump data, in contrast to the analysis proposed earlier by [44], applied to jumps measured in the laboratory [19]. This result motivates future work.

Figure 5.17 shows that as the friction between the grains decreases (stars shown on the plot), the effective friction inside the jump μ_e decreases as well. This is because as μ decreases, the enduring frictional contacts between the grains are less efficient at dissipating energy and a water-like roller can form. There is a large drop in volume fraction across most of the jump, indicating a very loose grain packing inside that roller. Figure 5.17 shows that μ_e, extracted from Eq.(5.8), may even reach zero for $\mu = 0.04$. Note that the incoming flows produced by simulations with μ below 0.04 (not shown here) were so gaseous that it was impossible to measure the depth-averaged variables properly. For the hydraulic-like jumps, because of the presence of that roller, it will certainly be relevant to infer a general jump height relation relying on a turbulent-like effective shear stress (similar to the one proposed for instance in [44] for water flows), instead of the

Coulombian shear stress which was deemed necessary for the derivation of Eq.(5.8). The transition from a steep colliding granular jump to a hydraulic-like jump with a roller is caused by the lowering of interparticle friction. This process of the transformation of the granular recirculation at the foot of the jump into a fully-developed roller inside the jump warrants further investigation.

Chapter 6

Energy dissipation in numerical granular jumps

This chapter builds on the conclusions of Part I on the need to focus on the notion of energy conservation in order to obtain a closure relation for jumps down inclines. Through not entirely conclusive, preliminary theoretical work was undertaken to recover such closure equation based on the depth-averaged energy. The following chapter details the work done on the numerical simulations to measure and understand better the dissipation of energy inside the jumps. Section 6.1 explains how the energy is calculated, Sec. 6.2 shows the evolution of the conservative part of the energy along the incline, and Sec. 6.3 focuses on the energy loss. Finally, Sec. 6.4 compares the energy loss along the incline calculated from coarse-graining, and the energy loss directly estimated from the depth-averaged flow properties, as a first step for recovering a theoretical closure relation in the future.

6.1 Introduction

In Part I, depth-averaged mass and momentum equations were used to predict the geometry of granular jumps. However, the prediction involved two unknowns (the flow depth after the jump h_* and the jump length L) with only one equation. As explained in the conclusion of Part I (Sec. 2.5), a possible research path could be to consider the depth-averaged conservation of energy. The two-dimensional Discrete Element Method simulations allow to access all the parameters inside the jumps, including the conservative part of the energy, from which we can deduce the energy loss from the energy conservation equation:

$$\frac{dE_c}{dx} = E_l(x) \tag{6.1}$$

with E_c the conservative part of the energy, and E_l the energy loss per unit length.

In the case of a granular flows down inclines, several types of conservative energy could be identified for the individual particles:

- The kinetic energy $E_k = \frac{1}{2}m(u_x^2 + u_z^2) = \frac{2}{3}\rho_p\pi\left(\frac{d}{2}\right)^3(u_x^2 + u_z^2)$, with m the mass of the particle, u_x its velocity along the $x-$axis, u_z its velocity along the $z-$axis, ρ_p its density, and d its diameter.

- The gravitational potential energy $E_g = mgZ = \frac{4}{3}\rho_p\pi\left(\frac{d}{2}\right)^3 g\,(-x\sin\zeta + z\cos\zeta)$, with Z the vertical altitude of the particle, and x and z the coordinates of the particle respectively along the $x-$axis and the $z-$axis.

- The elastic potential energy $E_e = \frac{1}{2}k\delta^2 = \sum_{\text{inter}}\frac{1}{4}k\delta^2$ with the subscript $-$inter$-$ referring to the coordination number, k the stiffness of the particles and δ the deformation of the particles which, in the case of DEM simulations, corresponds to the interpenetration of the glass beads.

The energy loss in granular flows down inclines is generally caused by friction and collisions between the particles. Like for the previous discrete variables needed for a continuum mechanics description, coarse-graining was used to establish the continuum conservative part of the energy (See [45] for more details).

Section 5.2.2 (Chap. 5) shows that for energy, the coarse-graining gives the following equation for the conservative energy at point $\mathbf{r}$ and time t:

$$E_c(\mathbf{r},t) = \frac{\sum_{\|\mathbf{r}-\mathbf{r_i}(t)\|\leq c}\left(e_i(t)m_i\mathcal{W}(\|\mathbf{r}-\mathbf{r_i}(t)\|\right)}{\sum_{\|\mathbf{r}-\mathbf{r_i}(t)\|\leq c}\left(m_i\mathcal{W}(\|\mathbf{r}-\mathbf{r_i}(t)\|\right)}. \tag{6.2}$$

As seen in Sec. 5.2.2, $\mathcal{W}$ represents a Lucy function commonly used for the coarse-graining (Eq. (5.3)), $\mathbf{r_i}$ is the coordinate of point i, m_i the mass of the particle number i, and $e_i(t)$ the conservative energy for the particle number i, at time t:

$$e_i(t) = \rho_p\, 4/3\,\pi\left(\frac{d}{2}\right)^3\left[\frac{1}{2}\left(u_{ix}^2(t)+u_{iz}^2(t)\right)+g\left(-x_i(t)\sin\zeta+z_i(t)\cos\zeta\right)\right]+\sum_{inter_i}(t)1/4\;k_i(t)\delta_i^2(t). \tag{6.3}$$

After calculating the field of conserved energy at any point $\mathbf{r}$, this field could be averaged over several uncorrelated times (thanks to the fact that we are at steady state). The depth-averaged value is then calculated with a ponderation of the density, on the same way as any other quantity, as described in Sec. 5.2.2:

$$E_c(x) = \frac{\sum_{z\leq h(x)}\rho(x,z)E_c(x,z)}{\sum_{y\leq h(x)}\rho(x,z)}. \tag{6.4}$$

6.2 Variation of energy along the incline

The variation of the depth-averaged conservative energy along the incline gives information on the dissipation of energy (energy loss) along the incline. Some curves showing the conservative energy E_c minus the conservative energy at the beginning of the jump E_{c1} (so that the energy just before the jump correspond to the point $(0,0)$) along the incline have been plotted in Fig. 6.1. Each plot represents the variation of energy loss as a function of one parameter per figure, indicated above the colour bar. In all these graphs, the jump corresponding to $\zeta = 25°$, $H = 0.5$m, $\mu = 0.5$, $d = 0.04$m is highlighted by the blue line. The insets represent the derivatives of the curves in the main graph, which correspond to the energy loss per unit length along the incline E_l.

From a qualitative point of view, from all the curves of Fig. 6.1, we see that the energy is decreasing at a constant slope across the incoming flow (before the point $(0,0)$). This is seen in the insets, where the derivative of the conservative energy is a constant. This means that the energy loss in the incoming flow is always a linear function of x. Then, inside the jump, the conservative energy is decreasing at a much higher negative slope, and is not linear with x. The derivative of the variation of conservative energy, that we can see in the insets, is much lower inside the jumps than in the inflows or outflows. This shows that the jump is very efficient at dissipating energy. And finally, after the jump, the energy loss is again a linear function of x. The insets show that this slope is a little bit higher than before the jump. In other words, we find there is more dissipation in the subcritical flow (after the jump) than in the supercritical flow (before the jump).

Figure 6.1a shows the curves of the depth-averaged conservative energy along the incline for the default values in Tab. 5.1 (Chap. 5), except for the slope angle, which

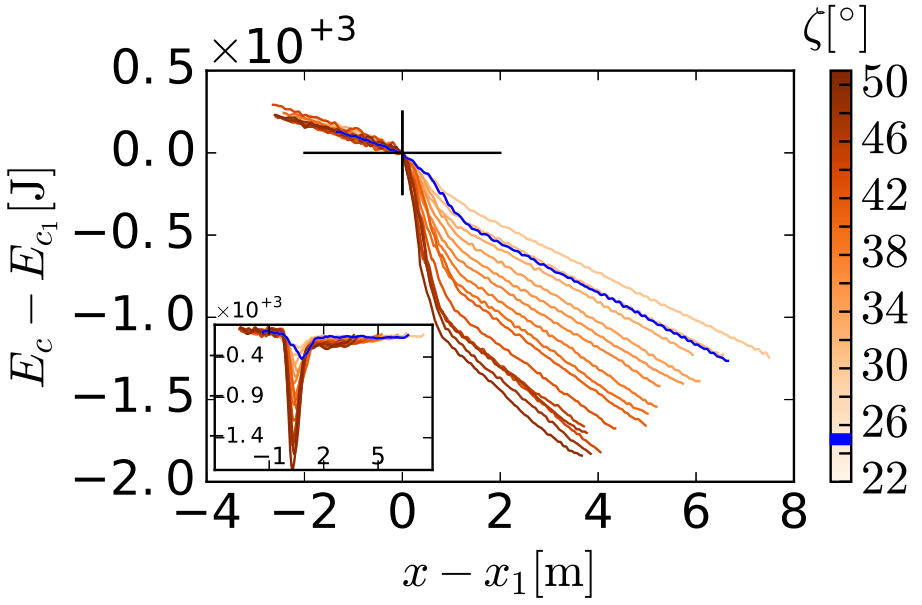
$\times 10^{+3}$
$\zeta[^\circ]$
0.5
0.0
−0.5
−1.0
−1.5
−2.0
$E_c - E_{c_1}$[J]
−4 −2 0 2 4 6 8
$x - x_1$[m]
50
46
42
38
34
30
26
22
$\times 10^{+3}$
0.4
0.9
1.4
−1 2 5

(a)

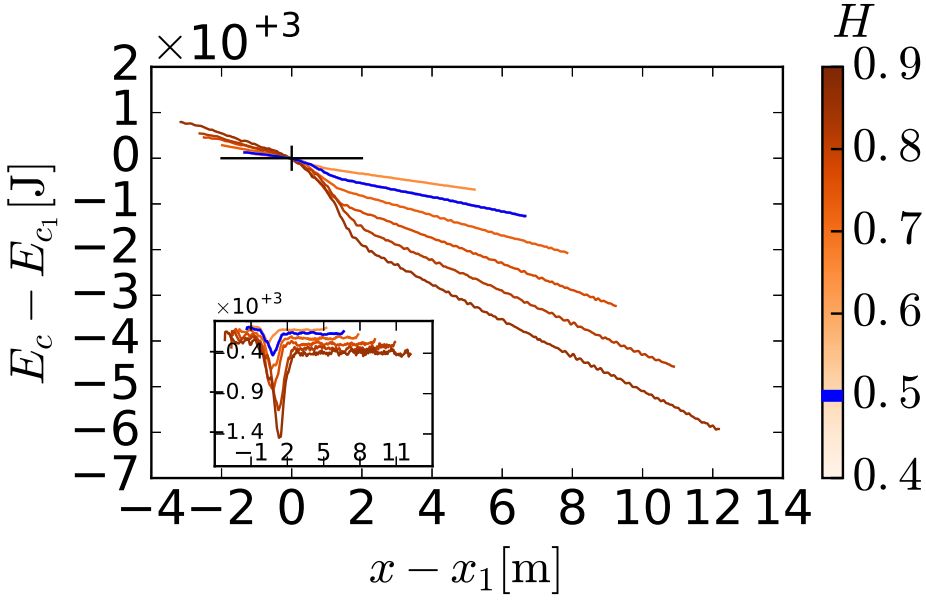
$\times 10^{+3}$
H
2
1
0
−1
−2
−3
−4
−5
−6
−7
$E_c - E_{c_1}$[J]
−4 −2 0 2 4 6 8 10 12 14
$x - x_1$[m]
0.9
0.8
0.7
0.6
0.5
0.4
$\times 10^{+3}$
0.4
0.9
1.4
−1 2 5 8 11

(b)

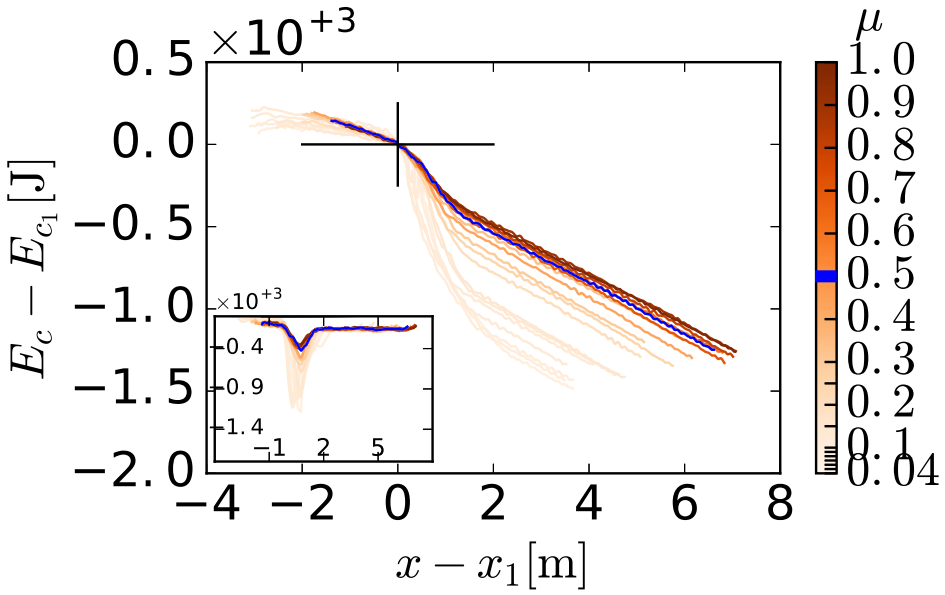

(c)

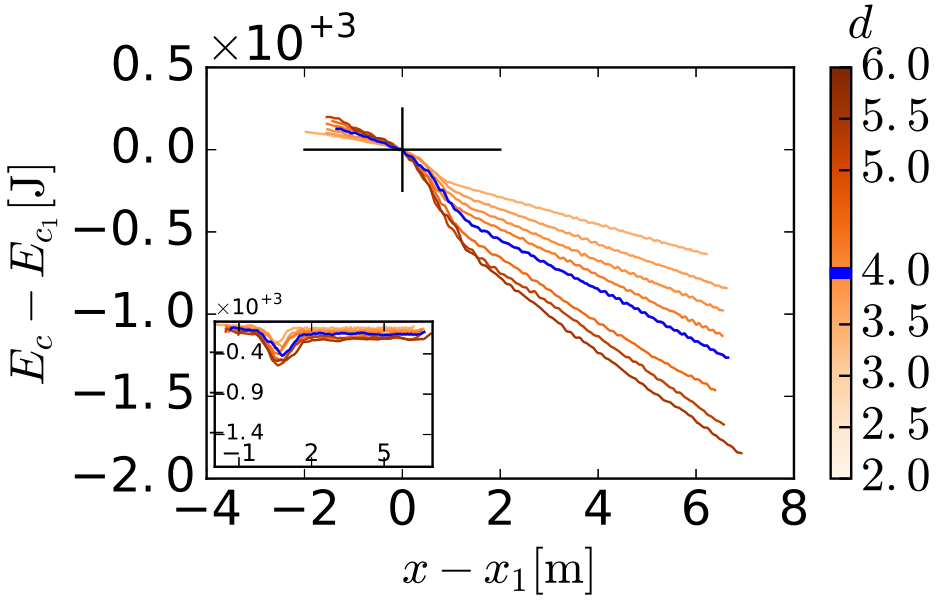

(d)

Figure 6.1: Depth-averaged conservative energy along the incline. The point $(0, 0)$ corresponds to the beginning of the jumps. The different curves correspond to a change of (a) the slope angle ζ of the incline, (b) the opening height of the reservoir h corresponding to the mass discharge, (c) the interparticle friction between grains μ and (d) the grain diameter d. The insets correspond, with the same colour legend, to the derivative of the curves of the main figure, which means the energy loss along the incline. The x-axis of the insets is the same as the $x-$axis of the main graph, and the $z-$axis of the insets is always varying from 0 (top) to -1800 (bottom) for all graphs.

varied from 22° (brightest curve) to 50° (darkest curve) with an increase of 2° between each curve. Apart from the general observation on the energy curves, it is noticeable that the slope angle of the incline does not have any influence on the energy loss of the incoming flow (the curves are superimposed on Fig. 6.1a and its inset). However, the higher the slope angle, the more energy is dissipated inside the jump. On the subcritical flow after the jump, the slope angle has a slight influence on the energy loss, with a little bit more dissipation at higher slopes, as seen in the inset. The fact that the variation of energy along the jump is dependent on the slope angle also proves the necessity to include explicitly the slope angle as a parameter into the mass and momentum equations in order to obtain a relation for the jumps (see Chap 2). The Rankine-Hugoniot point of view where the jump is a shock with no volume does not take into account the slope angle in the equation (see Bélanger's equation Eq. (2.1) in Chap. 2) and is thus not sufficient to describe a granular jump down an incline.

Figure 6.1b shows a different behaviour for the effects of varying the mass discharge through the opening height H at the reservoir exit. The linear energy loss with x across both the incoming supercritical flow and the outgoing subcritical flow is dependent on the discharge. For both flows, the higher the discharge, the higher the dissipation rate. The inset also shows that jumps with higher discharges dissipate more energy.

Figure 6.1d represents the conservative energy along the incline for several grain diameters. We can see that either before, during, or after the jumps, the bigger the grain diameter, the more energy is dissipated. Increasing the grain diameter has exactly the same effect as increasing the opening at the reservoir exit H.

Figure 6.1c represents the conservative energy along the incline for different interparticle friction coefficients μ. Two different behaviours are observed depending on the μ coefficient. For μ higher than a certain value (about 0.2), the curves (dark curves) collapse over each other. This means that the energy along the incline does not depend on the interparticle friction coefficient μ. However, under this critical value for μ (brightest curves), the dissipation of energy along the incline strongly depends on the interparticle friction. The incoming and outgoing flows, respectively before and after the jump, are a little bit less efficient at dissipating energy. However, in the jump region, the lower the interparticle friction coefficient, the more energy is dissipated inside the jump. This is fully consistent with the results obtained in the previous chapter (Chap. 5, published in [45]): Sec 5.4.4 evidenced the existence of a critical interparticle friction coefficient $\mu_{cr} = 0.2$. Beyond this critical value μ_{cr}, the jumps are laminar and the interparticle friction does not have any influence on the characteristics of the jumps. But for $\mu < \mu_{cr}$ the interparticle friction has a strong influence on the jumps patterns: the jumps develop an internal roller that increases when μ decreases, and some characteristics of the jumps become closer to the characteristics of hydraulic jumps. The jump height ratio h_*/h increases while the angle of the free-surface after the jump tends toward zero. This result shows that the more the granular jump develops a water-like roller, the more it is efficient at dissipating energy.

6.3 Energy loss within the jump

We define here the linear energy loss per unit length from Eq. (6.1) as the derivative of the conservative energy along the incline (insets in Fig. 6.1). It is possible to define two regions where the energy loss per unit length is linear with x: one in the incoming flow before the jump (E_l^{up}), and one on the downstream part of the incline after the jump

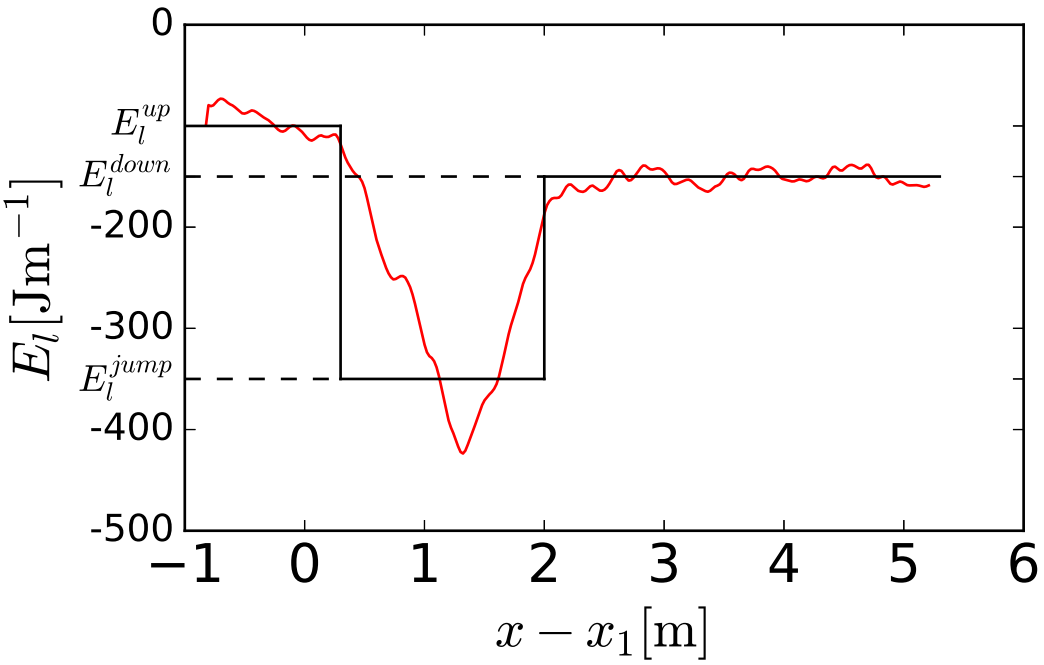

Figure 6.2: Example of the determination of three Energy loss coefficients E_l^{up}, E_l^{down}, and E_l^{jump} for one jump.

(E_l^{down}). The energy loss per unit length in the region inside the jump is not linear as it presents an inflexion point. However, it is not far from its linear approximation that we decided to use in the following (E_l^{jump}). The beginning of a jump is defined as the position in the incline where the slope of the energy curve is changing for the first time ($x = 0$ in Fig. 6.1) and the end of the jump is when it becomes constant again. This definition of the length gives exactly the same results as the definition of the length with the velocity (see Sec. 5.2.3) for the beginning of the jump, and a comparable result within the margin of error for the end of the jump, which is a little bit harder to determine. Figure. 6.2 shows how those energy loss coefficients are calculated in an example for one jump. The red curve corresponds to the derivative of the conservative energy, which represents the energy loss per unit length along the incline (like the insets of Fig. 6.1), and the black curve corresponds to the approximate energy loss per unit length, with a constant for each jump region.

Figure 6.3 shows the evolution of this energy loss per unit length E_l^{up}, E_l^{jump}, and E_l^{down} as a function of the control parameters: the slope ζ, the opening at the exit of the reservoir H, the interparticle friction between grains μ and the grain diameter d.

Figure 6.3 shows the same results as Fig. 6.1, with the specific effect of each parameter on the three flow regions easier to identify. The energy loss coefficient is plotted in red for the incoming flow (E_l^{up}), in blue for the outgoing flow (E_l^{down}), and in green inside the jump region (we remind here that it is an approximate energy loss coefficient, E_l^{jump}, based on the assumption that E_l is roughly linear with x). Figure 6.3a suggests that increasing the slope angle ζ is a very efficient way to increase the jump capacity to dissipate energy. However, the energy loss coefficient in the incoming flow keeps constant and the energy loss coefficient in the downstream flow barely increases. When the slope angle increases, the velocity of the incoming flow $\bar{u}$ increases. The kinetic energy E_k increases linearly

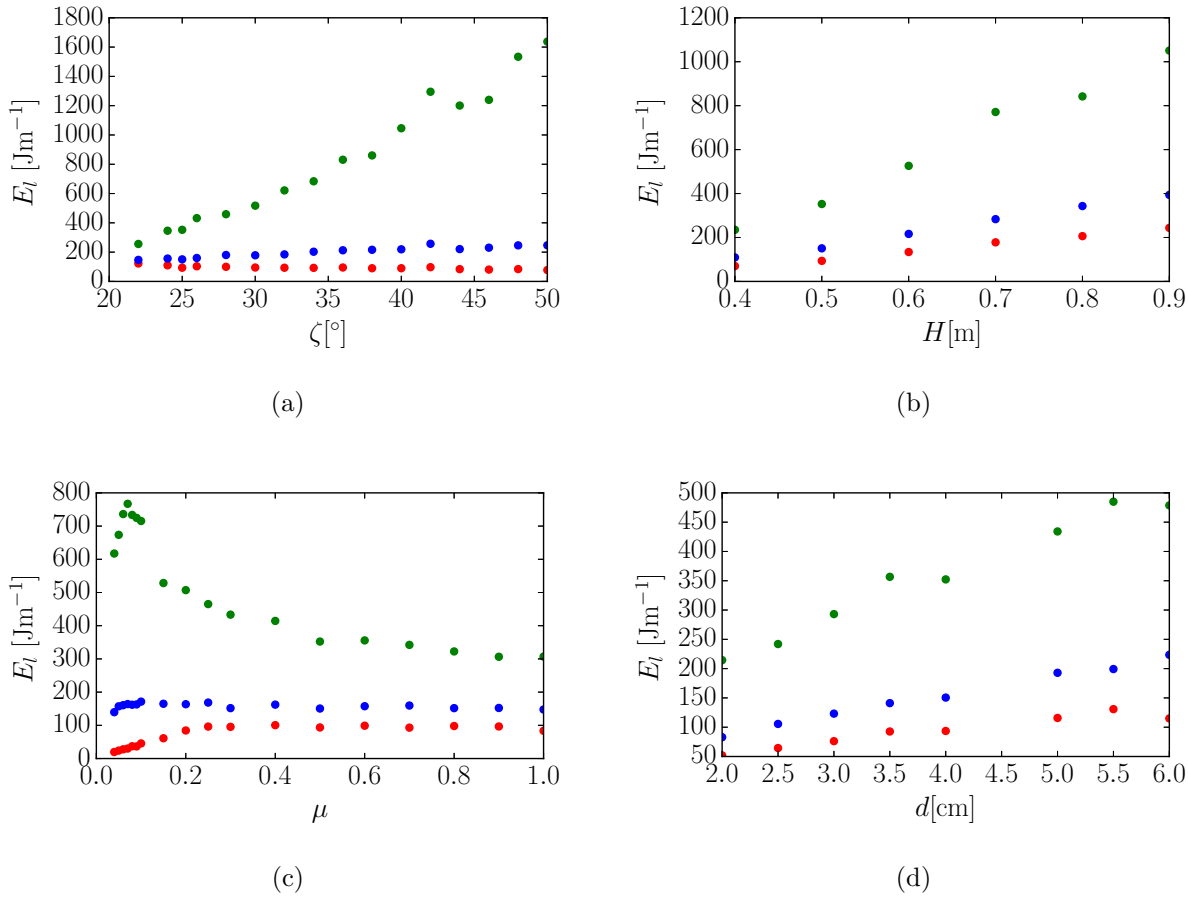

Figure 6.3: Energy loss per unit length before (red), during (green) and after (blue) the jumps, as a function of the slope angle of the incline ζ, the opening of the tank exit H, the interparticle friction coefficient between grains μ, and the grain diameter d.

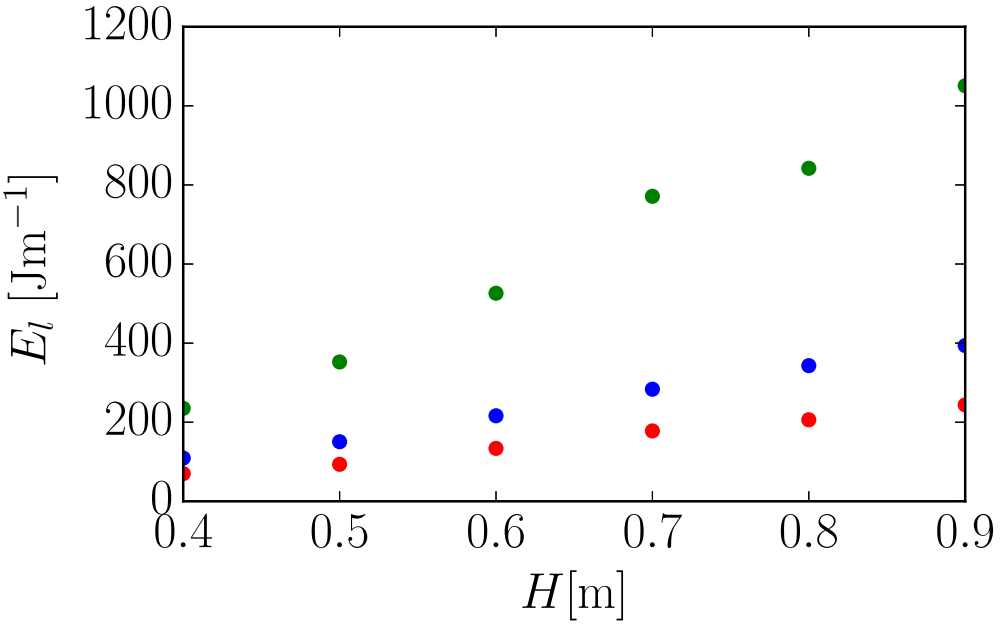

Figure 6.4: (a): Energy loss per unit length before (red), during (green) and after (blue) the jumps, varying only the opening of the tank exit H (x) and the grain diameter d (+), as a function of the incoming flow height h.

with the square of the velocity $\bar{u}^2$. Then, the jumps that form on inclines at a higher slope angles ζ need to dissipate a lot more energy. We can see that the kinetic energy is mostly dissipated in the jump region, and not at all in the incoming flow region.

In Figs. 6.3b and 6.3d, the energy loss coefficients are evolving exactly in the same way: anywhere in the flow region, the capacity to dissipate energy increases with d or with H. This behaviour is explained by the increase of the incoming flow height h, which can be caused either by the increase of the grain diameter d or the opening of the reservoir H. This has already been seen in the previous chapter (Chap. 5, published in [45]) and is confirmed with Fig. 6.4. This figure shows that increasing d or H results in an increase of h, which controls the energy loss. Indeed, the gravitational potential energy E_g is increasing linearly with the flow height, and the jumps with a high incoming flow height h will need to dissipate more energy. We can see that the gravitational potential energy is dissipated in the three flow zones.

Figure 6.3c again allows to see the threshold effect related to the interparticle friction coefficient μ on the dynamics of granular flows. The energy loss per unit length decreases inside the jump region and increases in the other regions of the flow when μ increases but stays below a critical value. When it reaches this critical value μ_{cr}, the effect of μ is much lower on the energy loss inside the jump, and has nearly no effect in the incoming and outgoing flows. The interparticle friction coefficient μ has an effect on both the kinetic and the gravitational potential energies, which may explain the complicated behaviour observed in Fig. 6.3c. The latter is different from the behaviour shown in Figs. 6.3b and 6.3d when H and d, both encapsulated in h, are varied and lead to a monotonic increase of E_l with h (Fig. 6.4) that mainly controls the potential energy of the granular flow.

6.4 Comparison between coarse-grained exact energy and hydrodynamic energy from depth-averaged flow properties

The coarse-grained, depth-averaged energy E_c is calculated from the two steps explained in Sec. 6.1. It is considered as the right amount of energy along the jump. However, in order to obtain the energy in a hydrodynamic point of view, without knowing everything that happens inside the jump, we want to calculate the energy from the hydrodynamic, depth-averaged flow properties. From the depth-averaged flow properties, it is possible to get the hydrodynamic flux of energy during one time unit (1 sec):

- Kinetic energy $E_k^{hydro}(x) = \frac{1}{2}\rho(x)\bar{u}(x)h(x)d\beta(x)\bar{u}^2(x)$, with $\rho(x)$ the depth-averaged density at point x of the incline, $\bar{u}(x)$ the depth-averaged velocity at point x, $h(x)$ the flow height at point x, and $\beta(x)$ the Boussinesq coefficient of the flow at point x, which corresponds to the depth-averaged velocity square over the square of the depth-averaged velocity: $\beta = \overline{u^2}/\bar{u}^2$.

- Gravitational potential energy $E_g^{hydro}(x) = \rho(x)\bar{u}(x)h(x)dg\left(-x\sin\zeta + \frac{h(x)}{2}\cos\zeta\right)$.

- Elastic potential energy $E_e^{hydro} \approx 0$. It is difficult to express the elastic potential energy in a hydrodynamic, depth-averaged point of view because of its intrinsic discrete nature. However, we will see that the elastic potential energy is so low compared to the kinetic and gravitational potential energies that it can be considered as negligible.

Then, the flux of energy from depth-averaged values becomes:

$$E_c^{hydro}(x) = \rho(x)\bar{u}(x)h(x)d\left[\frac{1}{2}\left(u(x)^2 + v(x)^2\right) + g\left(-x\sin\zeta + \frac{h(x)}{2}\cos\zeta\right)\right]. \quad (6.5)$$

In order to compare it to the energy calculated from coarse-graining, it is necessary to use the same units, as E_c is expressed in Joules, and E_c^{hydro} in J.sec^{-1}. For that purpose, E_c^{hydro} is multiplied by the mass of one particle (m_p in kg) divided by the flux of particles during one second (m_{flux} in kg.s^{-1}):

$$\frac{m_p}{m_{flux}} = \frac{\rho_p(4/3)\pi\left(\frac{d}{2}\right)^3}{\rho(x)h(x)u(x)d} = \frac{\pi d^2}{6\phi(x)h(x)u(x)}, \quad (6.6)$$

which is expressed in seconds.

This simple approach allows to calculate the hydrodynamic energy along the flow, and then obtain the energy loss per unit length. The energy loss per unit length inside the jump is expressed as the following:

$$E_l^{hydro} = \frac{E_{c\_before}^{hydro} - E_{c\_after}^{hydro}}{L} \quad (6.7)$$

with $E_{c\_before}^{hydro}$ and $E_{c\_after}^{hydro}$ the hydrodynamic energies at the beginning and at the end of the jump respectively, where L is the jump length.

This hydrodynamic point of view relies on two main assumptions: the elastic potential energy is negligible and the depth-averaging point of view is well captured by what happens at the micro-scale. However, this way to access the energy is the easiest possibly,

symbols	name in [45] or Chap. 5	$\zeta[^\circ]$	H[m]	d[m]	μ
orange points	laminar jumps	$22-30$	0.5	0.04	$0.25-1.0$
purple squares	steep colliding jumps	$32-48$	0.5	0.04	0.5
red stars	hydraulic-like jumps	25	0.5	0.04	$0.04-0.2$
orange cruxes	-	$<=30$	$0.4-1.1$	0.04	0.5
green cruxes	-	$>=30$	$0.4-1.1$	0.04	0.5
blue plus	-	42	$0.5-1.1$	0.04	0.5

Table 6.1: Colours and symbols used in Figs. 6.5 and 6.6 to distinguish between different types of jumps and / or numerical input conditions.

even from direct measurements in physical laboratory tests, and thus likely the best way for obtaining an usable closure relation to predict the geometry of the jumps.

The first assumption can be verified by comparing the energy loss per unit length inside the jumps taking into account the elastic energy (this correspond to the green points in Fig. 6.3), to the same energy loss, also calculated from coarse-graining, but without taking into account the elastic energy, as done in Fig. 6.5a. It shows that the elastic energy is always much smaller than the kinetic and gravitational potential energies, and thus, can be neglected. The symbols and colours in Fig. 6.5 designate the different types of jumps investigated as shown in Tab. 6.1. Figure 6.5b demonstrates that the error induced by this assumption is always smaller than 2%. We also see that this error increases with the volume fraction: if the bulk is denser, more spheres will be in contact, and thus the contact forces will be higher and the elastic potential energy can play a role. This also suggests that, if future work aims to include the elastic potential energy in the hydrodynamic depth-averaged energy, further research could focus on the relation between the elastic energy and the depth-averaged volume fraction.

The second assumption can be checked by comparing the energy loss per unit length inside the jumps calculated from the two different methods, coarse-graining or hydrodynamic depth-averaged values. Figure 6.5c shows the loss of hydrodynamic conservative energy inside the jumps E_l^{hydro}, as a function of the loss of the coarse-grained conservative energy inside the jumps E_l. We see that the points are always very close to the black curve $y = x$. This result suggests that the hydrodynamic point of view may be good enough to describe the energy along the incline.

However, if we look more closely, the fitting does not seem so good everywhere. Figure 6.5d shows the ratio of the two energy loss coefficients E_l^{hydro}/E_l, calculated with the two different methods, as a function of the Froude number Fr. It shows that the fitting is centered on one, but the direct hydrodynamic method overestimates the energy loss per unit length for jumps on slope angles below 30° (orange and blue markers), and underestimates the energy loss per unit length inside the jumps for higher slope angles, above 30° (purple markers) or when the friction between the grains is very low below the critical value 0.2 already discussed (red stars). This figure also shows that the error is evolving with the Froude number for low slope angles, and then stabilizes for high slope angles. The error can reach up to 30% for low slope angles. Therefore the hydrodynamic energy from depth-averaged values provides a good first-order approximation, although part of the information is still missing, as the errors can reach up to 30%.

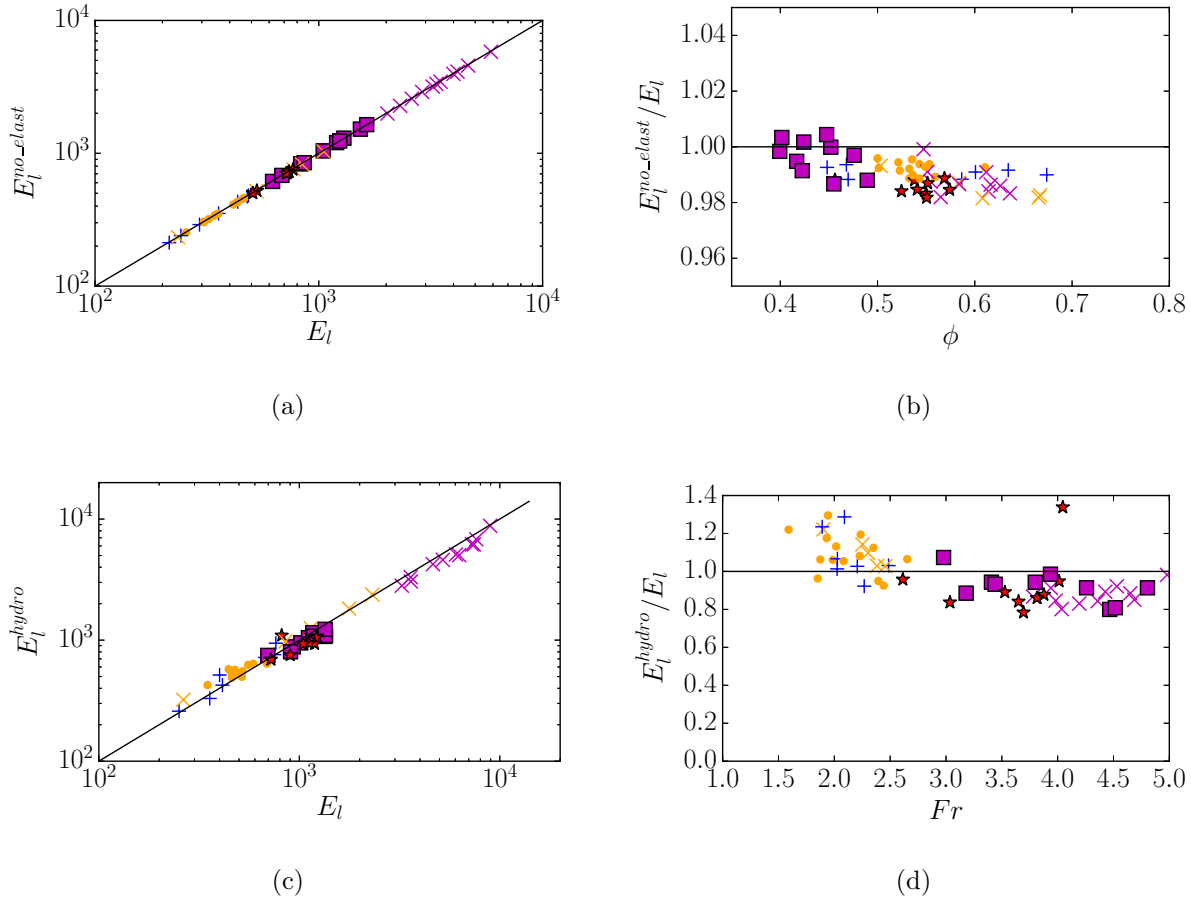

Figure 6.5: Comparison between the energy loss per unit length inside the jumps calculated by taking into account (E_l) or nor ($E_l^{no\_elast}$) the elastic potential energy (panel a); ratio of $E_l^{no_elast}$ over E_l as a function of the depth-averaged volume fraction (panel b); comparison between the energy loss per unit length inside the jumps calculated exactly with coarse-grained values and approximated with hydrodynamic depth-averaged values (panel c); and ratio of E^{hydro} over E_l as a function of the Froude number (panel d). The black lines correspond to the $y = x$ line in panels a and c or to $y = 1$ in panel b and d. The details of the colours and symbols used are described in Tab. 6.1.

6.5 Discussion

It is useful to compare the results in term of energy dissipations, as discussed in the present chapter, to the results of Chap. 5 based on the effective friction inside the jumps derived from mass and momentum equations.

Chapter 5 suggested that the effective friction inside the jump μ_e, the jump length L, and the jump ratio h_*/h are strongly linked to the energy dissipation along the incline and across the jump. In other words, more energy is dissipated for increasing the friction coefficient μ_e, the jump height ratio h_*/h or the jump length L.

The resistive force across the granular jump was expressed in Chap. 2, Eq. (2.4):

$$\tau_b = \mu_e \frac{w}{L} \cos\zeta, \tag{6.8}$$

where μ_e is the effective friction coefficient, which includes all the sources of friction over the jump length; while $w = \frac{1}{2} K_0 g L(\rho h + \rho_* h_*)$ is the weight of the jump, with K_0 being a shape factor. Then, the Coulomb-like stress τ_b has the following form:

$$\tau_b = \frac{1}{2} \mu_e K_0 \rho g h \cos\zeta \left(1 + \frac{\rho_*}{\rho}\frac{h_*}{h}\right). \tag{6.9}$$

Before the jump, the equivalent of the effective friction is exactly equal to the slope angle for steady and uniform flows $\mu^{inflow} = \tan\zeta$. The expression of the resistive force before the jump is then:

$$\tau^{inflow} = \rho g h \sin\zeta. \tag{6.10}$$

Figure 6.6 shows the difference between the resistive force within the jump and the resistive force of the inflow $\tau_b - \tau^{inflow}$ as a function of the energy loss per unit length across the jump E_l. Figure 6.6a has a linear scale, and Fig. 6.6b is the same figure with a log scale in order to highlight the details of the comparison for the low energies. We see that the energy loss per unit length E_l increases linearly with the difference in resistive force between the across and before the jump. Looking at the expression for $\tau_b - \tau^{inflow}$, this suggests that either an increase of h_*/h, μ_e, or ρ_*/ρ will increase the efficiency of the jump to dissipate energy across a short distance. Figure 6.6 also shows that something very different takes place in the case of the hydraulic-like jumps, with a very low friction coefficient μ between grains: the resistive force across the jump τ_b is too small to explain the relatively high efficiency of the jump to dissipate energy. This confirms the hypothesis of Chap. 5 that the roller created in the case of hydraulic-like jumps is able to dissipate energy very efficiently, but cannot be expressed as a Coulomb-like friction through the Eq. (6.8) for τ_b. Future work could focus on developing a more relevant expression of the resistive force for granular jumps with a water-like roller obtained when the interparticle friction is below a critical value of about 0.2. The expression for τ_b in that case should be closer to hydraulic relations based on turbulence concepts. On a more general note, we believe that investigating the granular jumps with a very low friction between grains could help to find an expression for the resistive force across water jumps (see discussion in Chap. 3). We remind here that we were not able to explain the experimental tests on jumps formed in water flows on a rough bottom by using a simple relation for τ_b as a turbulent stress, or to explain the physical meaning of the fitted relation able to reproduce the experimental observations.

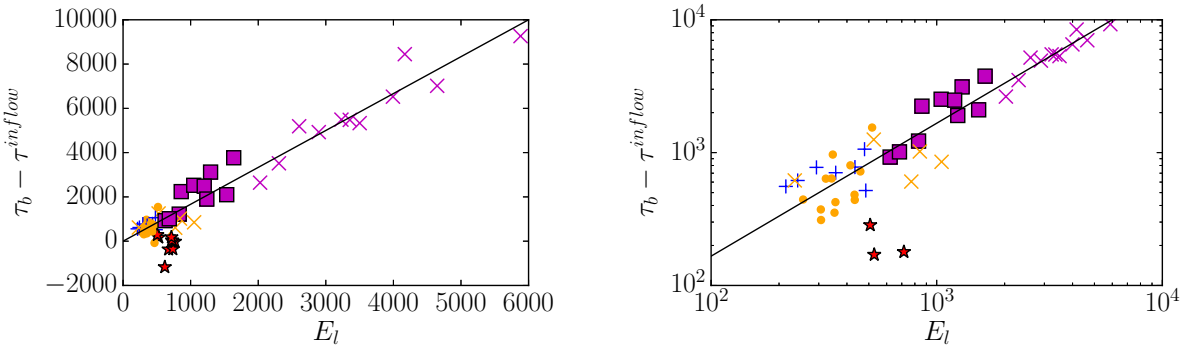

(a) (b)

Figure 6.6: Resistive force across the jump τ_b minus the resistive force in the incoming flow τ^{inflow} as a function of the energy loss per unit length inside the jump E_l. Linear (panel a) and logarithmic (panel b) scales.

6.6 Conclusion

The current chapter presented the results obtained from DEM numerical simulations on the dissipation of energy along the incline, by varying several parameters: the slope angle of the incline, the interparticle friction, the grain diameter and the mass discharge. It was shown that all those parameters have an influence on the energy dissipation along the incline. The conservative energy is mostly composed of the kinetic energy, and the gravitational potential energy. This means that the two parameters that have the more influence on the jumps are the slope angle of the incline, and the flow height h. Specifically, the slope angle increases the velocity (which drives the kinetic energy) and controls the gravitational potential energy (through the height of the base of the incline), while h controls the gravitational potential energy. What happens on the hydraulic-like jumps with a very low friction coefficient μ is a different phenomenon. Perhaps unexpectedly, our analysis of the granular jumps observed for low interparticle friction appears to open a new path to decipher the nature of the resistive force acting within the jump when a roller does appear, which might help to develop a physically-sound expression for τ_b in the case of water jumps (see discussion in Chap. 3).

Furthermore, the elastic potential energy was demonstrated to be negligible in most cases as the error induced by not taking it into account is always lower than 2%. However, we also showed that this error evolves with the depth-averaged volume fraction, thus suggesting that future work on the effect of the elastic energy could focus on a relation between the elastic energy and the volume fraction of the flow.

Finally, future research could also be focused on a full energy equation that would rely on the depth-averaged values. The current equation proposed is already good to a first order, though involves an error that can reach up to 30% depending on the incoming Froude number.

Part III

Experimental study

Chapter 7

X-ray radiography of standing jumps down inclines

Ségolène MEJEAN, François Guillard, Thierry FAUG, Itai EINAV
Article still in progress

To support the numerical study of Part II, a significant element of this thesis work was based on laboratory experiments. All those experiments were done in the School of Civil Engineering at the University of Sydney, using an innovative measurement technique based on X-ray dynamic radiography, described in Sec. 7.1. The rest of the chapter is then divided into two sections. Section 7.2 shows the results of the experiments on standing granular jumps with spherical glass beads, including the incoming flows, the jump region, and the identification of several jump types thanks to the measurement of the volume fraction fields. Finally, Sec. 7.3 focuses on jumps with elongated particles, where the particles change their orientation, thus creating a new type of granular jumps.

7.1 Experimental set-up and procedure

The experimental set-up to produce standing granular jumps is the same as the one used in [19], but adapted to allow internal measurements of material properties using dynamic X-ray radiography, combined with innovative image analysis method (as done in [28]).

The DynamiX laboratory in Sydney is organized around two rooms: the control room, and the X-ray room, where the experiments are set-up (Fig. 7.1a), which is shielded against X-ray leakage with thick lead-lined walls (to protect users who operate the equipment from the separate control room).

A sketch of the experimental granular jump device is shown in Fig. 7.1b. It is made of a reservoir full of grains (inclined at a slope of 16°), feeding a granular chute of adjustable slope ζ independent of the reservoir inclination, which is 1m long, 0.1m wide, and 0.15m high. Between the tank and the chute, an opening of adjustable height H controls the discharge. A gate just after the opening allows to release the granular material from the reservoir, at a chosen time. As it needs to be opened at the beginning of the experiment, it is closed with an electromagnet that can be disabled from the control room thanks to an electronic relay, with a spring device driving the opening of the gate after release.

At the end of the chute, a second gate is initially closed and its height from the bottom of the chute can be adjusted during the experiment with a remotely controlled translation stage. Opening this gate will allow to control the discharge after the jump. If it is higher than the incoming discharge, the jump will move upstream, if it is lower, the jump will move downstream. A steady state is generally reached if the discharge after the jump is the same as the discharge of the incoming flow. The height of this gate is then tuned from the control room, out of the X-ray room such that the steady granular jump will be placed at the desired location where the X-ray beam are intended to pass.

The X-ray device, as shown in Fig. 7.1, is composed of a source emitting X-rays perpendicularly to the interesting part of the chute, where the jump will be set stationary, and a detector on the other side of the chute, which measures the intensity of the X-rays

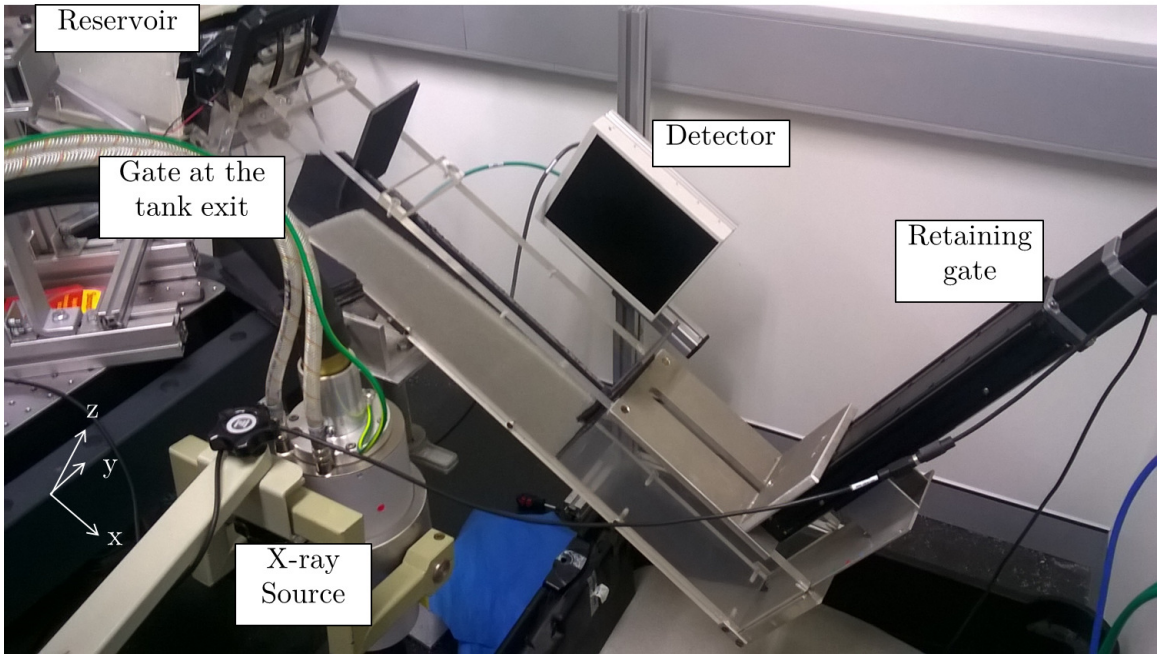

(a)

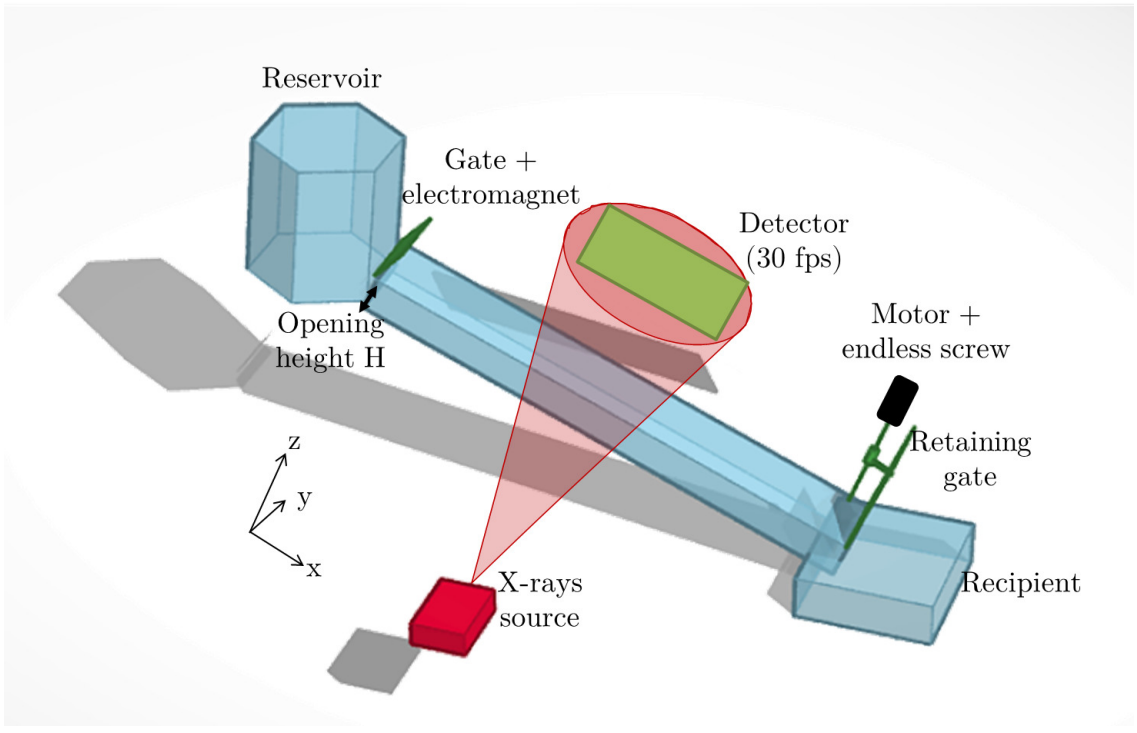

(b)

Figure 7.1: Experimental granular jump device in the X-ray room. (a) Picture of the device during a calibration test. (b) Commented sketch of the same device. This is the same device as used in [19], shown in Sec. 1, Fig. 1.8, only adapted to X-ray measurements.

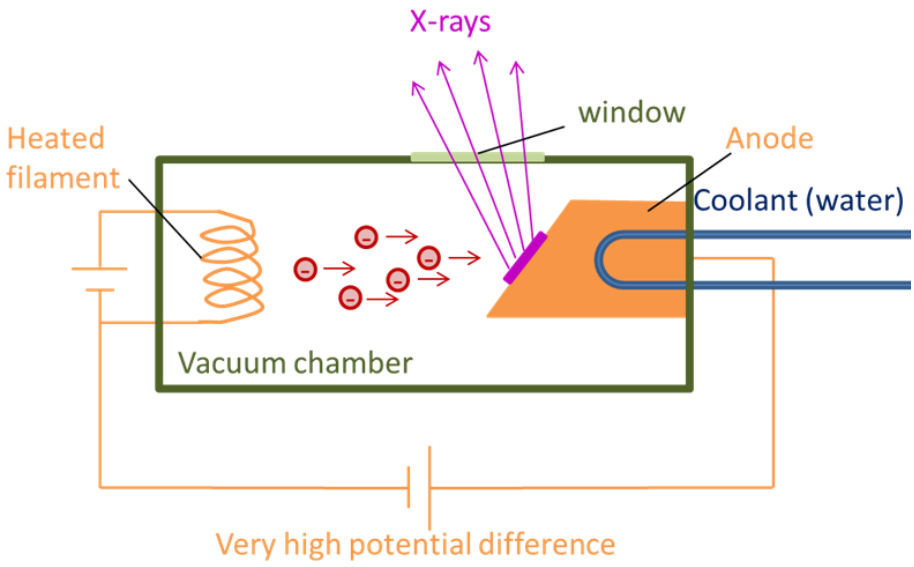

Figure 7.2: Sketch of a X-ray tube.

after having crossed the flume and the granular media inside, at a frequency of 30 frames per second.

The source, an X-ray tube depicted in Fig. 7.2, is producing X-rays thanks to charged particles (electrons) of sufficient energy hitting target material in Tungsten (anode). A very high potential difference accelerates the electrons released by a heated filament (cathode). When those electrons hit the anode, X-rays are created and escape the tube through a window to irradiate the experiment. The anode is permanently cooled by circulating water.

The detector measures the intensity in every pixel (960 pixels along the x-axis that follows the channel slope angle, and 768 pixels along the z-axis, perpendicular to the x-axis), and convert it into a number between 0 and 65535. An example of this image in gray level at a given time t is given in Fig. 7.3 for a jump made of glass beads (Fig. 7.3a) and a jump made of rice grains (Fig. 7.3b). The particles are flowing from left to right. From those images, some work is done to correct the difference of inclination between the detector and the channel.

The measured intensity on a given pixel at location (x, z) of the detector is the following:

$$I(x,z) = I_0 \exp\left(\int_l -\mu_{att}\rho_m(x,z,l)dl\right) \tag{7.1}$$

where I_0 is the intensity of the source, l the ray path inside the medium, μ_{att} the attenuation coefficient and $\rho_m(x,z,l)$ the density of the medium crossed by the ray that reaches the detector at point (x,z) averaged over the path l of the ray. The medium that is crossed by the ray is either the channel walls or the flow of particles we are interested in. Equation (7.1) can then be written:

$$I(x,z) = I_0 \exp\left(-\mu_{att}\left(\rho_{cw}2e + \rho_p\phi(x,z)W\right)\right) \tag{7.2}$$

with e the width of one wall of the channel, ρ_{cw} the density of the channel walls, ρ_p the density of a glass bead, ϕ the volume fraction of the flow crossed by the ray that will reach the detector at point (x,z), and W the width of the channel.

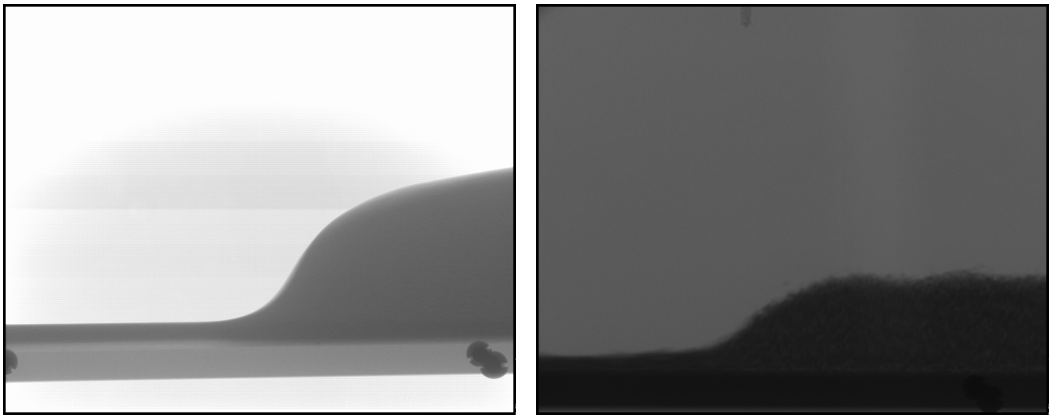

(a) (b)

Figure 7.3: Raw intensity measured by the detector converted in gray level for a jump made of glass beads (panel a) and a jump made of rice (panel b).

In order to get rid of the density of the empty channel, the calibration phase consists of measuring the intensity of the empty channel at every point (x, z) of the detector $\hat{I}_0 = I_0 \exp(-\mu_{att}\rho_{cw}2e)$. We divide, for each point (x, z) in the detector, the measured intensity by the intensity of the the empty chute $\hat{I}_0$, to obtain:

$$\frac{I(x,z)}{\hat{I}_0(x,z)} = \exp(-\mu_{att}\rho_p\phi(x,z)W) \tag{7.3}$$

We can therefore express directly the volume fraction of the granular medium at location (x, z) directly from:

$$\phi(x,z) = -c\ \ln\left(\frac{I(x,z)}{\hat{I}_0(x,z)}\right) \tag{7.4}$$

where $c = 1/(\mu_{att}\rho_p W)$ is a constant. Because of the term μ_{att} in this constant, c is not known and should be determined experimentally. The volume fraction ϕ is linear with $-\ln\left(I/\hat{I}_0\right)$, meaning that the plot of ϕ versus $-\ln\left(I/\hat{I}_0\right)$ is a straight line crossing zero with c the slope. The intensity $\hat{I}_f$ of the channel full of particles at the random close packing is also measured at every point (x, z) of the detector. This random close packing is also measured carefully as the mass of the particles times the density of one particle divided by the volume of the particles at the random close packing. In the case of spherical glass beads, the random close packing was equal to 0.62. In the case of rice grains, the calibration was done in two points, the random close packing measured to be equal to 0.506, and the volume fraction of the grains when they are oriented, equal to 0.602. This calibration process measuring $\hat{I}_0$ and $\hat{I}_f$ allows to establish the coefficient c is Eq. (7.4). Applying Eq. (7.4) to every point x, z of the reservoir yields a complete width-averaged field of volume fraction of the flow between the X-ray source and the detector, where the jump is located.

The X-ray measurement technique could also be a good way to measure a width-averaged velocity, for example *via* Particle Image Velocimetry (PIV). However, in the present tests on jumps down inclines, the velocity reaches high values typically of 0.5 to 1m.s^{-1}. The acquisition rate of the detector, 30 frames per second, was not high enough to obtain satisfying results with PIV. In order to measure directly the velocity, we need a detector with a quicker acquisition rate. However, as demonstrated in Sec. 7.2.2 an

Particles	$\zeta[^\circ]$	H[mm]
Spherical glass beads	$25-30-35-40$	$15-20-25-30-35$
Elongated rice	$30-35-40$	$20-30-35$

Table 7.1: Experimental parameters of this study.

alternative approach was developed to extract the depth-averaged velocity using mass conservation.

This experimental design allows to vary the slope ζ and the discharge through the opening height of the reservoir exit H. Two types of particles were studied: spherical glass beads and elongated rice. Table 7.1 summarizes how ζ and H were varied for each type of granular material in the present experiments.

7.2 Granular jumps with spherical grains

In the first set of experiments, we used glass beads with an average diameter of $d = 1.2$mm. The glass beads have a particle density of $\rho_p = 2500$kg m^3, and they are spherical.

7.2.1 Density fields

In our 2D numerical study using Discrete Element Method on granular jumps down smooth inclines [45], we evidenced the existence of several types of jumps depending on the slope angle and the discharge:

- For low slope angles, the streamlines are increasing smoothly inside the jump from the thickness before to the thickness after the jump. Looking at the depth-averaged volume fraction, we observe the same smooth transition inside the jump. We called them laminar granular jumps.

- For higher slope angles, the streamlines inside the jump are not so smooth anymore, and a recirculation pattern forms close to the free-surface. This is evidenced using the plots of depth-averaged volume fraction along the channel. The volume fraction begins to rise, then we observe a drop in the middle of the increase, and the volume fraction rises again to reach the volume fraction after the jump (close to the maximum packing fraction). They were called steep colliding granular jumps.

A wide range of slope angles and discharges have been tested in the present experiments. The volume fraction fields and the corresponding depth-averaged volume fraction graphs as a function of the position on the channel, for all experiments, are shown in Fig. 7.4.

The phase diagram obtained is consistent with the one obtained by the two-dimensional numerical simulations using the discrete element method [45]. Fig. 7.4 shows that the jumps are more and more compressible when the discharge (relating to the opening height of the reservoir H) is decreasing. This means that the difference in volume fraction before and after the jump is much higher on the graphs on the left (low H, and then low discharge). The steepness of the jumps, increasing strongly with the slope, is also noticeable in this graph. The thickness difference of the jump before and after the jump is higher at high slopes (bottom of the graph).

In [45], the streamlines showed that a recirculating zone appeared for jumps at high slopes. This was highlighted by a drop in the depth-averaged volume fraction plotted as

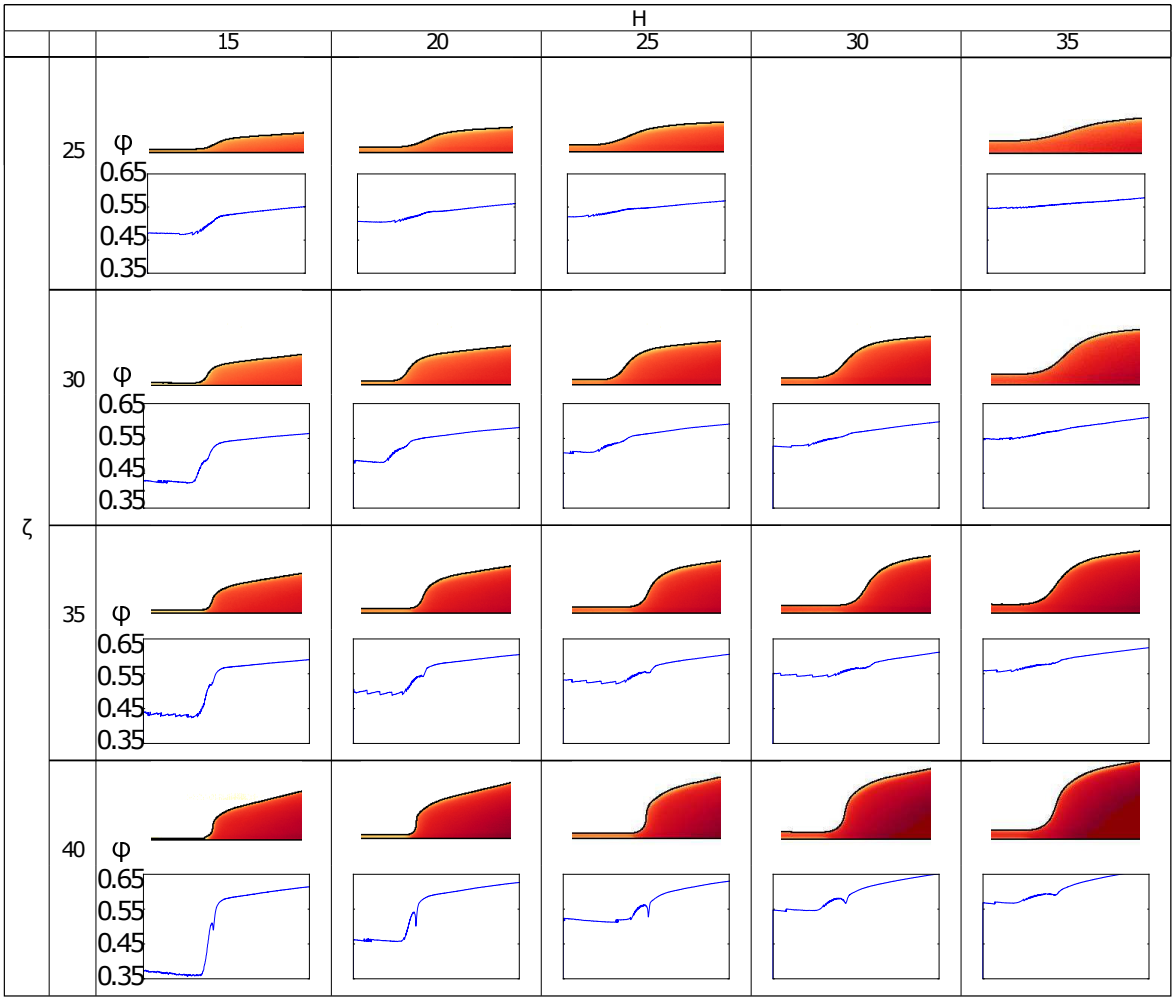

Figure 7.4: Transition from a laminar granular jump to a steep colliding granular jump. Density fields and depth-averaged volume fraction for different H/d and ζ presented in table 7.1.

a function of the position along the flume. This drop is present in Fig. 7.4 in all jumps at a slope angle of 40°, and seems close to appear in the 35° slope angle tests. This validates the existence of several types of jumps, as first observed using DEM simulations but here experimentally, with a recirculation developing at the highest slopes.

7.2.2 Macroscopic properties of jumps

In the experiments on the jumps by [19] using the same granular chute, the macroscopic properties of the jumps were measured with a high-speed camera placed on one side of the chute. However, any experiment with side walls have boundary effects, and the high speed camera measured only the perturbed part of the bulk along the walls. This perturbed flow is a little bit thinner and slower than in the middle of the chute. The new technique based on X-rays dynamic radiography presents big improvements compared to the high speed camera looking at the side walls. It allows to integrate the entire with of the channel, to finally obtain width-averaged values. In addition, the X-rays method helps us to extract a clean volume fraction field in every pixel of the detector, which was not possible to measure with the previous optical measurement techniques.

In the following, the incoming flows (before the jumps) and then the jumps are analysed.

Incoming flows

The incoming flow is the part of the flow between the reservoir exit and the beginning of the jump region. This flow is supercritical which implies that it is influenced only by what happens before it. This classical configuration of a flow of glass beads down a slope on a smooth base have been studied for example by [42], [71]. The X-rays allow to measure the variables in a width averaged point of view, which is not common in experimental studies.

The experimental set up allowed to vary the slope ζ of the chute, and the gate opening at the tank exit H. This height H is controlling the discharge q [m^3 s^{-1}] of the grains running from the reservoir to the chute.

Figure 7.5 shows the dimensionless thickness h/d and the depth-averaged volume fraction ϕ of the incoming flow, as a function of the slope angle ζ and the gate opening at the tank exit H/d. The colour and the shape of the markers on this figure are used consistently for all the other figures of this chapter : a change in the slope angle corresponds to a change in the markers shape (stars $\zeta = 20°$, circles $\zeta = 25°$, pentagons $\zeta = 30°$, and triangles $\zeta = 35°$); and a change in the markers colour corresponds to a change in the opening of the tank exit (blue $H = 15$mm, red $H = 20$mm, green $H = 25$mm, purple $H = 30$mm, and yellow $H = 35$mm).

Figure 7.5a shows a linear increase of the dimensionless flow thickness h/d with increasing discharge represented by the gate opening at the tank exit H/d. This increase of the discharge also makes the flow denser (see Fig. 7.5c) until it reaches a maximum volume fraction for the incoming flow (which is a supercritical rapid and thin flow), around $\phi = 0.55$. When this maximum flowing volume fraction is reached, around $H/d = 18$mm, the volume fraction remains constant whatever the discharge or the slope angle. Figure 7.5d confirms the existence of a critical discharge q_c below which the volume fraction falls below 0.55. It also shows that, for lower discharges, the volume fraction is decreasing when the slope angle is increasing. This is the influence of the gravity, more important on the steepest slope angles which brings more velocity to the grains and increases their free

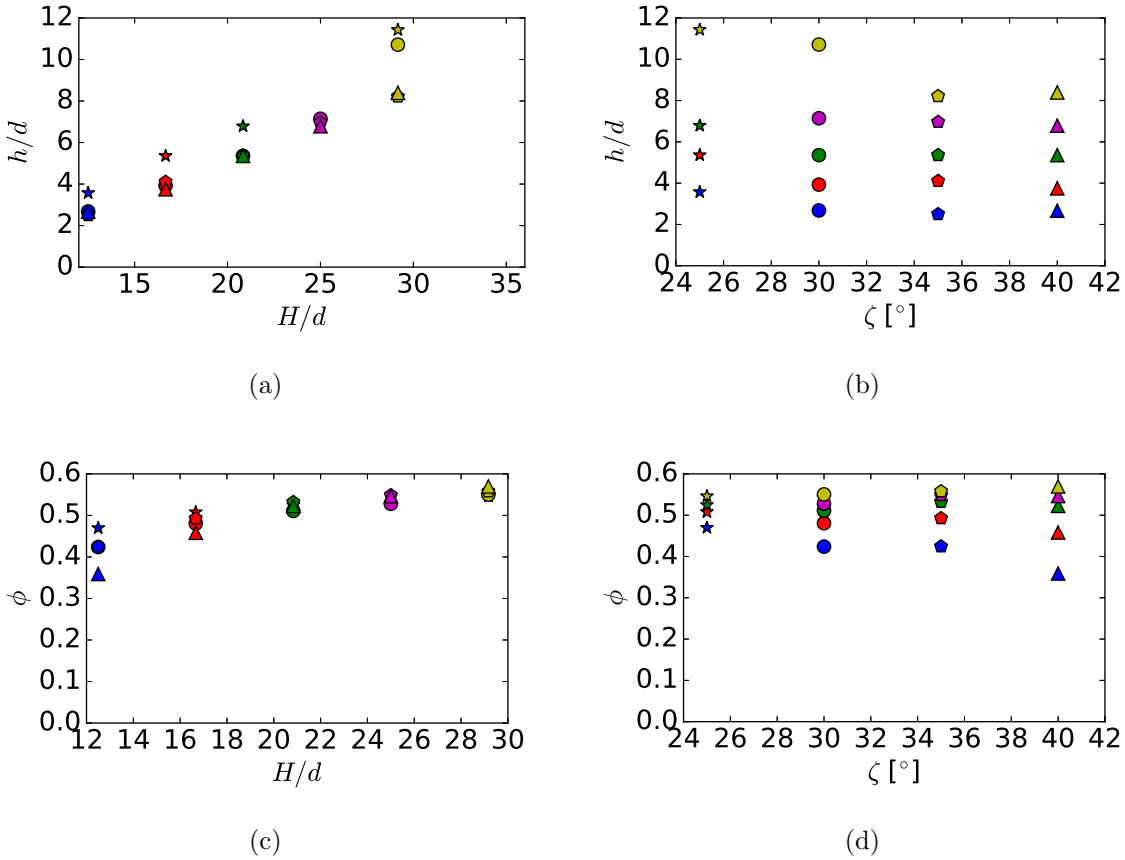

Figure 7.5: Dimensionless thickness h/d (top) and volume fraction ϕ (bottom) of the incoming flows, as a function of the slope angle ζ (right) and the gate opening at the tank exit H/d (left). Marker shapes: stars $\zeta = 20°$, circles $\zeta = 25°$, pentagons $\zeta = 30°$, triangles $\zeta = 35°$. Marker colours: blue $H = 15$mm, red $H = 20$mm, green $H = 25$mm, purple $H = 30$mm, and yellow $H = 35$mm.

mean path, thus decreases the volume fraction. This can be seen as a signature to the dense to dilute transition in granular flows, also known as liquid to gas transition [20].

Figure 7.5b suggests that the slope angle has almost no influence on the thickness of the flow, except for very low slope angles (star markers in Figs. 7.5b and 7.5a): the thickness of the flow is increasing when the slope is low and reaches a constant value for higher slopes. At low slope angles, the grain-grain and grain-wall friction effects are strong compared to gravity, allowing a slight increase of the thickness. When the gravity effects become stronger, the slope angle does not have an influence on the thickness anymore.

The previous graphs do not include a parameter able to describe the dynamics of the flow. To this purpose, we need the velocity of the flow, which could not be measured directly in the present experiments because of the acquisition rate of the detector, which was too slow compared to the velocity of the flows. However, we have access to a calculated depth-averaged velocity. Mass conservation equation says that the discharge is independent from the position x along the channel, which means that the discharge at the reservoir exit is the same everywhere:

$$\phi(x)h(x)\bar{u}(x)W = q_0. \tag{7.5}$$

As explained before, the discharge of the incoming flow is controlled by H, the opening at the exit of the reservoir. The relation between ζ, H and q can be addressed thanks to the Beverloo law:

$$q_0 = \alpha\phi_\infty\sqrt{gH\sin\zeta}HW \tag{7.6}$$

with α a coefficient which was measured to be equal to 0.72 in the experiments of [19] with glass beads on the same granular chute, ϕ_∞ the theoretical maximum packing fraction of the grains, which is equal for the present grains to 0.64 in three dimensions, and W the width of the channel.

Combining Eq.(7.5) with Eq. (7.6), we have:

$$\phi(x)h(x)\bar{u}(x)W = \alpha\phi_\infty\sqrt{g\sin\zeta}H^{3/2}W. \tag{7.7}$$

Next, knowing the depth-averaged volume fraction and thickness of the flow at any position x , it is possible to get the depth-averaged velocity averaged across the chute width at any location x:

$$\bar{u}(x) = \frac{\alpha\phi_\infty\sqrt{g\sin\zeta}H^{3/2}}{\phi(x)h(x)}. \tag{7.8}$$

Thanks to this calculated depth-averaged velocity, we therefore have experimental access to the Froude number,

$$Fr(x) = \frac{\bar{u}(x)}{\sqrt{gh(x)\cos\zeta}}, \tag{7.9}$$

which is the ratio between the flow velocity and the maximum velocity of free-surface gravity waves. This number describes the dynamics of a flow. A thin fast flow, which has a Froude number higher than 1, is influenced only by what happens upstream, and is called supercritical. A thick slow flow, with a Froude number lower than 1 is influenced only by what happens downstream and is called subcritical. A jump is the fast transition that takes place when a supercritical flow becomes subcritical.

Figure 7.6 shows the Froude numbers of the incoming flows as a function of the discharge H/d and the slope angle ζ. Figure 7.6a shows that the Froude number is decreasing

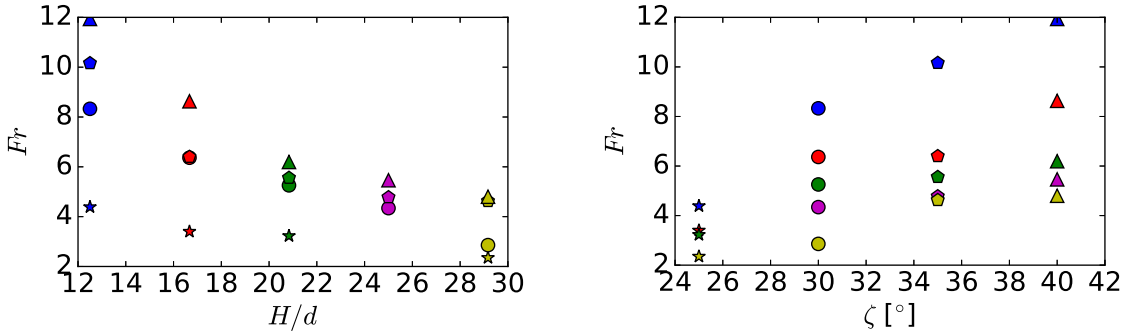

(a) (b)

Figure 7.6: Froude number Fr of the incoming flows as a function of the discharge H/d (a) and the slope angle ζ (b). Marker shapes: stars $\zeta = 20°$, circles $\zeta = 25°$, pentagons $\zeta = 30°$, triangles $\zeta = 35°$. Marker colours: blue $H = 15$mm, red $H = 20$mm, green $H = 25$mm, purple $H = 30$mm, and yellow $H = 35$mm.

when the discharge is increasing. This is due to the corresponding increase of the thickness of the flow (Fig. 7.5a). In the same way, Fig. 7.6b shows that the Froude number increases with the slope angle of the chute, as this slope strongly controls the velocity of the grains. Blue markers in Figs. 7.6b or 7.6a correspond to the lowest discharge. For those grains, the volume fraction is particularly low (see fig. 7.5c), and then, the free mean path of every particle is higher. This is compensated by a noticeable increase of the velocity, and hence, of the Froude number.

Jumps

In order to compare the evolution of the flow properties before and after the jumps, it is necessary to precisely define the beginning and the end or the jump region. In [19] and [44], the beginning and the end of the jumps were defined using the free-surface shape. The beginning of the jump was the point at which the free-surface started to rise and was not parallel anymore to the bottom, and the end of the jump was the point where the free-surface curve reached a constant angle with the horizontal axis. However, as shown in [45], the depth-averaged velocity is a better measure for determining the jump region. Indeed, the change of velocity sometimes occurs while no change is detectable in the free-surface. Moreover, this length is very close to the one which may be determined "by eyes" with the depth-averaged volume fraction. In this study, the depth-averaged velocity is not directly accessible. The jumps region was therefore determined with both the volume fraction and the free-surface, so that any part of the flow where one of those curves was varying greatly was considered to be inside the jump.

Figure 7.7 shows the relative height of the jump h_*/h, the relative volume fraction of the jump ϕ_*/ϕ, and the jump length L as a function of the discharge H/d and the slope ζ. Both the discharge (Fig. 7.7a) and the slope (Fig. 7.7b) have an influence on the relative height h_*/h. We see that the highest h_*/h, (highest difference between the incoming and outgoing thicknesses) takes place for high slope angles and low discharges. At the same time, we see in Fig. 7.7c and 7.7d that higher thickness difference is well correlated with a higher compressibility (high ϕ_*/ϕ). The compressibility of the jump is highly linked to the volume fraction of its incoming flow, as the volume fraction after the jump does not vary very much, remaining close to the maximum packing fraction. The jump length is

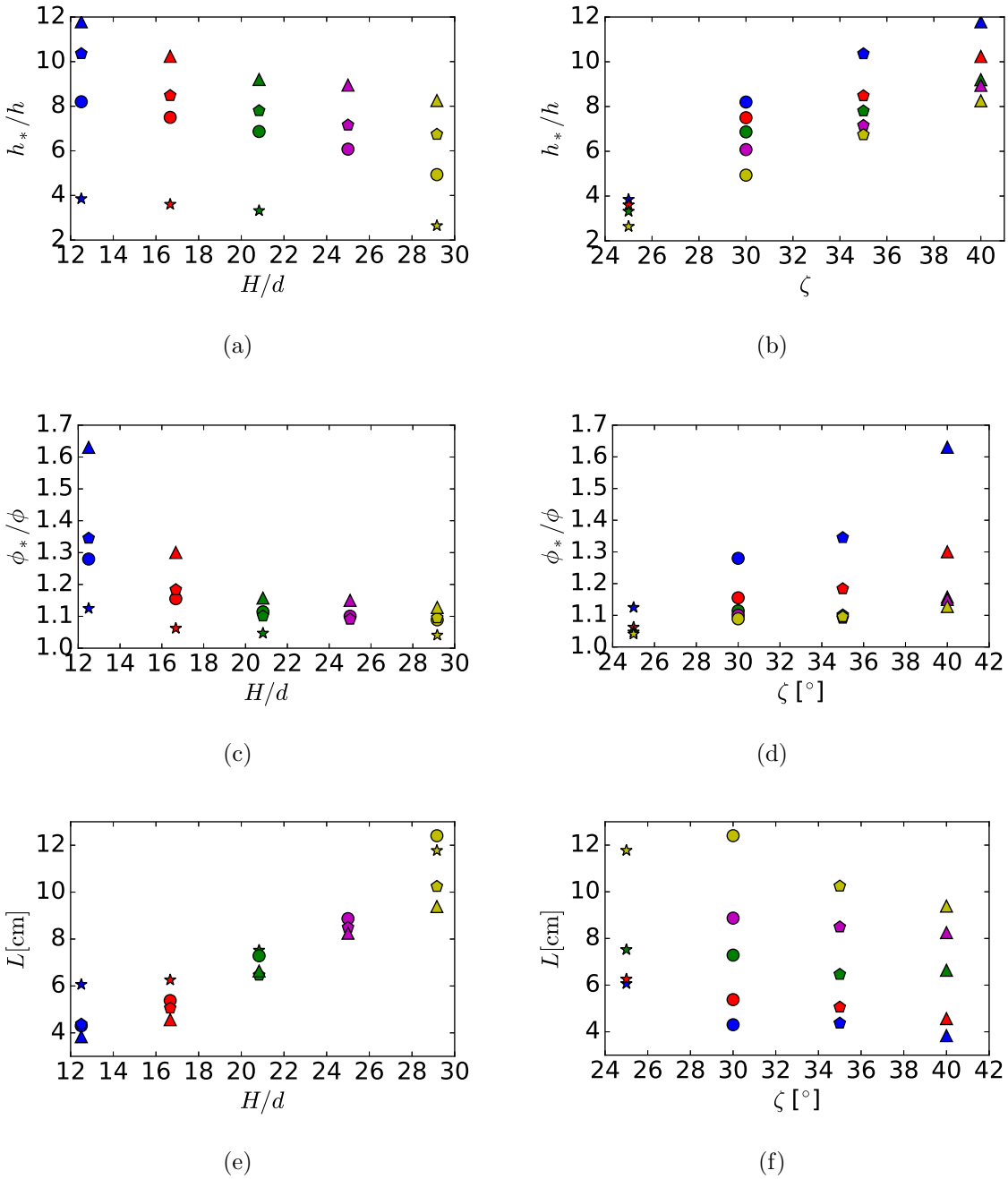

Figure 7.7: Effects of H/d (left) and ζ (right) on the jump height ratio h_*/h (a,b), the volume fraction ratio ϕ_*/ϕ (c,d), and the length of the jumps L (e,f). Marker shapes: stars $\zeta = 20°$, circles $\zeta = 25°$, pentagons $\zeta = 30°$, triangles $\zeta = 35°$. Marker colours: blue $H = 15$mm, red $H = 20$mm, green $H = 25$mm, purple $H = 30$mm, and yellow $H = 35$mm.

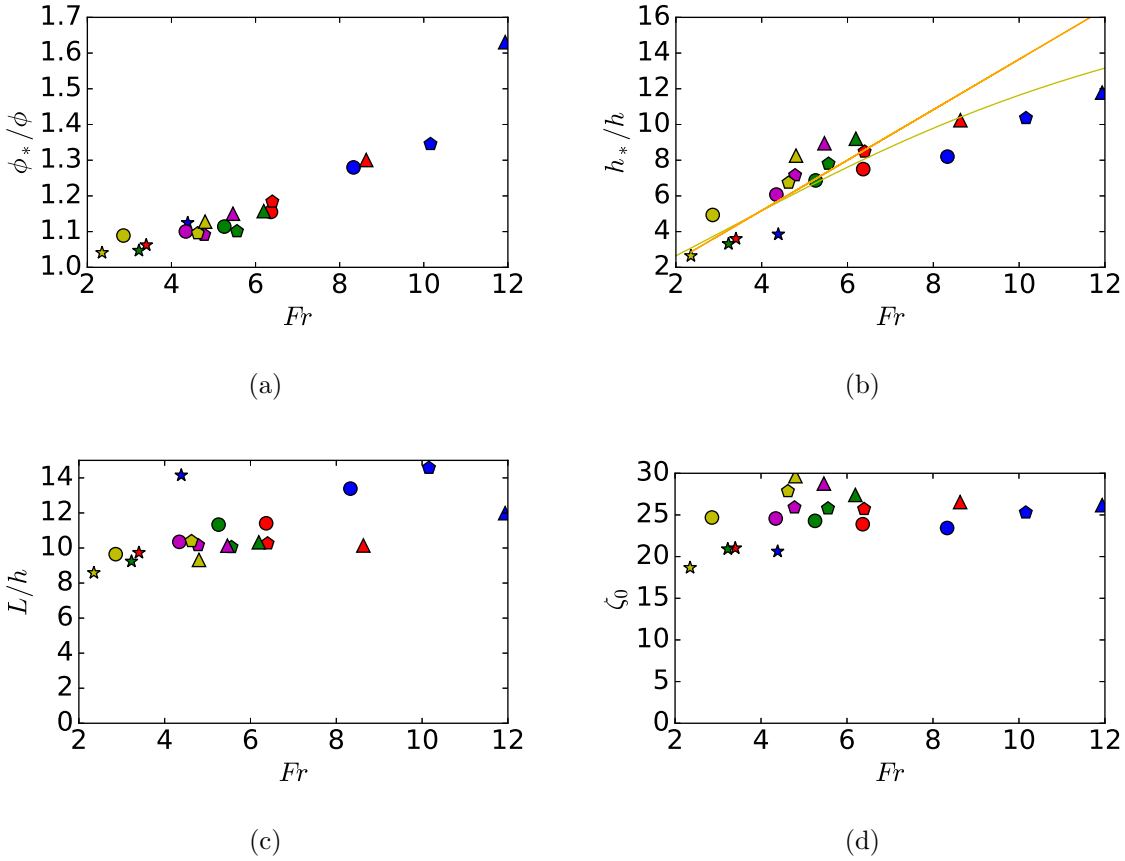

Figure 7.8: The dependence of ϕ_*/ϕ (panel a), h_*/h (panel b), L/h (panel c), and ζ_0 (panel d) on the Froude number. In panel b, Bélanger's equation (7.6) is shown by the continuous orange line, while a correction of Bélanger's equation taking into account the change in volume fraction across the jump is represented by the yellow continuous line. Marker shapes: stars $\zeta = 20°$, circles $\zeta = 25°$, pentagons $\zeta = 30°$, triangles $\zeta = 35°$. Marker colours: blue $H = 15$mm, red $H = 20$mm, green $H = 25$mm, purple $H = 30$mm, and yellow $H = 35$mm.

following an invert trend (Fig. 7.7e and 7.7f): it increases with H/d while the jump height ratio and the compressibility are decreasing, and it decreases with the slope angle, while the height ratio and the compressibility are increasing. We obtain the steepest jumps at high discharges and low slope angles.

Those ratios comparing the flows before and after the jumps can be collapsed together by considering the Froude number of the incoming flow (Fig. 7.8).

The relative volume fraction of the jump is a linear function of the Froude number, as shown in Fig. 7.8a. The volume fraction after the jump ϕ_* is increasing slightly with the slope angle and the discharge, but it is always close to the random close packing fraction of the present glass beads: most of the changes in the ratio of packing fractions comes from the incoming flow. We can conclude that the higher the Froude number, the higher the compressibility of the flow, whereas the flow is almost incompressible for very low Froude numbers (ϕ_*/ϕ close to 1).

Figure 7.8b shows the relative thickness of the jumps h_*/h as a function of the Froude number. The orange line is showing the relative thickness according to Bélanger's equa-

tion, which is valid for jump of a hydraulic frictionless fluid on a smooth flat base [44, 45]:

$$\frac{h_*}{h} = \sqrt{1 + 8Fr^2} - 1. \tag{7.10}$$

Although the data is scattered, we can see that the points are following Bélanger's equation relatively well for low Froude numbers, and are below the curve for high Froude numbers. The points below the curve at high Froude numbers correspond to the lowest discharges (red and blue points). As seen in Fig.7.8a, they correspond to highly compressible jumps. Faug et al. [19] proposed an equation that improved Bélanger's equation by taking into account the compressibility of the jumps through the volume fraction ratio $\frac{\rho_*}{\rho}$:

$$2Fr^2 \left(1 - \frac{1}{\frac{\rho_*}{\rho}\frac{h_*}{h}}\right) = \frac{\rho_*}{\rho}\left(\frac{h_*}{h}\right)^2 - 1. \tag{7.11}$$

This equation is used to plot the yellow line in Fig. 7.8b. We can see that the yellow line follows much better the data points at high Froude numbers, under the prediction of Bélanger's equation. We can conclude that the jumps with a low incoming volume fraction, which are most compressible, will first densify before thicken, thus leading to a lower jump height ratio h_*/h. For lower Froude numbers, where the compressibility is lower and does not have a strong effect anymore, we expected the Bélanger's equation to underestimate the jump height ratio, as observed in our previous study of 2D-DEM simulations of granular jumps [45]. It seems to be the case for some values, but the scattering seems to be too significant to be able to conclude. In particular, the data points corresponding to the lowest slope (star markers) are systematically under the prediction of Bélanger's equation (orange curve). The main technical issue that can explain the large scattering is the difficulty to detect the bottom of the chute, that can lead to an error in the flow thickness h, and then, the error propagates and is amplified in the calculation of the Froude number from mass conservation (Eq. (7.8)). Another limitation is that while the reservoir was emptying and its weight was changing during the experiment, the slope angle was slightly evolving, and thus the position of the bottom of the flume on the detector. It would be necessary to correct this issue in order to be able to conclude on the extent of comparison to the Bélanger's prediction at low Froude numbers.

If the jump length L is divided by the incoming flow thickness h, it becomes almost constant whatever the Froude number (see Fig. 7.8c). It is always close to ~ 10 for any Froude number. Only one exception is noticeable for very low discharges (blue markers). They correspond to discharges significantly lower than the critical discharge q_c, previously evidenced by investigating the incoming flows (Fig. 7.5c). The different behaviour of the jumps with a very low discharge was also observed in Fig. 7.8b, where the points of the lowest discharge (blue points) are always significantly under the predictions for any Froude number, even when including the compressibility in the predictions (yellow line).

The limit angle ζ_0, between the curve describing the free-surface after the jump and the horizontal axis, is a signature of the effective friction between the grains, and no jump can be created under the minimum ζ_0. Figure 7.8d suggests that this angle is not constant, as previously considered by [19], but evolves with the slope angle and the discharge. In this figure, no general trend is collapsing the points together, but the analysis of the shape and the colour of the markers shows that this limit angle ζ_0 increases both with the discharge and the slope angle. However, this limit angle is situated in the subcritical flow, after the jump. The correlation should then be searched with the outgoing Froude number, $Fr_* = u_*/\sqrt{gh_* \cos\zeta}$. Figure 7.9 shows a clear correlation between ζ_0 and Fr_*,

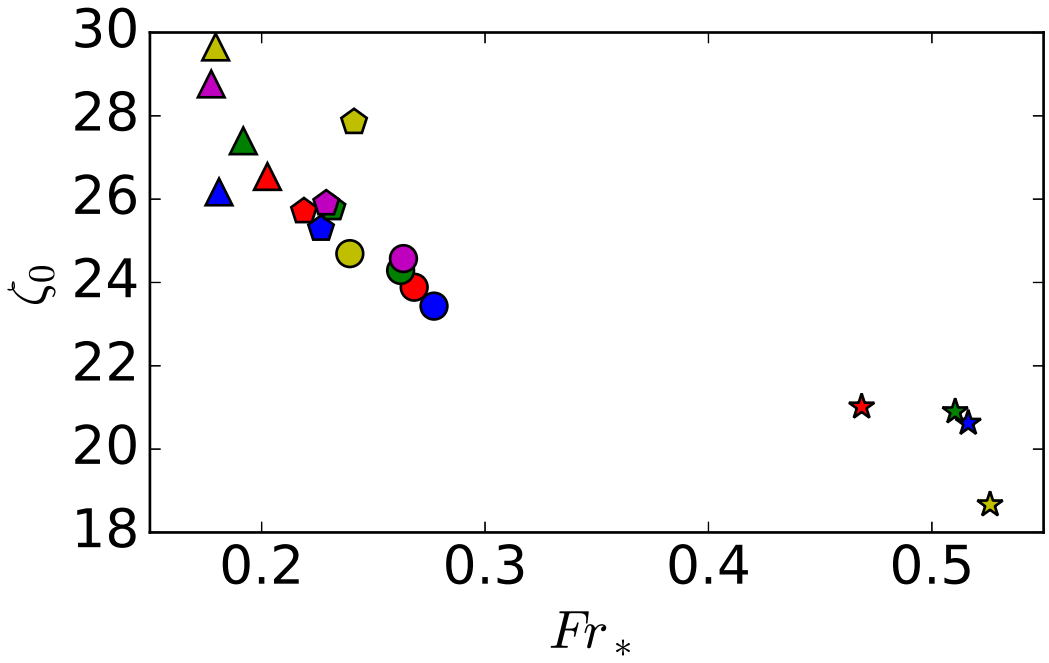

Figure 7.9: Friction slope angle of the outgoing flow ζ_0 as a function of the subcritical Froude number in the outgoing flow. Marker shapes: stars $\zeta = 20°$, circles $\zeta = 25°$, pentagons $\zeta = 30°$, triangles $\zeta = 35°$. Marker colours: blue $H = 15$mm, red $H = 20$mm, green $H = 25$mm, purple $H = 30$mm, and yellow $H = 35$mm.

with all the points collapsing: the lower the outgoing Froude number, the higher the limit angle. This means that slow and thick flows are more frictional, allowing the outgoing flow to keep a large angle between its free surface and the horizontal axis, up to $\zeta_0 = 30°$. The limit angle ζ_0 is related to the derivative of the thickness of the flow after the jump, and thus should be related to the earth pressure coefficient after the jump k_* addressed in [44]. Figure 7.9 suggests that this coefficient k_* is different than 1, and evolves with the slope angle of the channel. Future work could focus on a relation between k_* and the Froude number of the outgoing flow.

7.3 Jumps with elongated grains

In the following set of experiments, the effects of the shape of the grains was explored to identify the interaction between particle alignment and flow. We used elongated grains of rice with an ellipsoid shape. Their longest length was on average $L_r = 7$mm, and the shorter length was $l_r = 2$mm, giving an aspect ratio of about $L_r/l_r = 3.5$. The particle density of this rice was measured to be equal to $\rho_r = 1469$kg m^{-3}.

In the case of the rice, and in order to keep the information of the orientation of the particles, we improved the quality of the images extracted from the detector by putting a shutter between the source of the X-rays and the flume, as shown in Fig. 7.10. This was a thick wheel made of steel (to absorb the X-rays) with two holes inside, turning at half the velocity of the acquisition rate of the detector (15 rotations per second). The X-rays are reaching the detector only when they face the holes, thus avoiding the motion blur that can appear in the images. However, the smallest difference between the acquisition

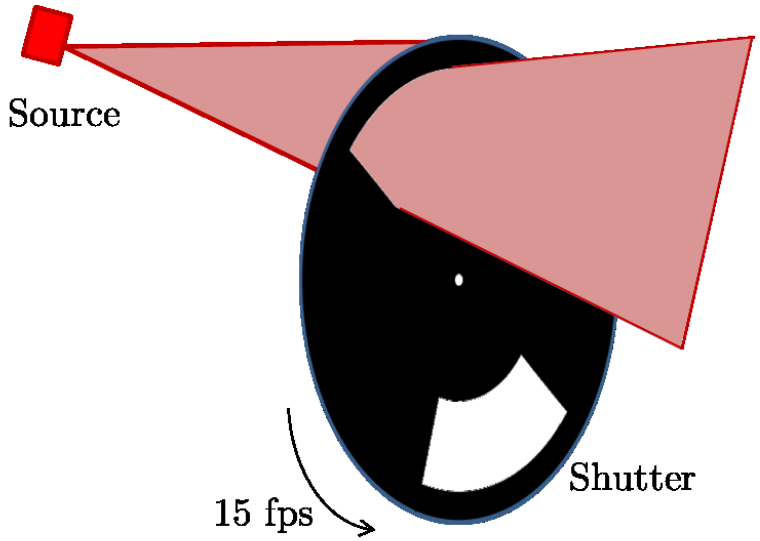

Figure 7.10: Sketch of the shutter: a thick wheel made of steel rotating at half the velocity of the acquisition rate of the detector was settled to improve the quality of the images.

rate of the detector and the rotating velocity of the wheel creates an artefact in the detection. This makes the density field nearly impossible to be measured quantitatively in this configuration. However, many differences between spherical and elongated grains are still visible for effective analysis.

7.3.1 Similarities and differences between spherical and elongated grains

The phase diagram of the experiments with the rice, obtained by varying the slope angle and the discharge is shown in Fig. 7.11. Some similarities with the phase diagram of the glass beads (Fig. 7.4) and with the two-dimensional numerical simulations [45] can be noticed. The steepness of the jumps is increasing with the slope angle.

However, a fundamental difference is seen on the downstream part of the jumps. While the free-surface of the jumps made of glass beads keeps a constant limit angle with the horizontal ζ_0 which is larger than zero and lower than the slope angle of the bottom, this angle, in the case of a jump made of rice grains, is always equal to the slope angle of the chute bottom. This fundamental difference is responsible for the observation of a new type of granular jump, which was not observed with glass beads, as explained in the following.

7.3.2 The role of the grain alignment

Figure 7.12 shows a qualitative density field of a jump with elongated particles at a given time (and not averaged over time like in Fig. 7.4). Thanks to the shutter, the image is clear enough to see the orientation of the grains. In the incoming flow while they are fast, the grains are aligned with the bottom of the chute. This is consistent with previous work showing that elongated particles get oriented in shear flow [11]. Nagy et al. [47] showed that particles with a big aspect ratio (> 3) are oriented in the direction of the streamlines.

But when the grains hit the final gate, they are aligning with the gate, which is

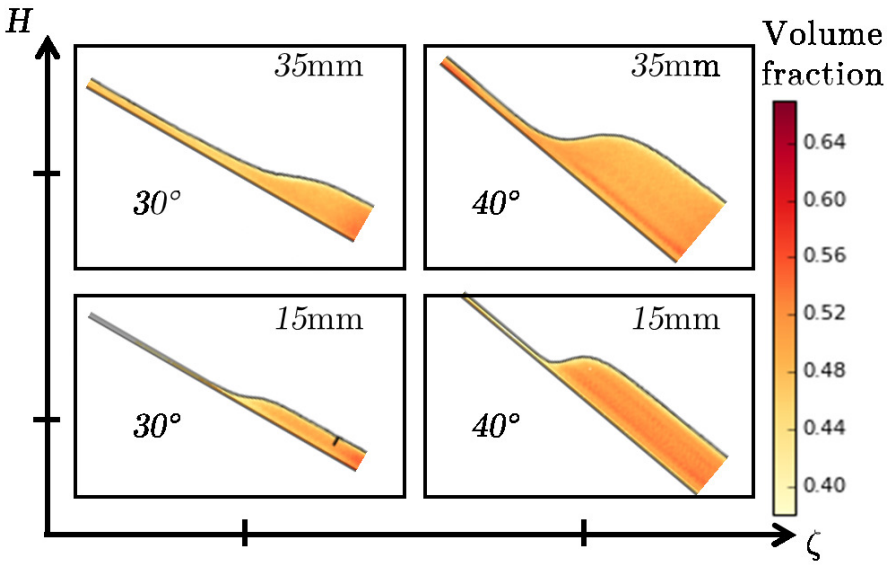

Figure 7.11: Phase diagram of the experiments with the rice, varying the slope angle and the discharge.

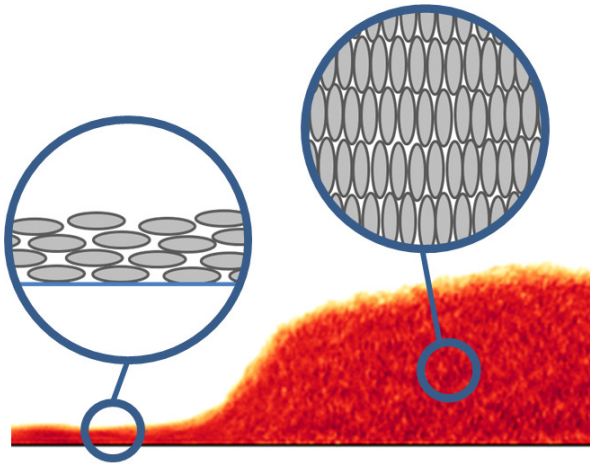

Figure 7.12: An example of jump with elongated particles ($\zeta = 40°$, $H = 35$mm): orientation of particles.

perpendicular to the bottom. They keep this alignment in the subcritical flow while the jump is propagating upstream and when it becomes stationary. The alignment of the grains is then parallel to the bottom before the jump, perpendicular to the bottom after the jump, and in an intermediate alignment state inside the jump, as shown in Fig. 7.12. This orientation change has a strong influence on the general shape of the jump.

7.3.3 A new type of granular jump

Upstream of the jump, the behaviour of the grains aligned with the bottom is similar to the behaviour of spherical grains. The volume fraction is lower than the maximum packing fraction, and the grains are mostly interacting through friction. Because of the elongation of the rice grains, and their rough nature, the friction between the grains is higher than the friction between spherical glass beads. The fact that the friction is stronger for ellipsoids than for spheres, when they are aligned in a shear flow, was already observed and explained by [11], and [47]. In our experiments, this higher friction in the incoming flow had a direct impact on our tests: although we could create some jumps with spherical particles at a slope of 25°, we did not succeed to create a jump under 30° with rice grains.

However, after the jump, when the particles are oriented perpendicularly to the bottom, the behaviour is totally different. The flow is not dominated by the grain/grain friction anymore, but by the trapping of the grains with their neighbours, that we can call geometrical friction. This geometrical friction is very high. Indeed, the force needed for one grain in the upstream part of the jump to pass over its neighbours is much higher than a contact friction between two grains, because of the geometrical blockage. The effect of the very high friction in the downstream part of the jump is seen in the limit angle ζ_0 (see Sec. 7.3.1). While this angle is a signature of the friction, depending on the outgoing flow conditions for the spherical grains, it is always equal to the bottom slope angle for the ellipsoids (see Figs. 7.11). On the contrary, numerical simulations in [45] showed that when the friction between grains is lowered close to zero, this angle is tending towards zero. This proves that the friction is responsible for this behaviour. Figure 7.13 illustrates this relation: when the friction between the particles μ tends towards zero, the limit angle ζ_0 also approaches zero. For spherical glass beads where the flow is only limited by a grain-grain friction μ, the limit angle ζ_0 was evolving with the bottom slope angle, and was always higher than zero and lower than the bottom slope angle. When a trapping of the grains is added to the grain-grain friction due to their shape, the effective friction, ζ_0 gets very high and reaches the slope of the bottom ζ. A jump with $\zeta_0 = \zeta$ would be impossible to create with spherical particles because the friction upstream would prevents flow in the flume altogether. Only a change in the orientation of the particles makes such jumps possible, and therefore, this type of jumps can only occur in a flow of orientable grains.

Another difference between glass beads and rice grains is the stability of the steady state, illustrated in Fig. 7.14. It shows a picture of a jump extracted from an experiment with rice grains (Fig. 7.14a) and another one from an experiment with glass beads (Fig. 7.14b). In both of them, the density, that is responsible for the determination of the free-surface, is averaged across the width of the channel (along the X-ray path), but not in time. In the experiment with glass beads, the black line representing the free-surface is very smooth, and looks like the pictures of standing jumps averaged in time (like in Fig. 7.4). On the opposite, the free-surface in the picture at a single timestep for rice grains (Fig. 7.14a) is very rough: an averaging in time is necessary to obtain a smooth

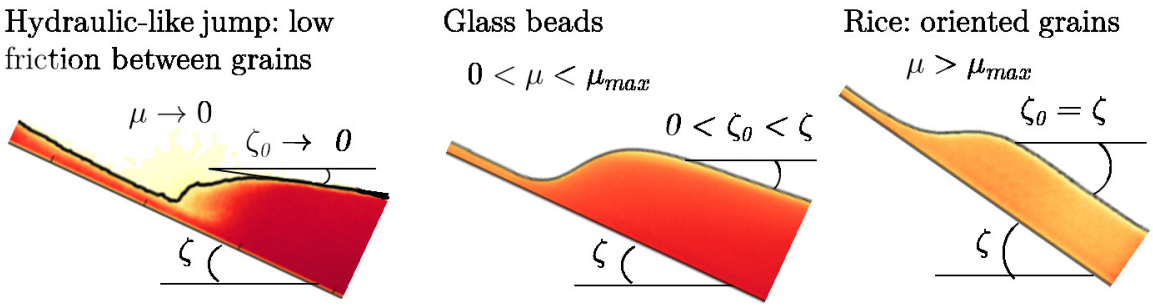

Figure 7.13: Illustration of the evolution of the limit angle ζ_0 with the friction coefficient between grains μ with the field of density of three jumps: a theoretical jump with very low friction between the grains obtained with DEM simulations in two dimensions (left), and two jumps obtained using X-ray radiography in the laboratory, with glass beads (middle) and rice grains (right).

free-surface (like in Fig. 7.11). This means that the width-averaging is not sufficient to smooth the irregularities in the case of rice grains: the roughness of the free-surface in Fig. 7.14a is caused by surface waves. The evolution of the surface waves over time is shown in Fig. 7.14c. The instantaneous height of the flow $h(t)$ was divided by the time-averaged height h and plotted in two different positions x of the channel, before (in red for rice grains, in blue for glass beads) and after (in orange for rice grains, in green for glass beads) the jumps plotted in Figs. 7.14a and 7.14b, and during 50 timesteps $\simeq$ 1.7sec. One can notice that the magnitude of the surface waves observed in the jump with rice grains is in the order of 5% of the averaged thickness, both in the incoming and outgoing flows. The waves are propagating at a wavelength that seems constant. Those waves do not exist at the surface of the jump in a flow of glass beads, where the steady state is almost perfect (less than 0.2% change in the free-surface, and no wavelength). The surface waves in the jump with rice grains can be explained by the grain alignment. When a rice grain reaches a gate (the gate at the exit of the reservoir for the incoming flow, and the retaining gate at the end of the channel for the outgoing flow), their shape makes them create a brief blockage, which will correspond to a wave trough. Then, the orientation of the grains allows them to keep a trace of this instability as they are flowing. This behaviour of blockage / release appeared also during the experiments. In the experiments with glass beads, the retaining gate was fixed as soon as the steady state was reached, until the end of the experiment. However, in the case of rice grains, the user needs to adjust the retaining gate continuously, in order to keep the steady state, because any blockage or release could propagate too much and then put an end to the steady state. This suggests that the jumps with elongated particles are naturally unsteady and the steady state may not be formally possible.

7.4 Discussion and conclusion

This chapter presented a new measurement technique based on dynamic X-ray radiography to measure density inside granular flows. This technique was tested on a wide range of granular flows varying the slope ζ and the discharge q through the opening of the tank exit H/d. Most of the results were obtained on an incoming flow of glass beads, which correspond to the classical configuration of a dense free-surface granular flow of spherical particles down a slope. The new measurement technique gave similar results to the stud-

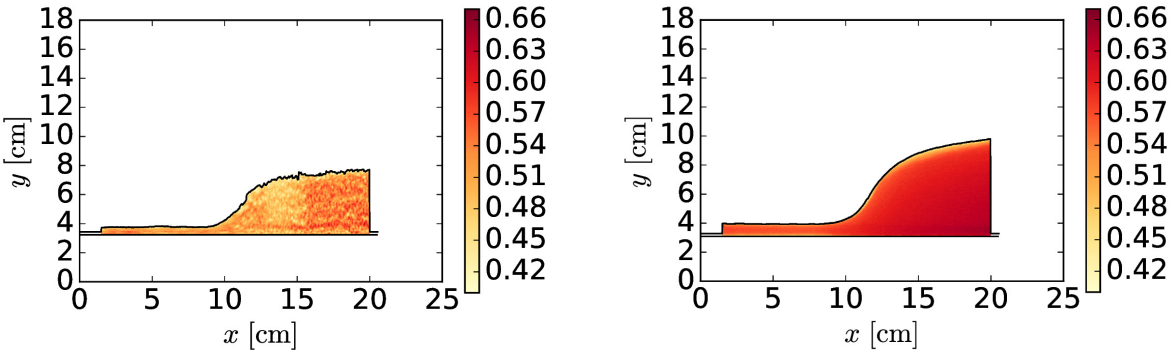

(a) (b)

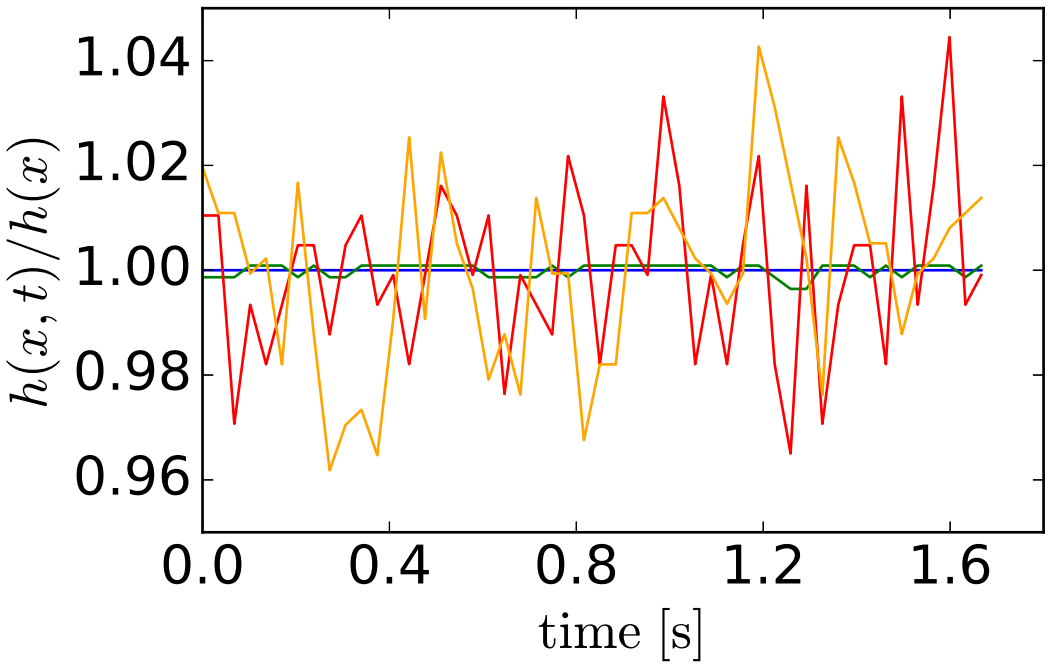

(c)

Figure 7.14: Instabilities of the flow: non-averaged image (showing the density field) of a jump made of rice grains (panel a), and a jump made of glass beads (panel b). The ratios of the instantaneous flow height over the averaged flow height have been plotted in panel c for the two previous jumps, on the incoming (red curve for rice grains, blue curve for glass beads), and outgoing (orange curve for rice grains, green curve for glass beads) flows, over 50 timesteps ($\simeq$ 1.7sec.). Flow height before (red, blue) and after (orange, green) a jump, for rice (red, orange) and glass beads, at 50 timesteps, divided by the average flow height. We can see that the free-surface is much more instable with the rice (up to 5% difference) than with glass beads (less than 0.2% difference).

ies which were not able to access the inside of the flows, and the volume fraction fields of the flows were measured. This careful measurement brought out the existence of a critical discharge q_c under which the volume fraction was so low that the volume fraction was influenced by the slope, creating jumps with a lower height ratio and a longer length than expected. This was not evidenced in the previous study of DEM simulations of 2D jumps [45] because such a low volume fraction became impossible to measure in two dimensions.

The study then focused on standing granular jumps. They combined a fast and thin incoming flow at supercritical state, a stable slow and thick outgoing flow at subcritical state, and a complex transition between them, where we could observe a fast increase of the flow height and decrease of the flow velocity, together with the effects of the compressibility, the friction and collisions between the grains and sometimes a recirculation pattern. This study was consistent with the previous studies on granular jumps, and brings new data, particularly on the volume fraction inside the jumps and their length. Here again, we observed the different behaviour of the jumps with a particularly low discharge $q < q_c$: although the relative length L/h was a constant for most jumps, it was significantly higher for jumps with the lowest discharge. Another result of the careful measurements inside the jumps was that the limit angle ζ_0 was not a constant but evolved with the flow conditions: it was maximum for the thickest and slowest outgoing flows, and decreases for faster and thinner outgoing flows.

Finally, the study explored the jumps of another grain shape. The rice grains are orientable, and the X-ray radiography showed that the incoming and outgoing flows behaved totally differently depending of their orientation. With this it was possible to observe a different type of granular jump, which had not been observed before. It opens the way to widen the possibilities for future research focused on grain shape effects. It would also be a good way to study the effects of the grain size distribution, for different degrees of polydispersity.

The novel X-ray measurement technique is demonstrated to be a promising experimental tool for future research. Some improvements should be considered: a detector with a faster acquisition rate would allow to measure directly the flow velocity, instead of propagating any error on other values by calculating it. It would also improve the quality of the images, and possibly help to quantify the orientation of the particles in the case of non-spherical grains.

Chapter 8

Conclusions and perspectives

8.1 Snow avalanches and design of protection dams

Snow avalanches represent a natural hazard that have been studied for decades. The problem of the interaction of avalanches with protection dams has received particular attention in recent years with current knowledge and capabilities being summarized in the handbook edited in 2009 by the European commission [3]. However, some aspects of snow avalanches still remain challenging and not fully understood.

When a snow avalanche impacts a dam, two distinct scenarios may follow: if the dam is not high enough, the flow remains supercritical and goes over the dam, but if the dam is high enough, the flow becomes subcritical and exhibits a jump. The equations currently used to design avalanche protection dams are strictly valid for frictionless incompressible flows on flat planes, or for shocks with no length and no volume. However, it has been proven that flowing snow cannot be idealized as a simple fluid, such as water. Snow aggregates in dense snow avalanches can, instead, be well represented as a system of dry grains, which forms what is known as granular flow. This thesis analyzes the macroscopic and microscopic features of standing jumps in granular flows down inclines.

The Bélanger's equation currently used in the design of avalanche protection dams to obtain the jump height ratio provides a good first-order approximation. However, granular materials are complex, and their finite volume should be taken into account. The weight of the jump tends to increase its height ratio while dissipation caused by friction and collisions between the grains have the opposite effect. Moreover, the first-order Bélanger's approximation is also not able to capture the effects of compressibility, which can lead to an overestimation or underestimation of the height of the protection dam.

Studying the geometry of the jumps by taking into account their finite volume, we showed that the jump length L has a strong influence, and thus should not be neglected. We demonstrated that the jump length relative to the thickness of the incoming flow L/h is a crucial input parameter and can be considered to be constant for all jumps, which is not the case for jumps in a non-frictional media like water.

The jumps studied in this thesis were always at steady state for simplification purposes. One of the most important perspective for future research would be to extend this work for unsteady conditions, which is relevant for natural conditions of snow-avalanches impacting protection dams. We believe that considering a frame of reference moving with the velocity of the jump should allow to transform the current results to those moving jumps. Our jumps involved the flow of stiff grains on smooth beds, with a very small amount of grain-size polydispersity. In order to get closer to natural avalanche conditions, future work should study the effects of different input conditions. One could use real snow flow in small-scale models to check if the jump properties are changed. Even if stiff grains are indeed appropriate for representing snow aggregates, it is possible to improve the current model by adding polydispersity or cohesion to the grains. Roughness can also be added to the bottom of the experiments to investigate its effects on the jump conditions.

Beyond the initial motivation of the improvement of the knowledge in the interaction between snow avalanches and protection dams, it is believed that this thesis work has substantially increased our understanding of granular jumps down a slope, and provided important answers to some fundamental issues. In the following, we remind some of those important outcomes and perspectives.

8.2 Innovative tools

This thesis work relied mostly on two tools with which we were able to create and do some detailed measurements on standing granular jumps down smooth inclines: numerical simulations and innovative X-ray experiments with laboratory chute device.

The numerical model was based on Discrete Element Method (DEM), using YADE software to create a numerical set-up that produces standing jumps. We showed that DEM is a powerful tool for creating and studying granular jumps. The numerical jumps reproduced all the behaviours expected from previous experimental experiments for various channel's slope angle and the incoming flow discharges, thus creating both steep and diffuse jumps, more or less compressible. The DEM has also enabled us to access various important variables within the jump, including local volume fraction, velocity, and energy dissipation. Thanks to coarse-graining, theses variables were presented either as 2D fields or with their depth-averaged value along the incline. The present numerical study was done in two dimensional idealization, in order to reduce the computational time. Note that in our preliminary work we found that it was possible to create three dimensional jumps with the same numerical tool. Future work could focus on those more realistic jumps in order to get closer to the laboratory conditions and to check if anything else different could emerge in three dimensions.

The small-scale laboratory experiments were done using an existing chute which was adapted to allow internal measurements of material properties using dynamic X-ray radiography, combined with an innovative image analysis method. This technique appeared to be very promising, and allowed us to obtain the width-averaged density field inside the experiment. This technique also seemed to be a good candidate to study the orientation of elongated particles. There are however some possible improvements to be carried out. A better stability of the experimental device should help to avoid the problems of detecting the bottom of the chute. A faster acquisition rate for the detector would improve the measurements, especially when it comes to observing the orientation of the grains. Moreover, it would allow to obtain the field of the width-averaged velocity everywhere within the jump, instead of calculating it from mass conservation, as we have achieved in the present thesis, which may have amplified any problem in the measurements due to technical issues. In the present configuration, it was only possible to obtain width-averaged values. Applying the method developed by Baker et al. on X-ray rheography [1], future work could enable to recover three dimensional fields of variables by adding two orthogonal X-ray sources and detectors to the granular chute.

8.3 Different types of granular jumps

Thanks to our numerical and experimental tools, it was possible to vary several parameters to study their influence on the shape of granular jumps. Both in the numerical and experimental set-ups, it was possible to vary the slope of the incline ζ, and the discharge of the incoming flow, through the height at the exit of the reservoir H. The numerical

model additionally allowed us to vary the interparticle friction between the grains μ, the grain diameter d, and the coefficient of restitution e. We also changed the shape of the grains in the small-scale experiments. We identified five types of granular jumps:

Laminar granular jumps are characterized by a smooth transition between the incoming and the outgoing flows. The thickness and the depth-averaged volume fraction increase smoothly in a monotonic way, the streamlines are well-distributed and the local velocity is always in the direction of the flow. This type of jumps is diffuse, and not very steep. It happens for low to medium slope angles of the incline. After the jump, the limit angle between the free-surface and the horizontal line reaches a constant angle ζ_0.

Steep colliding granular jumps are very steep jumps that are not stable enough to insure a smooth transition between the incoming supercritical flow and the outgoing subcritical flow. A recirculation zone, highly visible in the streamlines, appears close to the free-surface. The signature of the recirculation can be seen by a drop perturbing the monotonic increase of volume fraction. Those jumps appear when the slope angle of the incline is high. The limit angle of the free-surface after the jump ζ_0 is higher than the ones for laminar granular jumps.

Hydraulic-like jumps were observed only in numerical simulations due to the possibly unphysical conditions they can explore. They are created when the interparticle friction between grains becomes very low, lower than a critical interparticle friction. This granular jump behaves totally differently from jumps with the more physically meaningful friction, and has a behaviour approaching that of hydraulic jumps. A water-like roller is created, which presents a turbulent zone penetrating deeply into the jump. It can be identified from the curve describing the volume fraction by a big drop before the increase of the jump. The limit angle of the outgoing flow ζ_0 tends toward zero, which means that the free-surface of the outgoing flow tends to be horizontal.

Highly compressible jumps with a very low discharge were observed only in experimental conditions, because they are created with a very low discharge, which is physically meaningful only in three dimensions. They look like laminar granular jumps or steep colliding granular jumps depending on the slope angle of the incline. They differ from the other jumps in the volume fraction of the incoming flow, which is so low that it induces a very high compressibility of this jump type, and also changes the relative length L/h, which is slightly higher than for the other jumps. The existence of such jumps prove that density variations within jumps cannot be neglected.

Jumps with oriented particles are created with elongated particles, that can have a preferential orientation. The behaviour of those jumps is totally different from the ones formed with spherical particles. The particles in the incoming flow are aligned with the main flow direction, whereas they are oriented perpendicularly to the direction of the flow after the jump. The orientation of the particles after the flow gives them a very high geometrical friction, whose effect can be seen in the limit angle after the jump ζ_0, which is always equal to the slope angle of the incline. They are also highly unstable, some waves are forming and propagating along the surface, and the steady state is more difficult (or impossible) to obtain.

Studying the dissipation of energy along the incline, we showed that the differences between the jump types could be explained by their different ways to dissipate energy.

Most of the jumps studied involved spherical rigid grains. Changing the shape of the particles (allowing them to get orientated) allowed us to discover another type of jump. In that respect, it would be very interesting if future research could study the jumps made of different material with different shapes and different grain-size distributions.

8.4 Towards a general theoretical framework

We used mass and momentum conservation equations in order to understand the physics behind granular jumps. The goal was to find a relation that is able to predict the jump height ratio of any type of jump, including the presence or absence of frictional/collisional processes, without ignoring their possible compressibility, all while changing a wide range of input conditions, such as the slope of the incline or the discharge of the incoming flow.

Many experimental data sets from the literature were used to check this relation. As expected, the Bélanger's equation works well for incompressible non-frictional flows on a flat bottom. If the bottom is inclined and/or friction is added, a new parameter, the jump length L starts to play a role in determining the jump height ratio: a closure relation is needed for L to become fully predictive.

Using the measured jump length, our equation predicted very well the jump height ratio of jumps formed in water flows down an incline. In the case of water jumps with roughness on the bottom, we found a relation that worked for the resistive force τ_b induced by the roughness, but the question remains open to well understand its physical meaning.

The jumps in granular flows can only develop down inclines, while their compressibility, as well as frictional and collisional processes that come into play between the grains. The slope angle of the incline tends to increase the jump height ratio compared to a jump on a flat bottom, while the friction between the grains tends to decrease the jump height ratio compared to a non-frictional jump (like for hydraulic jumps). The compressibility also plays a role on the jump shape. When the effects of the slope angle and the friction are perfectly balanced in dense flows (poorly compressible), the Bélanger equation for frictionless materials flowing on a horizontal smooth bottom appears to work. The effect of the slope was well captured by the gravity forces on the volume of the jump, like for hydraulic jumps, and the frictional effects could be described by a simple law for the effective friction coefficient within the jump μ_e. Our equation takes into account the effects of the slope angle, the frictional forces, and the compressibility, which makes it more accurate than the Bélanger's equation.

Thanks to the numerical model, we were able to create jumps with almost no friction between the grains. The behaviour of those jumps is approaching the behaviour of hydraulic jumps. The resistive force expressed with an effective friction μ_e is not relevant anymore for those jumps. Finding a resistive force for those granular jumps may help to find a physically meaningful relation for the resistive force of water jumps on a rough base.

We saw that our general relation for jumps used the jump length L as an input parameter, leading to the need of another equation in order to have a closure relation and then become fully predictive. Our work on the energy conservation equation is not yet conclusive, but it enabled to quantify the energy loss along the granular jumps in two-dimensional numerical simulations. We found that the conservative part of the energy is mostly formed of the kinetic energy and the gravitational potential energy. The elastic energy can be neglected, although it may be useful to note that it can be linked to

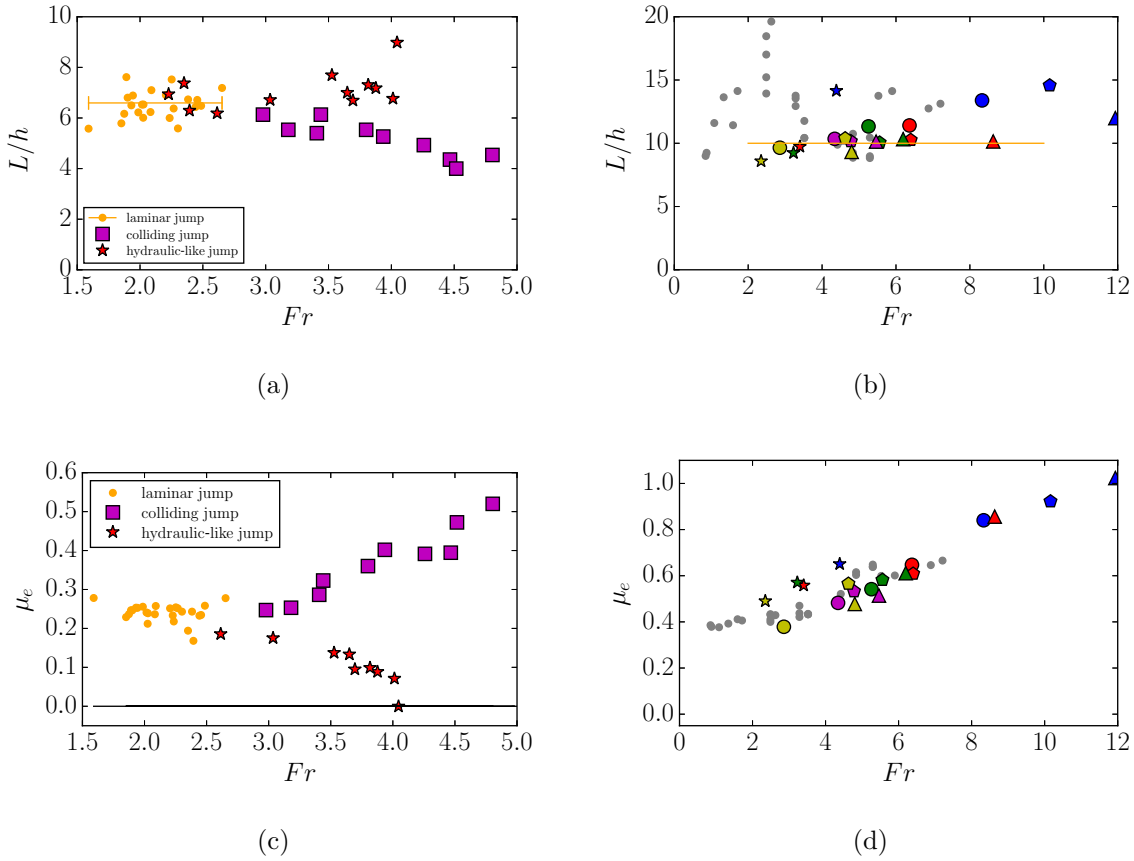

Figure 8.1: Jump length relative to the incoming flow height L/h as a function of the Froude number for both numerical (panel a) and experimental (panel b) results. Effective friction inside the jumps μ_e for both numerical (panel c) and experimental (panel d) results. Numerical colours and markers (panels a and c) are the same as used in Chap. 5: orange dots for laminar granular jumps, purple squares for steep colliding granular jumps, and red stars for hydraulic-like granular jumps. Experimental markers and colours (panel b and d) are the same as in Chap. 7: marker shapes: stars $\zeta = 20°$, circles $\zeta = 25°$, pentagons $\zeta = 30°$, triangles $\zeta = 35°$; marker colours: blue $H = 15$mm, red $H = 20$mm, green $H = 25$mm, purple $H = 30$mm, and yellow $H = 35$mm, and in addition, grey dots show the experimental data from the previous experiments of [19].

the volume fraction. We proposed an equation for the loss inside the granular jumps that can be computed with depth-averaged values. This relation works to a first order approximation, but still needs improvements, as its error, which is evolving with the incoming Froude number, can reach up to 30% under some conditions. This relation could help us to have a relation for L and then a fully predictive theoretical framework for the jump height.

In want of any theoretical prediction for the relative jump length L/h, one main objective of the Ph.D work was to measure it. Figure 8.1a and b summarize all the results for L/h. Figure 8.1a shows the relative jump length of numerical 2D simulations, and Fig. 8.1b shows the experimental results, both from the previous experiments of [19] (grey dots) and from the present experiments with the X-ray measurement technique (coloured markers). The relative jump length L/h is a constant for most jumps. Something different happens for the hydraulic-like jumps (red stars in Fig. 8.1a), where the relative length

increases with the Froude number, which is the same behaviour as hydraulic jumps. In the case of steep colliding granular jumps, it is clear that the decrease of L/h with the Froude number only happens in 2D conditions comforting the need for future research to explore 3D numerical jumps. The other difference is the magnitude, which is smaller in 2D compared to 3D conditions. Figure 8.1b shows that the new measure is a lot less scattered, thus demonstrating that the X-ray technique is much more robust to identify the jump length compared to the grey points where the measurement were done on one sidewall. This is explained by the fact that the X-ray measurements of L/H are based not only the free-surface changes but also the changes in volume fraction.

The last parameter for the equation presented in Chap. 2 to become fully predictive is the effective friction inside the jump μ_e. The results concerning this coefficient back-calculated from Eq. (2.7) of Chap. 2 are summarised in Fig.8.1c for numerical 2D simulations and Fig. 8.1d for 3D laboratory experiments. Again, it is possible to conclude that the hydraulic-like jumps cannot be described by the same laws as granular jumps with a coloumbian friction. For all the jumps except hydraulic-like jumps with a roller, the relation between μ_e and the Froude number follows the same trend, even if the magnitude is smaller under 2D conditions than in 3D.

Bibliography

[1] James Baker, François Guillard, Benjy Marks, and Itai Einav. X-ray rheography uncovers planar granular flows despite non-planar walls. *Nature communications*, 9(1):5119, 2018.

[2] Boris A Bakhmeteff and Arthur E Matzke. The hydraulic jump in terms of dynamic similarity. *Transactions of the American Society of Civil Engineers*, 101(1):630–647, 1936.

[3] M Barbolini, U Domaas, T Faug, P Gauer, KM Hakonardottir, CB Harbitz, D Issler, T Johannesson, K Lied, M Naaïm, F Naaim-Bouvet, and L. Rammer. *The design of avalanche protection dams Recent practical and theoretical developments*. European Commission, Directorate-General for Research, Publication EUR 23339, 2009.

[4] Jean Baptiste Belanger. *Essai sur la solution numerique de quelques problemes relatifs au mouvement permanent des eaux courantes; par m. J.-B. Belanger..* chez Carilian-Goeury, libraire, des corps royaux des ponts et chaussees et ..., 1828.

[5] D. Berzi, C. G. di Prisco, and D. Vescovi. Constitutive relations for steady, dense granular flows. *Physical Review E*, 84:031301, Sep 2011.

[6] W Ar Beverloo, Hendrik Antonie Leniger, and J Van de Velde. The flow of granular solids through orifices. *Chemical engineering science*, 15(3-4):260–269, 1961.

[7] JF Boudet, Y Amarouchene, B Bonnier, and H Kellay. The granular jump. *Journal of Fluid Mechanics*, 572:413–432, 2007.

[8] C.E. Brennen, K. Sieck, and J. Paslaski. Hydraulic jumps in granular material flow. *Powder Technology*, 35(1):31 – 37, 1983.

[9] Nicolas Brodu, Patrick Richard, and Renaud Delannay. Shallow granular flows down flat frictional channels: Steady flows and longitudinal vortices. *Physical Review E*, 87(2):022202, 2013.

[10] John WM Bush and Jeffrey M Aristoff. The influence of surface tension on the circular hydraulic jump. *Journal of Fluid Mechanics*, 489:229–238, 2003.

[11] Charles S Campbell. Elastic granular flows of ellipsoidal particles. *Physics of Fluids*, 23(1):013306, 2011.

[12] Girolamo Cardano and C Spon. Ars magna (1545). *Opera Omnia*, 4:221–302, 1968.

[13] Francesco Giuseppe Carollo, Vito Ferro, and Vincenzo Pampalone. Hydraulic jumps on rough beds. *Journal of Hydraulic Engineering*, 133(9):989–999, 2007.

[14] Hubert Chanson. Current knowledge in hydraulic jumps and related phenomena. a survey of experimental results. *European Journal of Mechanics-B/Fluids*, 28 (2):191–210, 2009.

[15] Hubert Chanson. Development of the bélanger equation and backwater equation by jean-baptiste bélanger (1828). *Journal of Hydraulic Engineering*, 135 (3):159–163, 2009.

[16] Ven Te Chow. *Open-Channels Hydraulics*. McGraw-Hill, New York, 1959.

[17] Thierry Faug. Jumps and bores in bulky frictional granular flows. In *POWDERS AND GRAINS 2013: Proceedings of the 7th International Conference on Micromechanics of Granular Media*, volume 1542, pages 642–645. AIP Publishing, 2013.

[18] Thierry Faug. Depth-averaged analytic solutions for free-surface granular flows impacting rigid walls down inclines. *Physical Review E*, 92(6):062310, 2015.

[19] Thierry Faug, Philippa Childs, Edward Wyburn, and Itai Einav. Standing jumps in shallow granular flows down smooth inclines. *Physics of Fluids*, 27(7):073304, 2015.

[20] Yoel Forterre and Olivier Pouliquen. Flows of dense granular media. *Annual Review of Fluid Mechanics*, 40(1), 2007.

[21] GDRMidi. On dense granular flows. *The European Physical Journal E*, 14(4):341–365, Aug 2004.

[22] Gustavo Gioia and Pinaki Chakraborty. Turbulent friction in rough pipes and the energy spectrum of the phenomenological theory. *Physical Review Letters*, 96:044502, 2006.

[23] C Goldenberg and I Goldhirsch. *Continuum mechanics for small systems and fine resolutions*. American Scientific Publishers, Stevenson Ranch, CA, 2006.

[24] Isaac Goldhirsch. Rapid granular flows. *Annual review of fluid mechanics*, 35(1):267–293, 2003.

[25] Isaac Goldhirsch. Stress, stress asymmetry and couple stress: from discrete particles to continuous fields. *Granular Matter*, 12(3):239–252, 2010.

[26] J. M. N. T. Gray, Y.-C. Tai, and S. Noelle. Shock waves, dead zones and particle-free regions in rapid granular free-surface flows. *Journal of Fluid Mechanics*, 491:161–181, 9 2003.

[27] JMNT Gray and X Cui. Weak, strong and detached oblique shocks in gravity-driven granular free-surface flows. *Journal of Fluid Mechanics*, 579:113–136, 2007.

[28] François Guillard, Benjy Marks, and Itai Einav. Dynamic x-ray radiography reveals particle size and shape orientation fields during granular flow. *Scientific Reports*, 7(1):8155, 2017.

[29] Willi H Hager. *Energy dissipators and hydraulic jump*. Kluwer Academic Publishers, 1992.

[30] Willi H Hager and Roger Bremen. Classical hydraulic jump: sequent depths. *Journal of Hydraulic Research*, 27(5):565–585, 1989.

[31] Kristín Martha Hákonardóttir. *The interaction between snow avalanches and dams*. PhD thesis, University of Bristol, 2004.

[32] Kristin Martha Hákonardóttir and Andrew J Hogg. Oblique shocks in rapid granular flows. *Physics of Fluids (1994-present)*, 17(7):077101, 2005.

[33] Alex J. Holyoake and Jim N. McElwaine. High-speed granular chute flows. *Journal of Fluid Mechanics*, 710:35–71, 11 2012.

[34] William C Hughes and J Ernest Flack. Hydraulic jump properties over a rough bed. *Journal of Hydraulic Engineering*, 110(12):1755–1771, 1984.

[35] D Husain, AA Alhamid, and Abdel-Azim M Negm. Length and depth of hydraulic jump in sloping channels. *Journal of Hydraulic Research*, 32(6):899–910, 1994.

[36] S.R. Nagel Jaeger, M. and R. P. Behringer. Granular solids, liquids, and gases. *Rev. Mod. Phys.*, 68:1259, 1996.

[37] JAMES T Jenkins and MW Richman. Kinetic theory for plane flows of a dense gas of identical, rough, inelastic, circular disks. *The Physics of fluids*, 28(12):3485–3494, 1985.

[38] C. G. Johnson and J. M. N. T. Gray. Granular jets and hydraulic jumps on an inclined plane. *Journal of Fluid Mechanics*, 675:87–116, 2011.

[39] Pierre Jop. Rheological properties of dense granular flows. *Comptes Rendus Physique*, 16(1):62 – 72, 2015.

[40] Pierre Jop, Yoël Forterre, and Olivier Pouliquen. A constitutive law for dense granular flows. *Nature*, 441(7094):727–730, 2006.

[41] Carl E Kindsvater. The hydraulic jump in sloping channels. *Trans. ASCE*, 109:1107–1154, 1944.

[42] Michel Y. Louge and Stephen C. Keast. On dense granular flows down flat frictional inclines. *Physics of Fluids*, 13(5):1213–1233, 2001.

[43] Leon B Lucy. A numerical approach to the testing of the fission hypothesis. *The astronomical journal*, 82:1013–1024, 1977.

[44] S. Méjean, T. Faug, and I. Einav. A general relation for standing normal jumps in both hydraulic and dry granular flows. *Journal of Fluid Mechanics*, 816:331–351, 2017.

[45] S. Méjean, F. Guillard, T. Faug, and I. Einav. Length of standing jumps along granular flows down inclines. *Physical Review Fluid*, 2019.

[46] Ségolène Méjean, Thierry Faug, and Itai Einav. Discrete element method simulations of standing jumps in granular flows down inclines. In *EPJ Web of Conferences*, volume 140, page 03026. EDP Sciences, 2017.

[47] Dániel B Nagy, Philippe Claudin, Tamás Börzsönyi, and Ellák Somfai. Rheology of dense granular flows for elongated particles. *Physical Review E*, 96(6):062903, 2017.

[48] Iwao Ohtsu and Youichi Yasuda. Hydraulic jump in sloping channels. *Journal of Hydraulic Engineering*, 117(7):905–921, 1991.

[49] Iwao Ohtsu, Youichi Yasuda, and Motoyasu Ishikawa. Submerged hydraulic jumps below abrupt expansions. *Journal of hydraulic engineering*, 125(5):492–499, 1999.

[50] A. J. Peterka. *Hydraulic design of stilling basins and energy dissipators*. Engineering Monograph No. 25, 1984.

[51] O. Pouliquen and Y. Forterre. Friction law for dense granular flows: application to the motion of a mass down a rough inclined plane. *Journal of Fluid Mechanics*, 453:133–151, 2002.

[52] Olivier Pouliquen. Scaling laws in granular flows down rough inclined planes. *Physics of fluids*, 11(3):542–548, 1999.

[53] Farhang Radjai and Stéphane Roux. Turbulentlike fluctuations in quasistatic flow of granular media. *Physical review letters*, 89(6):064302, 2002.

[54] N Rajaratnam. Hydraulic jumps. *Advances in hydroscience*, 4:197–280, 1967.

[55] R. Riegel and J. Beebe. *The Hydraulic jump as a means of dissipating energy*. Dayton, Ohio : State of Ohio, Miami Conservancy District, 1917.

[56] Pierre Rognon, Thomas Miller, and Itai Einav. A circulation-based method for detecting vortices in granular materials. *Granular Matter*, 17(2):177–188, 2015.

[57] Pierre G Rognon, Jean-Noël Roux, Mohamed Naaim, and François Chevoir. Dense flows of cohesive granular materials. *Journal of Fluid Mechanics*, 596:21–47, 2008.

[58] Jean-Noël Roux and Gaël Combe. Quasistatic rheology and the origins of strain. *Comptes Rendus Physique*, 3(2):131–140, 2002.

[59] G Saingier, S Deboeuf, and P-Y Lagrée. On the front shape of an inertial granular flow down a rough incline. *Physics of Fluids (1994-present)*, 28(5):053302, 2016.

[60] S. B. Savage and K. Hutter. The motion of a finite mass of granular material down a rough incline. *Journal of Fluid Mechanics*, 199:177–215, 1989.

[61] Stuart B. Savage. Gravity flow of cohesionless granular materials in chutes and channels. *Journal of Fluid Mechanics*, 92:53–96, 5 1979.

[62] Abraham Savitzky and Marcel JE Golay. Smoothing and differentiation of data by simplified least squares procedures. *Analytical chemistry*, 36(8):1627–1639, 1964.

[63] H. Schulz, U.D. Nóbrega, A.L.A. Simões, H. Schulz, and Rodrigo de Melo Porto. *Hydrodynamics - Concepts and Experiments*, chapter Details of Hydraulic Jumps for Design Criteria of Hydraulic Structures, pages 73–116. 2015.

[64] L.E. Silbert, D. Ertas, G. S. Grest, T. C. Halsey, D. Levine, and S. J. Plimpton. Granular flow down an inclined plane: Bagnold scaling and rheology. *Physical Review E*, 64:051302, 2001.

[65] R. Silvester. Hydraulic jump in all shapes of horizontal channels. *J. Hydraul. Div. ASCE*, 90:23–55, 1964.

[66] V. Smilauer, A. Gladky, J. Kozicki, C. Modenese, and J. Stronsky. Yade, Using and Programming. In V. Smilauer, editor, *Yade Documentation*. The Yade Project, 1st edition, 2010. http://yade-dem.org/doc/.

[67] Alfredo Taboada, Nicolas Estrada, and Farhang Radjai. Additive decomposition of shear strength in cohesive granular media from grain-scale interactions. *Physical review letters*, 97(9):098302, 2006.

[68] S. Viroulet, J. L. Baker, A. N. Edwards, C. G. Johnson, C. Gjaltema, P. Clavel, and J. M. N. T. Gray. Multiple solutions for granular flow over a smooth two-dimensional bump. *Journal of Fluid Mechanics*, 815:77–116, 2017.

[69] AW Vreman, M Al-Tarazi, JAM Kuipers, M van Sint Annaland, and O Bokhove. Supercritical shallow granular flow through a contraction: experiment, theory and simulation. *Journal of fluid mechanics*, 578(1):233–269, 2007.

[70] Thomas Weinhart, Remco Hartkamp, Anthony R. Thornton, and Stefan Luding. Coarse-grained local and objective continuum description of three-dimensional granular flows down an inclined surface. *Physics of Fluids*, 25(7):070605, 2013.

[71] Thomas Weinhart, Anthony R Thornton, Stefan Luding, and Onno Bokhove. Closure relations for shallow granular flows from particle simulations. *Granular Matter*, 14(4):531–552, 2012.

[72] Gerald Beresford Whitham. *Linear and nonlinear waves*, volume 42. John Wiley & Sons, 2011.

[73] Chia-Shun Yih and C. R. Guha. Hydraulic jump in a fluid system of two layers. *Tellus*, 7(3):358–366, 1955.

[74] V. Šmilauer, E. Catalano, B. Chareyre, S. Dorofeenko, Duriez J., A. Gladky, J. Kozicki, C. Modenese, L. Scholtès, L. Sibille, J. Stránský, and K. Thoeni. Yade Reference Documentation. In *Yade Documentation*. The Yade Project, 2010.

Abstract. The design of avalanche protection dams relies on the understanding and modelling of physical processes related to the formation of jumps that form when a thin and fast flow meets an obstacle high enough to slow down and thicken the incoming flow. The jump height is nowadays calculated through equations that are strictly valid for non-frictional incompressible flows on a horizontal and smooth bottom. However, dense-snow avalanches are compressible granular flows taking place on a slope, and inside which energy is dissipated through enduring frictional contacts and collisions between grains. It is then essential to decipher the behaviour of jumps formed during granular flows down inclines. To this extent, the thesis relies on several approaches. Standing granular jumps are first studied in a purely theoretical way, with the help of depth-averaged mass and momentum conservation equations, in order to find a relation to predict the height of the jumps regardless of the input conditions. A great number of granular jumps are then simulated by varying several parameters (the slope angle of the incline, the discharge, the grain diameter, the grain-grain friction) thanks to the discrete element method. This method allows us to access to the internal structure of the jumps, and in particular to the spatial distributions of velocity, volume fraction and energy dissipation. Those simulations are done in two dimensions. Finally, an innovative measurement technique using dynamic X-ray radiography was adapted to an existing small-scale laboratory device to produce standing granular jumps. This technique allows in particular the measurement of the width-averaged spatial distribution of volume fraction before, inside and after the granular jumps. The comparison between the new theoretical framework proposed and both the experimental and numerical data, allows us to evidence a rich variety of granular jump patterns as a function of the input conditions. For each type of jump pattern, the shortcomings of the classical theoretical framework, which does not account for the forces at stake within the jump volume nor the compressibility, are well established.

Résumé. Le dimensionnement des digues paravalanches s'appuie sur la connaissance des processus physiques liés au ressaut, qui se forme lorsqu'un écoulement fin et rapide rencontre un obstacle suffisamment haut pour ralentir et épaissir l'écoulement incident. La hauteur du ressaut est aujourd'hui calculée à partir d'équations strictement valides pour des écoulements de matériaux non frictionnels et non compressibles tels que l'eau, sur fond plat et lisse. Or, les avalanches de neige dense sont des écoulements compressibles qui ne peuvent avoir lieu qu'en pente, et au sein desquels se produit de la dissipation d'énergie par friction et collisions entre les grains. Il est donc essentiel de mieux connaître le comportement des ressauts dans les écoulements granulaires en pente. Pour cela, la thèse s'appuie sur plusieurs approches. Les ressauts granulaires stationnaires sont d'abord étudiés de manière purement théorique, à l'aide des équations de conservation de la masse et de la quantité de mouvement moyennées dans l'épaisseur, afin de trouver une relation générale pour prédire la hauteur des ressauts quelques soient les conditions d'entrée. Nous simulons ensuite numériquement un grand nombre de ressauts granulaires en faisant varier plusieurs paramètres (la pente du plan incliné, le débit, le diamètre des grains, la friction entre les grains) à l'aide de la méthode aux éléments discrets. Cette méthode permet d'accéder à la structure interne des ressauts, et notamment à la mesure des champs de vitesse, de fraction volumique, ou encore de la dissipation d'énergie. Les simulations sont réalisées en deux dimensions. Enfin, un dispositif de mesure innovant, qui utilise la radiographie à rayons X dynamique, a été adapté à une expérience de laboratoire existante pour créer des ressauts granulaires stationnaires. Cette technique de mesure permet, en particulier, de mesurer la distribution spatiale moyennée dans la largeur de l'écoulement de la fraction volumique avant, à l'intérieur et après le ressaut granulaire. La comparaison du nouveau cadre théorique proposé avec les résultats expérimentaux et numériques nous permet de mettre en évidence une grande diversité des types de ressauts granulaires en fonction des conditions initiales. Pour chaque type de ressaut, les lacunes du cadre théorique classique, qui ne tient pas compte des forces mises en jeu dans le ressaut ni de la compressibilité, sont clairement établies.